Dissertation

Influencing rolling contact fatigue and wear by different rail grades and contact conditions

Dipl.Ing. Richard Stock

Leoben, 15.11.2011

This thesis was typset using LaTeX, Lyx and KOMA-Script

voestalpine Schienen GmbH
Kerpelystrasse 199
8700 Leoben
www.voestalpine.com

For Dipl. Ing. Richard Stock (1936 - 1993)

Declaration

I declare in lieu and oath, that I wrote this thesis and performed the associated research myself, using only literature cited in this volume

Leoben, November 2011

Acknowledgments

First of all I would like to say thank you to my supervisor Prof. Dr. Reinhard Pippan for his supervisory work, for the patience and for the productive discussions.

Secondly I am very grateful that voestalpine Schienen GmbH gave me the possibility to conduct this project as part of my work. Special thanks to my superiors Peter Pointner, Norbert Frank, Gregor Girsch and Hans Peter Brantner for fruitful, skeptical and energetic discussions about wear and RCF of rail steels and for their continuous support. Also special thanks to my colleagues at voestalpine for all their help with this work.

A very special "Thank You" also to Kelsan Technologies (now LB Foster Friction Management) in Vancouver / Canada for the help with the friction modifier related work. Don Eadie, Kevin Oldknow and Dave Elvidge provided big help on the technical side for the test rig tests and they always spend their time for being constructive and motivating partners for technical discussions about friction management, wear, RCF and everything under the sun. Many thanks also for the great 8 months in Vancouver.

Finally I would like to thank my wife Alexandra and my sons Felix, Benjamin and Jakob for their motivation, support, patience and understanding.

Thank you very much all of you!

Abstract

The continuing increase of axle loads, train frequencies and train speeds both in passenger service and freight operations are causing a consequent increase in stress on track and trains. Infrastructure owners have to face the challenge to manage and reduce the costs caused by the effects of these increasing stresses – Rolling Contact Fatigue (RCF) and wear. According to shakedown theory several approaches can be selected to mitigate the formation of damage on the rail surface. The rail grade influences the formation of damage by its microstructure and mechanical properties. Managing the friction between wheel and rail with a friction modifier will reduce the maximum possible traction that can be transmitted from wheel to rail. A friction modifier provides constant and positive friction characteristics (no maximum in the traction - creepage relationship) at an intermediate friction level without influencing traction or braking behavior of trains.

This thesis investigates the wear and RCF behavior of several pearlitic and bainitic rail steels on a full scale test rig at voestalpine Schienen GmbH under dry and friction modifier contact conditions and compares the results with selected track tests of voestalpine. The test rig is capable of producing realistic contact conditions that allow the formation of wear and RCF defects in very short time periods within 100,000 wheel passes. On the test rig the improved wear and RCF resistance of higher hardness steels is clearly seen. Bainitic steels show a slightly different behavior – the wear resistance is reduced compared to a pearlitic steel with the same hardness level though the RCF resistance is higher. The tests with the friction modifier highlight its capability to further reduce the formation of wear and RCF and thereby provide an addition to rail life extension. Although the trends are consistent on the rig and in track, the absolute values concerning wear and RCF differ due to some specific differences between track and test rig conditions. Finally ideas are postulated that explain on one hand the test rig specific wear behavior of the rail grades and on the other the formation of periodic, rail grade dependent crack spacing of the defect type head checks.

Contents

Part I.

Introduction to the system

1. The railway system

The history of railways and railway track goes far back to ancient times. The Greeks and the Romans [1, 2] used stone carved grooves to guide vehicles for religious or trading reasons. Around 1500 wooden board track is mentioned to be used for mining vehicles. The year 1789 can be seen as the hour of birth for the modern railway track as the first cast iron rail was produced in England. Since then the continuing increase of axle loads, train frequencies and train speeds both in passenger service and freight operations is causing a consequent increase in stress on track and trains. Infrastructure owners have to face the challenge to manage and reduce the costs caused by the effects of these increasing stresses – rolling contact fatigue (RCF) and wear. Since the early days of railway operations the steel quality of the rail steel was continuously improved and further developed to conquer the degrading effects of steel on steel contact. Soon after the breakthrough of the railway in Europe research attention was put to the railway system resulting in outstanding scientific findings that help to better understand this system (e.g. Hertz 1881 [3], Klingel 1883 [4], Carter 1926 [5], Archard 1953 [6], Johnson 1985 [7]etc..). Still nowadays the complex and multi-scale challenges of the railway system with the small rail wheel contact as the center point of this system (see figure 1.1) provide many areas with so far unsolved problems. The work in this thesis focuses specifically on this central point - the rail wheel contact - and the resulting problems of wear and rolling contact fatigue (RCF).

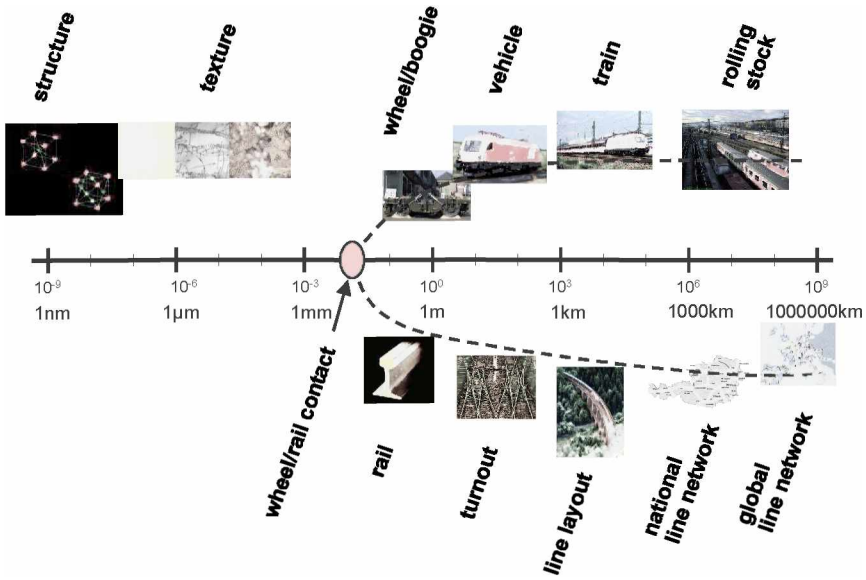

Figure 1.1.: The railway system - a multi-scale challenge. From the atomic structure of the material to the wheel-rail contact to the global line network.

2. Rail Wheel Contact

This chapter represents a compendium of [8]. Additional references are listed in the text.

2.1. General Contact Conditions

The general conditions of steel bodies brought into contact are shown in figure 2.1. A problem according to figure 2.1 is called a normal contact problem as two bodies are brought into contact normal (perpendicular) to their surface (in z-direction). Both bodies are considered to be elastic with known mechanical properties (E, ν) and they will meet at an initial contact point 0 (origin of coordinate system) when the normal distance (normal to a body) between these two bodies reaches a minimum. The surfaces of these bodies can be described by polynomial surfaces of the order of two as

$$z = Ax^2 + By^2. \tag{2.1}$$

If a normal load (P) is applied, the bodies will deform and a pressure distribution p(x,y) within the contact patch will provide an equilibrium condition. δ_z describes the normal distance of a point from the surface in the case of penetrating bodies without interaction. In case of tangential loading (Q_x, Q_y) a tangential deformation $\delta_x$and $\delta_y$of the bodies will take place. The equilibrium concerning tangential forces is maintained by shear stresses q_x(x,y) and q_y(x,y). In order to solve the contact problem it is necessary to know either the deformations ($\delta_x, \delta_y, \delta_z$) or the global loads (P, Q_x, Q_y) or a combination of both so that the pressure distribution p(x,y) and resultant shear forces (q_x(x,y), q_y(x,y)) can be determined. The following assumptions are necessary:

- Small strain settings of elastic, isotropic and homogeneous materials.
- The contact area is much smaller than the dimensions of the contacting bodies (infinite half spaces). Consequently this only applies for non-conformal contacts (point or line contacts).
- Flat contact surfaces within the contact patch. As a result the pressure distribution is acting in z direction.

2.2. Normal contact problem

Heinrich Hertz developed his normal contact theory at the age of 24 when he was working as a research assistant at the University of Berlin [3]. The Theory of Hertz proved that the normal contact between two elastic non-conformal bodies has the shape of an ellipse and he proposed a method of calculating the pressure distribution within the contact area and the semi axes of the contact ellipse. Besides this general contact condition Hertz developed equations for

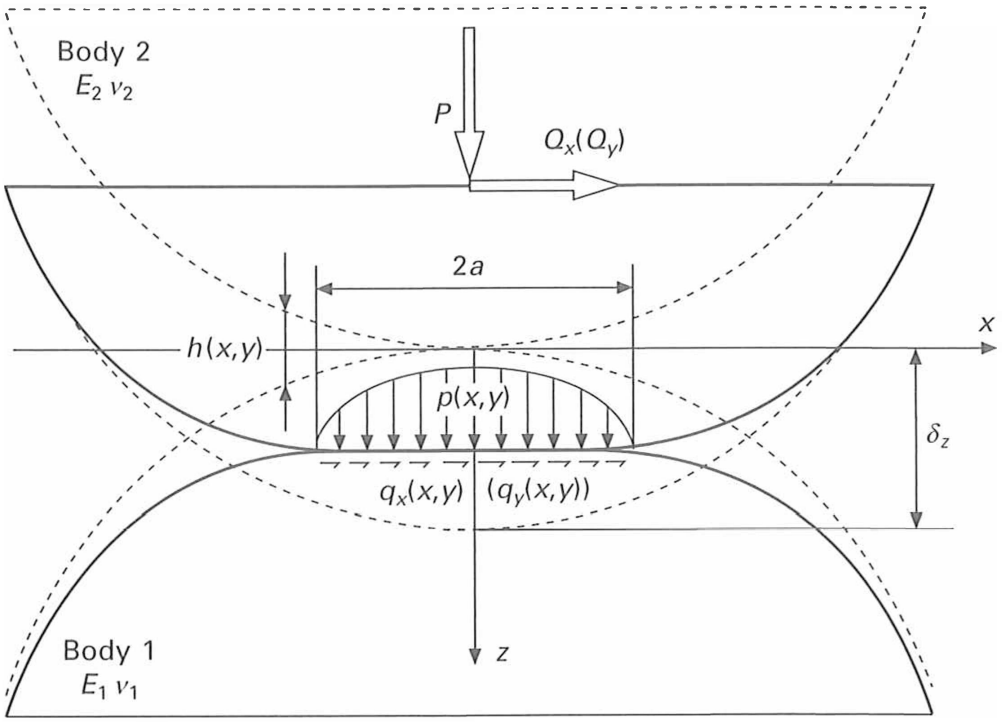

Figure 2.1.: General contact between two elastic bodies loaded with normal load P and tangential load Q, taken from [9].

the vertical deformation, contact size, maximum pressure and pressure distribution for two special cases (figure 2.1) that are of particular interest for the rail wheel contact:

- Line contact - contact between cylinders.
- Point contact - contact between two spheres.

For the general case (two bodies with convex curvatures in all directions, radii Rx and Ry) no explicit equations are available. A summary of the equations calculated by Hertz for the two special conditions can be seen in table 2.1.

2.3. Tangential contact problem

When applying a tangential force to the normally loaded contact sliding will eventually occur. Before the whole contact will start to slide (macro slip) only parts of the contact will develop local slip. The rest of the contact will still stay in the stick condition. This condition is referred to as micro slip. Slip will start in regions with low pressure distribution. This means for circular or point contact that slip will form in the outer region of the contact whereas the center still remains in stick condition (circular shape). For the line contact the slip area will have a rectangular shape surrounded by the slip region. For a body that is normally loaded by P and subjected to a tangential load Q_x equations for the calculation of the size and shape of the stick and slip regions have been derived according to Mindlin [10] (based on Carter [5]) for line contact (c: size of the stick region, μ : coefficient of friction and a: contact size according to Hertz - see also figure 2.5) as

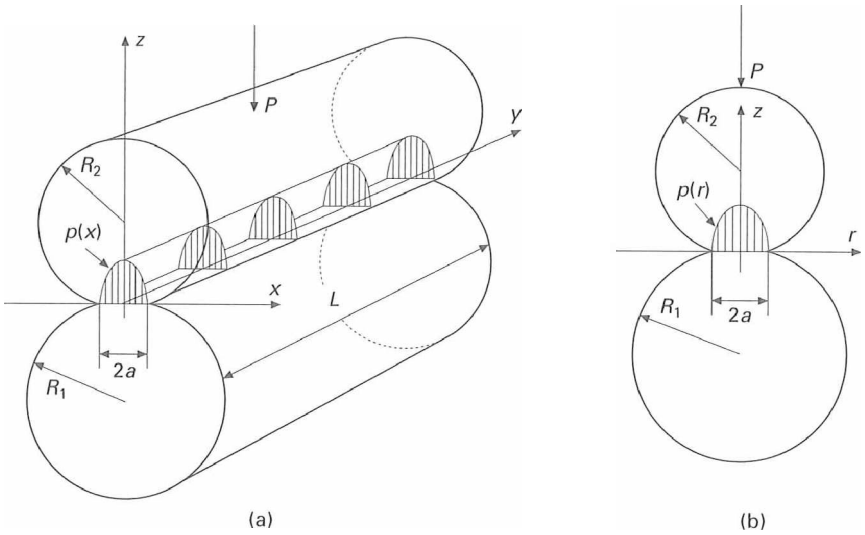

Figure 2.2.: Two special cases Hertz contacts: a) line contact, b) point contact, picture taken from [8].

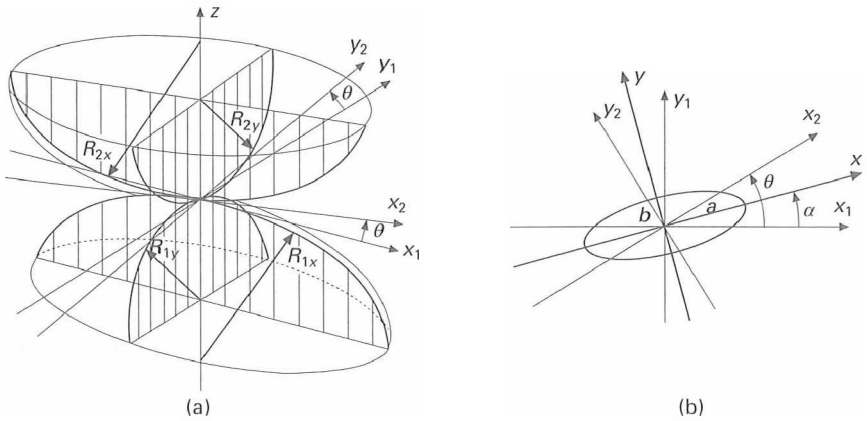

Figure 2.3.: General Hertzian contact between two bodies, (a) bodies contacting initially in one singular point (without load) and (b) resulting contact ellipsis if a certain load (P) is applied. Figure taken from [8].

	line contact	circular contact	elliptical contact
Equivalent Modulus of Elasticity	$\frac{1}{E^*} = \frac{1-\nu_1^2}{E_1} + \frac{1-\nu_2^2}{E_2}$		
Equivalent radius	$\frac{1}{R} = \frac{1}{R_1} + \frac{1}{R_2}$		series of equations
Contact Size	a=$\left(\frac{4PR}{\pi LE^*}\right)^{\frac{1}{2}}$	a=$\left(\frac{3PR}{4E^*}\right)^{\frac{1}{3}}$	c = $\sqrt{ab}$= $\left(\frac{3PR}{4E^*}\right)^{\frac{1}{3}} F_1(\xi)$
Maximum pressure	p0=$\left(\frac{PE^*}{\pi LR}\right)^{\frac{1}{2}}$	p0=$\left(\frac{6PE^{*2}}{\pi^3R^2}\right)^{\frac{1}{3}}$	p0=$\left(\frac{6PE^{*2}}{\pi^3R^2}\right)^{\frac{1}{3}} \frac{1}{F_1^2(\xi)}$
Deformation	not applicable	$\delta_z = \left(\frac{9P^2}{16RE^{*2}}\right)^{\frac{1}{3}}$	$\delta_z = \left(\frac{9P^2}{16RE^{*2}}\right)^{\frac{1}{3}} F_2(\xi)$
Pressure Distribution	$p(x) = p_0\sqrt{1-(x/a)^2}$	$p(r) = p_0\sqrt{1-(r/a)^2}$	$p(x,y) = p_0\sqrt{1-(x/a)^2-(y/b)^2}$
Max. shear stress, $\tau_{1,max}$	$\tau_{1,max} = 0,30p_0$	$\tau_{1,max} = 0,31p_0$	numerical solution
Location of $\tau_{1,max}$, z	z = 0,78a	z = 0,48a	numerical solution

Table 2.1.: Hertz equations for line, point and elliptical contact. For the explanation of the parameters see figures 2.1, 2.2 and 2.3 as well as [8].

$$c = a\left(1 - \frac{Q}{\mu P}\right)^{\frac{1}{2}}, \tag{2.2}$$

and for point or circular contact as

$$c = a\left(1 - \frac{Q}{\mu P}\right)^{\frac{1}{3}}. \tag{2.3}$$

The distribution of the shear stresses in the stick region is given by

$$q_x(x) = \frac{\mu p_0}{a}\left[\left(a^2 - x^2\right)^{\frac{1}{2}} - \left(c^2 - x^2\right)^{\frac{1}{2}}\right] \tag{2.4}$$

for line contact, whereas for point or circular contact one has

$$q_x(x,y) = \frac{\mu p_0}{a}\left[\left(a^2 - r^2\right)^{\frac{1}{2}} - \left(c^2 - r^2\right)^{\frac{1}{2}}\right]. \tag{2.5}$$

The parameter r is defined by $r = \left(x^2 + y^2\right)^{\frac{1}{2}}$. The distribution of tangential traction in the slip region is defined by $\mu p(x,y)$. A relationship between applied tangential load and tangential deformation is given for the circular contact by

$$\delta_x = \frac{3\mu P}{16aG^*}\left(1 - \left(1 - \frac{Q_x}{\mu P}\right)^{\frac{2}{3}}\right), \tag{2.6}$$

with G* being defined as the combined shear modulus of the two bodies (G1 and G2 represent the shear moduli of the two bodies) in contact as

$$\frac{1}{G^*} = \frac{2-\nu_1}{G_1} + \frac{2-\nu_2}{G_2}. \tag{2.7}$$

For tangentially loaded elliptical contacts the results are similar to the circular configuration however, with an elliptic shaped stick zone.

2.4. Application to wheel rail contact

Using the Hertzian approach for analyzing the rail wheel contact is a common method for solving normal contact problems. Of course the assumptions and limitations of the Hertzian theory must be considered:

- Ideally smooth and frictionless surfaces.
- Material stiffness parameters must be identical for both rail and wheel.
- Linear elastic material behavior.
- Constant initial curvature within the contact area.
- Small contact area size in relation to the contacting body dimensions.

Though these conditions are only partly valid for rail-wheel contact this method is often used especially in vehicle dynamics simulations due to the very fast computation times.

When analyzing the contact between wheel and rail a coordinate system is introduced where the x-axis points in rolling direction, the z-axis denotes the normal direction rail upwards and y the lateral direction (figure 2.4). A list of the important parameters of the rail wheel contact is listed in table 2.2.

R	wheel rolling radius	υ_x	longitudinal creep ratio
V	wheel traveling speed	υ_y	lateral creep ratio
Ω	wheel rotational speed	φ	spin ratio
P	normal force	u_x	longitudinal displacement
Q_x	longitudinal creep force	u_y	lateral displacement
Q_y	lateral creep force	s_x	longitudinal normalized slip
M	spin moment	s_y	lateral normalized slip
Δv_i	relative in-plane translation velocity between contacting bodies, i$\epsilon \{x, y\}$	p	contact pressure
$\Delta\omega$	relative rotation velocity between contacting bodies	q_x	tangential stress component in longitudinal direction
a	longitudinal contact ellipse semi-axis	q_y	tangential stress component in lateral direction
b	lateral contact ellipse semi-axis	μ	coefficient of friction
t	time	α	traction coefficient

Table 2.2.: Notation of quantities, wheel rail contact analysis. See also figures 2.1, 2.2 and 2.4.

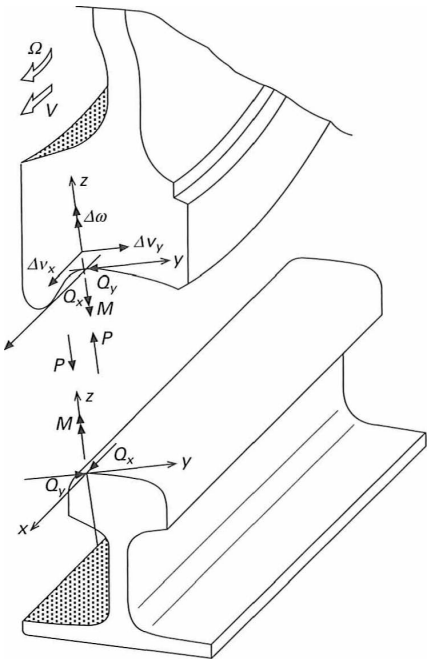

Figure 2.4.: Definition of coordinate systems and parameters in the rail-wheel contact. Detailed description in table 2.2.

According to Kalker [11] *rigid body slip* is defined as the sum of the rolling speed and the circumferential speed of a rigid wheel rolling over a rail. The *true slip* or *slip* is defined as the rigid body slip plus the time derivative of surface material deformation (elastic and or plastic) in direction of the slip. Slip is also defined by Carter [5] as one body sliding over another body. *Creep* is defined as a velocity difference between rolling speed and circumferential speed. If the creep is normalized to the rolling speed this is referred to as *creepage* [12]. Often these terms and definitions are mixed up and are not used in their original meaning.

For the development of creep forces (tangential force) a certain amount of creep is necessary. As listed in table 2.2 three different slip conditions can be found: slip due to longitudinal creep, slip due to lateral creep and slip due to spin creep. Generally the tangential forces depend on the normal load, friction conditions and relative motion between wheel and rail. The creep and spin ratios in the contact depend on the relative velocities normalized to a reference speed (e.g. traveling speed of the train) as

$$\nu_i = \frac{2\Delta v_i}{V + \Omega R},\ i\epsilon(x,y), \tag{2.8}$$

$$\varphi = \frac{2\ \Delta\ \omega}{V + \Omega R}. \tag{2.9}$$

The traction coefficient is defined by the ratio between tangential and normal force as

$$\alpha = \frac{\sqrt{Q_x^2 + Q_y^2}}{P}. \tag{2.10}$$

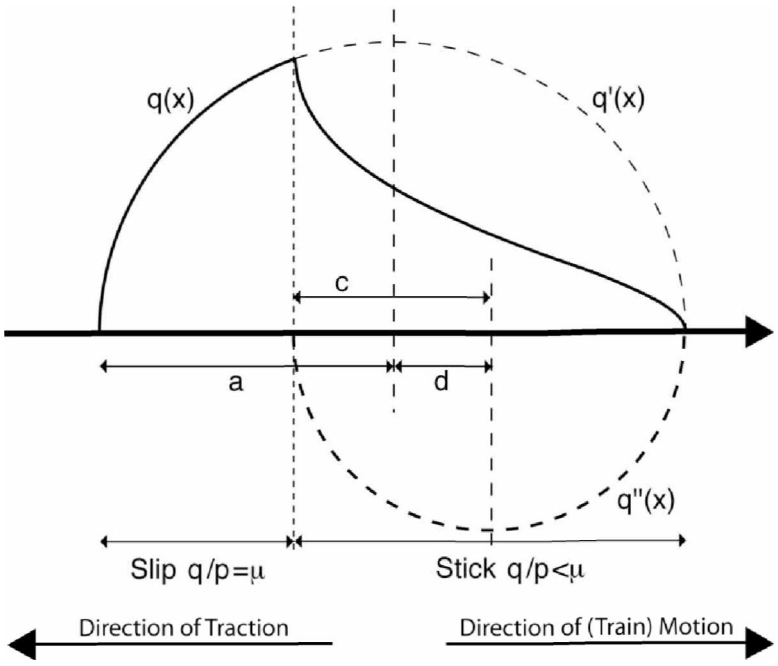

Figure 2.5.: Stick and slip in the contact patch for longitudinal loading according to [5]. Relation of stick and slip zones depend on the applied tangential force Q and the resulting tangential stress q(x) which is limited by the friction (μ) between wheel and rail. Picture taken from [13].

Carter developed in 1926 [5] a creep force law by analyzing locomotive wheels transmitting large traction or breaking forces (only longitudinal creep - figure 2.5). Carter could show that the maximum tangential force is limited by Coulomb's friction law and that at zero slip no tangential force is transmitted (traction - creepage relationship). Between full slip and zero slip there is a relation of stick and slip in the contact patch dependent on the tangential force (see figure 2.6) as

$$\frac{Q_x}{\mu P} = \left\{ \begin{array}{cc} -k\nu_x + \frac{1}{4}k^2\nu_x \mid \nu_x \mid & if\ k \mid \nu_x \mid \leq 2 \\ -sgn\left(\nu_x\right) & if\ k \mid \nu_x \mid > 2 \end{array} \right\}. \tag{2.11}$$

The coefficient k is called Carter creep coefficient. $\frac{Q_x}{\mu P}$ represents the relationship of the normal force and the longitudinal creep force (traction force) limited by the coefficient of friction (see also figure 2.6).

The slip (or true slip) can be defined by the rigid body slip and the surface strain as

$$\begin{array}{l} s_x\left(x,y,t\right) = \nu_x\left(t\right) - \varphi_x\left(t\right)\cdot y - \frac{\partial u_x(x,y,t)}{\partial x} + \frac{1}{V}\cdot\frac{\partial u_x(x,y,t)}{\partial t}, \\ s_y\left(x,y,t\right) = \nu_x\left(t\right) - \varphi_x\left(t\right)\cdot y - \frac{\partial u_y(x,y,t)}{\partial x} + \frac{1}{V}\cdot\frac{\partial u_y(x,y,t)}{\partial t}. \end{array} \tag{2.12}$$

Additionally also Coulomb's friction law is applied as

$$\begin{array}{l} \mid q \mid \left(x,y,t\right) \leq \mu\cdot p\left(x,y,t\right), \\ q = \left[q_x\left(x,y,t\right), q_y\left(x,y,t\right)\right]. \end{array} \tag{2.13}$$

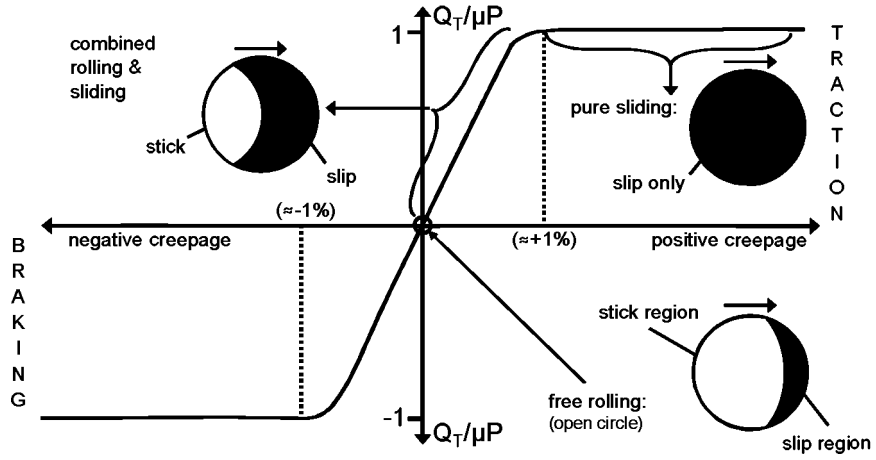

Figure 2.6.: Traction - creepage relationship dependent on tangential force according to [5]. An increase in traction results in an increase in creep. Furthermore with increasing traction also the ratio between stick and slip zone in the contact patch moves towards full slip. Maximum possible traction (at full slip) is limited by the coefficient of friction (μ). Picture (replot) taken from [14].

These calculations are only valid for assumed steady state conditions. In this case the time dependent term can be neglected.

2.5. Numerical solutions

Kalker [15] developed a linear creep theory based on the Carter equations. Kalker considered longitudinal and lateral creep in an elliptic contact patch according to Hertz as

$$\begin{Bmatrix} F_x \\ F_y \\ M \end{Bmatrix} = Gc^2 \begin{bmatrix} C_{11} & 0 & 0 \\ 0 & C_{22} & cC_{23} \\ 0 & cC_{23} & cC_{33} \end{bmatrix} \begin{Bmatrix} \nu_x \\ \nu_y \\ \varphi \end{Bmatrix}. \tag{2.14}$$

c^2=ab and C_{ij}represent the Kalker coefficients (functions of Poisson's ratio and the ratio of contact ellipse semi-axes). Kalker's theory is nowadays widely used in vehicle dynamics applications. Further developments also include non-elliptic contact configurations of elastic bodies and boundary element discretisisation of the contact patch. Kalker's algorithm was included into the CONTACT code [16] that is widely used for simulation. Due to that fact that CONTACT required too much computation time to be included in online vehicle dynamics calculations, Kalker developed a simplified theory based on the concept of a thin elastic layer that is rigidly supported. This algorithm is referred to as FASTSIM [17]. Although this algorithm was originally developed for elliptic contact it can also be applied for non-elliptic contact zones [18]. Besides creep forces FASTSIM can also be used for calculating shear stresses. A constant stress gradient is assumed in the simplified theory until the traction bound (contact pressure times coefficient of friction) is reached. The resulting shear stress assumes the value of that bound limit. The tangential stress distribution is calculated by numerical integration over the contact patch [8].

Improved methods have been developed over time that base on FASTSIM but provide extensions to the original algorithm. These algorithms (iterative or non iterative) divide the contact patch into several strips and provide solutions for each strip (independently or dependently) to provide a solution for non-elliptic curved contact patches. A similar approach was chosen by the "Virtual Vehicle Competence Center" (ViF) for the development of their contact model as a part of a voestalpine co-funded project [19]. Another approach used for simulations of some contact conditions in this thesis was chosen in [20]: the conformal contact (conformal contact: high lateral extension of the contact patch as wheel and rail profiles "fit into one another") between wheel and rail at the test rig of voestalpine was approximated by using two overlapping Hertz ellipses in the multi-body software VAMPIRE (see http://vampire-dynamics.com/). Such multi-body software packages can be used to simulate a whole vehicle running over a railway track. By implementing algorithms like CONTACT or FASTSIM this software can not only provide global outputs like forces, moments or displacements for the wheelsets but can also calculate local conditions for each rail wheel contact (contact dimension, contact force distribution, stresses, creep, slip...) as mentioned above. The partners of voestalpine are using the software packages GENSYS (Chalmers Railway Mechanics Competence Center - CHARMEC, Sweden, http://www.gensys.se/), SIMPACK (ViF, Graz, http://www.simpack.com/) and VAMPIRE (Kelsan Technologies now LB Foster Friction Management, Vancouver, Canada).

If more detailed simulations have to be made the finite element method has to be chosen. With free or commercial available software packages like ABAQUS (see www.simulia.com) it is possible to model the rail wheel contact or specific details of the rail wheel contact very accurately. The problem in applying a FEM simulation to the rail wheel contact consists in the fact that many input parameters (e.g. strain hardening behavior of the material, material characteristics of the strain hardened material like tensile strength or fracture toughness, friction conditions, roughness conditions etc...) are unknown and that the calculation times can go up weeks (dependent on available computation power and complexity of the model) per simulation run. On the other hand these models are not restricted to specific conditions like smooth surfaces or elastic material behavior as some of the other methods as mentioned above. The Material Center Leoben as a partner of voestalpine uses the software ABAQUS to simulate effects in the rail wheel contact [21].

3. Rail damage due to loading

3.1. The shakedown map

Due to the transfer of the axle loads of railway vehicles in the relatively small contact patches (size of a coin) between wheel and rail the rail surfaces are often loaded beyond the elastic limit during their service time. In general when loading a material cyclically the response can be within four possibilities (figure 3.1) [22, 23]. Case I: ideal elastic material behavior which rarely happens in the wheel rail contact. Caste II: if the load exceeds the yield limit of the material plastic deformation takes place. The material will respond with strain hardening and residual stresses will be introduced. Subsequently the material will return to an elastic state after some plastic deformation cycles - elastic shakedown. Case III: if the contact load is further increased a closed loop behavior will develop after some accumulating plastic deformation. The sum of plastic deformation per loop is zero. This material response is called plastic shakedown. Case IV: in every load cycle there is an increment of plastic deformation - this behavior is called ratchetting or cyclic plastic deformation. Due to the permanent plastic deformation the material will finally rapture when the ductility is exhausted.

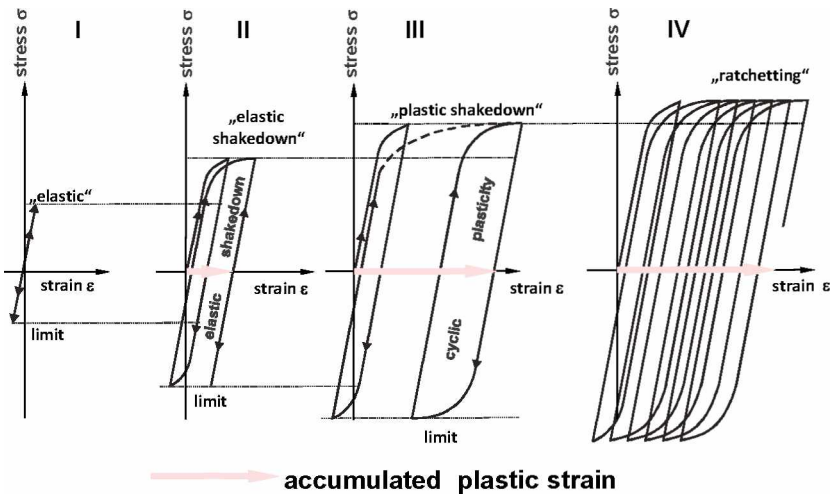

Figure 3.1.: Material response to cyclic loading. I: ideal elastic, II: elastic shakedown, III: plastic shakedown, IV: ratchetting. Picture recreated from [23].

Dependent on the traction coefficient T/N (T: tangential force, also referred to as Q in table 2.2 on page 17, N: normal force, also referred to as P in table 2.2 on page 17) for the elastic cases (I and II in figure 3.1) the maximum shear stress and consequently the fatigue damage of the rail is situated either sub-surface or on the surface (figure 3.2). With a traction coefficient below 0.25 the shear stress maximum is situated below the surface at a maximum depth of approx. z =0.5a (1/4 of the contact ellipsis width 2a) for pure rolling

$\mu = 0$. With an increasing traction coefficient this maximum starts to move towards the rail surface. Above a traction coefficient of 0.25 this maximum will reach the rail surface.

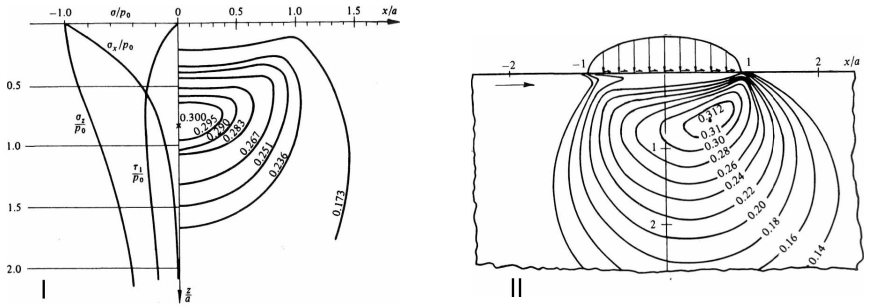

Figure 3.2.: Contact of cylinders in the elastic case; I: subsurface stress state along the axis of symmetry and contour plot of shear stress for T/N=0 (pure rolling); II: contour plot of principal shear stresses for T/N = 0.2. [7].

The shakedown map shows the elastic and shakedown limits (surface and sub-surface) for bodies that are in rolling contact. The basic work was done by Johnson [7] based on Hertzian contact conditions. Figure 3.3 shows a replot of a shakedown map from [24] for a rolling sliding point contact. The x-axis represents the traction coefficient (T/N). The maximum possible traction coefficient is limited by the characteristics of the traction-creepage relationship (i.e. the friction coefficient) - therefore in some diagrams also the friction coefficient is used instead as a label of the x-axis. The y-axis is labeled as the load factor. This load factor consists of the maximum normal contact pressure p_0 divided by the material parameter k_e that represents the shear yield strength of the rail material ($p_0/\ k_e$). The lines within the diagram separate the different material response areas and were derived by shakedown theorems. The green line represents the transition from elastic material response to elastic shakedown. The horizontal blue line separates plastic shakedown from elastic shakedown. Finally beyond the red line only ratchetting material behavior will occur. The transition from subsurface to surface induced damage is indicated by blue vertical lines. With reference to the shakedown map damage can be mitigated or reduced for a given rail-wheel contact condition in several ways:

- Traction coefficient: by applying a lubricant to the gauge face of the rail or a friction modifier to the top of rail the maximum possible traction is reduced (moving along the x-axis from right to left). The friction modifier does also have an influence on the curving behaviour of a vehicle therby weakly reducing the maximum contact pressure p_0.
- Rail material: using a heat treated rail grade instead of an as-cooled grade the shear yield strength is increased resulting in a reduction of the load factor (moving down along the y-axis).
- rail and wheel profiles: by optimizing rail and wheel profiles it is possible to reduce the maximum contact pressure reducing also the load factor (y-axis).

In practical every day railway operation these three methods are used to reduce rail damage by rail grade selection (k_e), preventive or corrective grinding (p_0) and friction management (T/N).

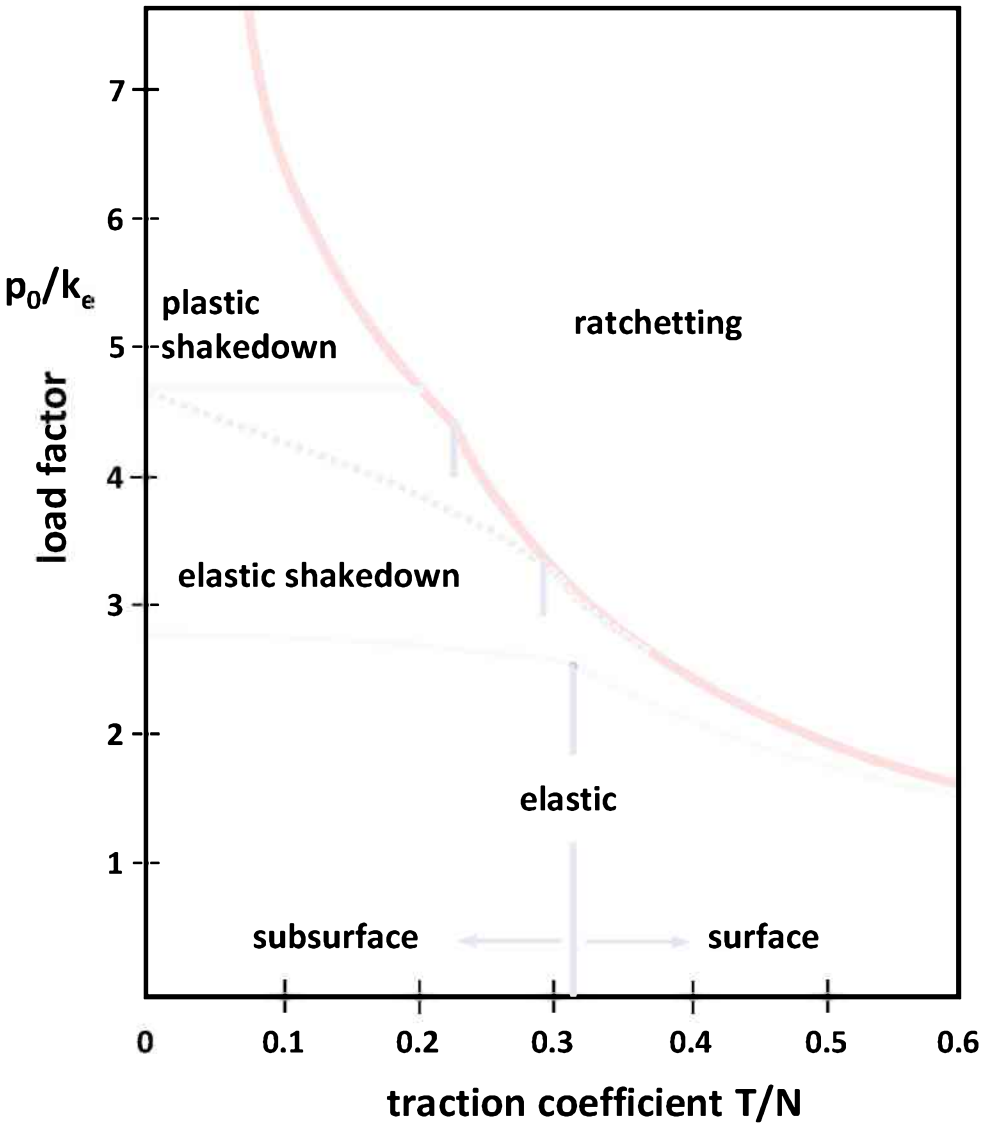

Figure 3.3.: A shakedown map for rolling-sliding contact representing different material behavior areas (elastic, elastic shakedown, plastic shakedown, ratchetting). Replotted from [24].

3.2. Wear

As both rolling and sliding occur in the rail wheel contact one of the most important damage mechanisms is wear. According to [25] wear is defined as the loss of material from a surface, transfer of material from one surface to another or movement of material within a single surface. One of the widely used physical models for wear between two sliding bodies was introduced by Archard in 1953 [6] as

$$V = K\frac{Nl}{H}. \tag{3.1}$$

He V is defined as the worn material volume, N as the normal load applied to the surface by the counter body, l as the sliding length and H as the material hardness. The parameter K is called the wear coefficient (dimensionless) and gives and indication of the severity of the wear process. The variation of the the wear coefficient and its relation to different wear classifications can be seen in figure 3.4.

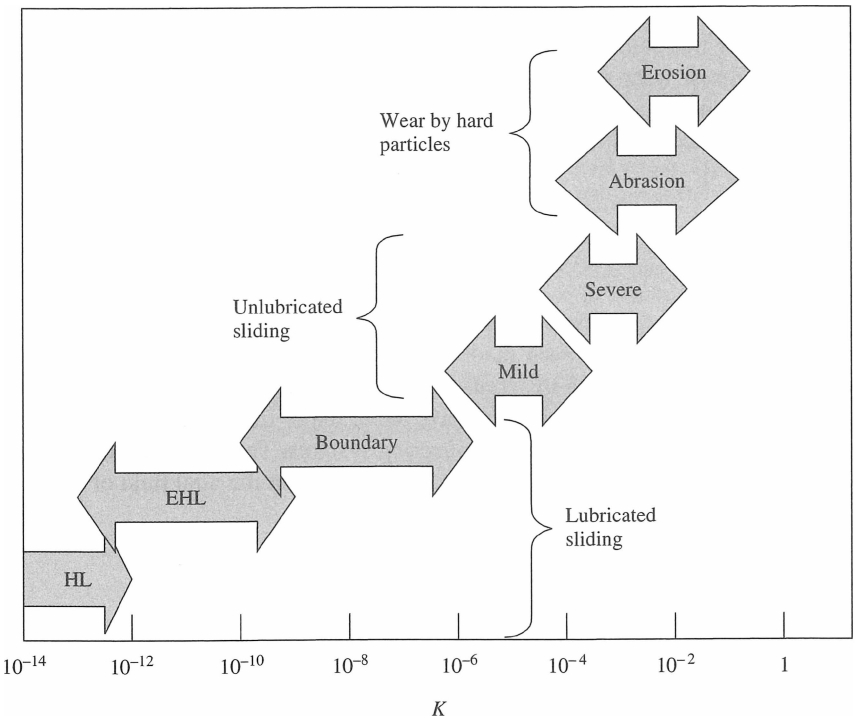

Figure 3.4.: Schematic relationship of the range of the wear coefficient K and different wear classifications. HL: hydrodynamic lubrication, EHL: elastohydrodynamic lubrication [25].

For the rail wheel wear often the terms mild and severe wear are used. Mild wear is defined [26, 23] as a mainly oxidative process with growth and spalling of oxides at the surface asperity level. There is a continuous process of forming and removing of this oxide layer in the wheel rail contact (see also third body layer in chapter 4). Mild wear conditions in the wheel rail contact can be achieved by material choice, profile optimization and friction management [27]. Severe wear will result in rough or scored surfaces. The oxide layer will be

destroyed and particles will be removed from the rail surface. Direct metal to metal contact will result in excessive shear deformation of the surface inducing cracks that grow parallel to the rail surface and finally lead to delamination of bigger surface areas (small plates) [27]. The different wear modes can be plotted in so called wear (coefficient) maps that provide a wear overview in relation to the parameters contact pressure and sliding speed [9]. Besides classifying wear according to its severity also a classification according to the fundamental mechanisms is possible [9]:

- Adhesive wear occurs due to adhesive interaction of two surfaces. This wear mechanism is often associated with severe wear as worn surfaces often appear scuffed and scored.
- Abrasive wear is produced by scratching of hard particles along a surface. The particles generated by corrosive wear (hard iron oxides) can result in abrasive wear when they move through the rail-wheel contact.
- Corrosive wear is a consequence of the chemical reaction of the surface with the environment. This will form a reaction layer on the rail surface that will be again worn off by mechanical action in the wheel-rail contact. As mentioned above this wear mechanism is associated with the mild wear regime.
- Surface fatigue wear is characteristic of rolling contact. Pits and flakes will form on the rail surface. Due to repeated high contact stresses the rail surface becomes fatigued.

4. Friction

4.1. Friction conditions in the rail-wheel contact

Leonardo DaVinci was the first person to state a friction law. As it was only published in his personal notes it was rediscovered by Amonton and further developed by Coulomb as follows: [28]

- Friction in general is defined as the force resisting a relative lateral (or tangential) motion of solid surfaces.
- The friction force is proportional to the normal load ($F = \mu \cdot N$).
- The friction force is independent on the contact area of the two bodies.
- The friction force is independent of the sliding velocity.

These general statements cover both rolling and sliding friction. The friction conditions between wheel and rail have a huge impact on traction and breaking capabilities of a train. As shown in figure 2.5 in chapter 2 the contact patch is divided into stick and slip regions (dependent on the tangential force). In [29] and [30] a third body layer concept was introduced. A third body layer is a layer of material that may separate wheel and rail and it may influence the friction conditions between wheel and rail by its rheological behavior. The third body layer approach was adopted by the NRC (National Research Council, Canada) [31] and possible variations of the composition of the third body layer were analyzed. The predominant constituent of the layer is fine iron oxide powder. Furthermore, there are environmental contaminants such as leaves and dust. Also leaking transportation good can cause a contamination (coal, sulphur, grain ...). Sanding from locomotives will add silica to the rail wheel contact. Furthermore also intentionally applied materials like oil and grease for flange lubrication will contribute to the layer. Figure 4.1 summarizes the influencing factors on the formation of the third body layer between wheel and rail.

Another way of looking at the effects within the rail-wheel contact with reference to the third body layer is the so called "bathtub model" [31]. The wheel rail interface is represented by the content of the bathtub. A mixer/heater in the bathtub represents the effects caused by the wheel loads. Several drains simulate the consumption/decomposition of the third body layer. Depending on what tap is open or closed and on what drain is open or closed the composition of the third body layer can vary thereby directly influencing the friction between wheel and rail.

It is assumed [31] that the third body layer typically consists of deformed asperities (surface roughness of wheel and rail), wear particles and other debris. When traction and extreme pressure are applied to the layer it will start to deform first elastically (shear module G) and then plastically (plastic modulus k) - figure 4.3. It is assumed that the layer is incompressible in z-direction. If the elastic limit is exceeded the increasing shear stress within the layer can be accommodated in several ways (shear stress accommodation mechanism):

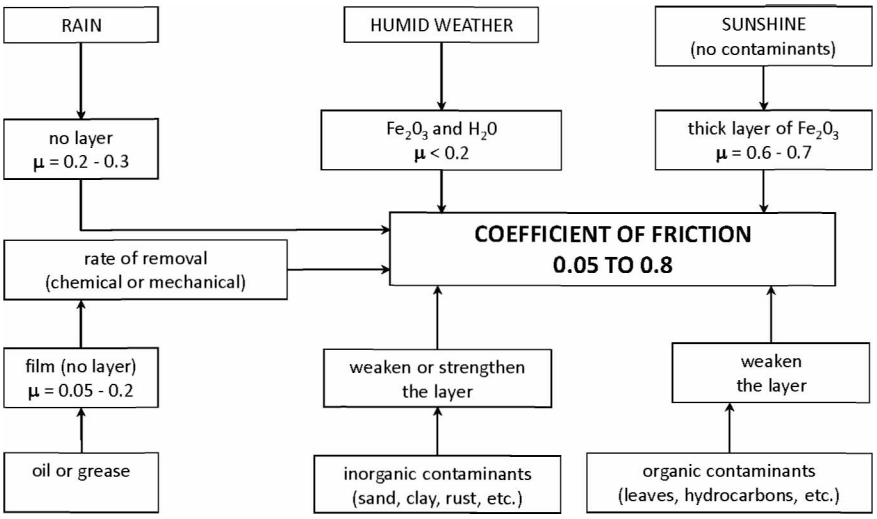

Figure 4.1.: Factors that influence the composition of the third body layer and the friction conditions between wheel and rail [31].

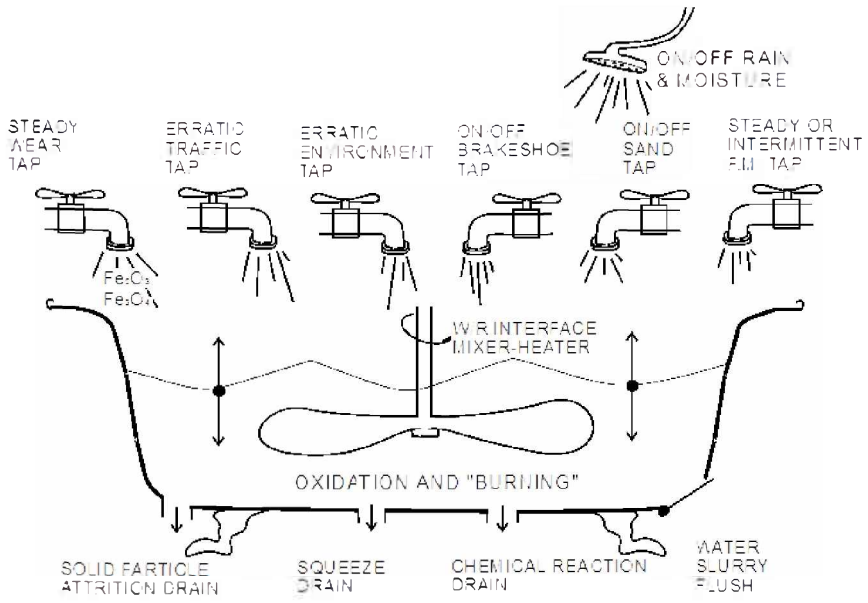

Figure 4.2.: Bathtub model of the rail-wheel interface developed by Joe Kalousek. The content of the bathtub represents the interface (third body layer). Loading is simulated by the mixer/heater in the bathtub, the taps represent different sources of third body materials and the drains simulate the consumption/decomposition of the interface materials [31].

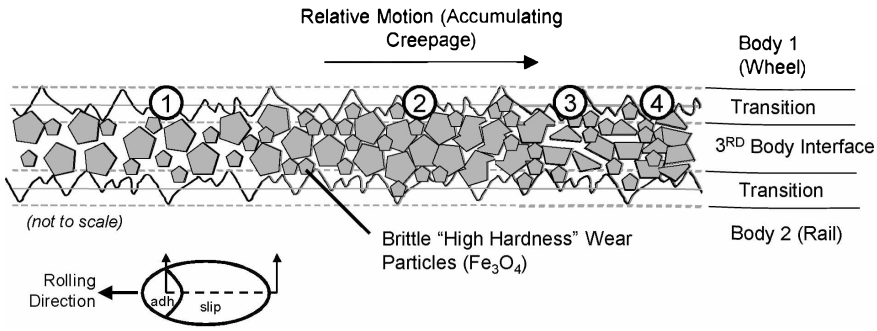

Figure 4.3.: Third body layer model - shear deformation accommodation mechanism according to [31]. (1) rolling of particles, (2) elastic deformation, (3) breaking, (4) void collapse. Drawing by LB Foster Friction Management.

- The particles in the layer will start to roll against each other.
- Particles will start to sever and form new surfaces.
- The void of third body particles will collapse within the layer.

The composition and the properties of the layer particles will have a major influence on the wheel/rail friction characteristics and will govern the response of the layer to the wheel/rail loading. Looking at the traction creepage curve (figure 4.4) three general cases are possible beyond the point of creep saturation: positive friction, neutral friction and negative friction (the typical case for steel and iron oxides) [32].

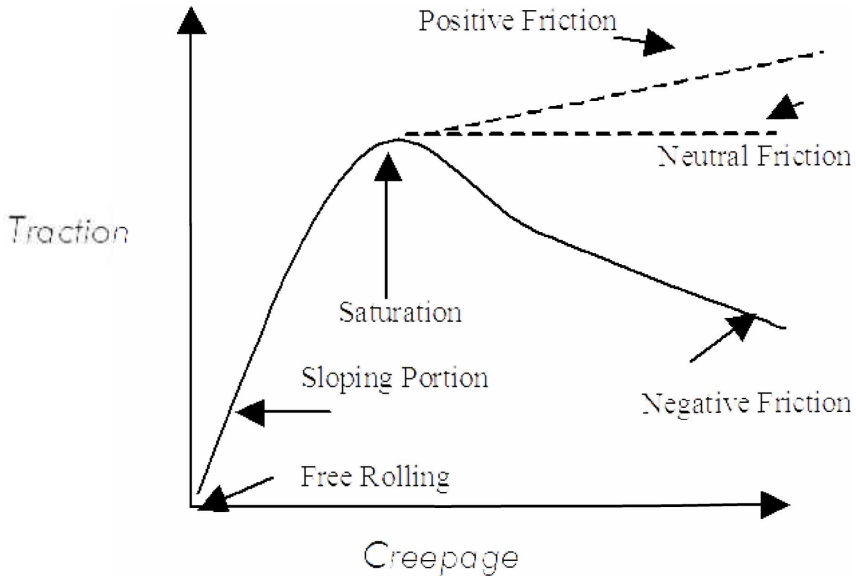

Figure 4.4.: Possible traction - creepage relationships in the wheel rail contact beyond the creepage saturation point [32].

4.2. Friction Management

According to [32] friction between wheel and rail has an influence on wear, RCF, fuel efficiency, flanging noise, squealing noise, lateral forces, corrugation development, hunting of railway vehicles (swaying motion of the railway vehicles), derailment potential etc... Depending on the position on the rail different friction target levels are required (figure 4.5):

- High rail (outer rial in a curve) gauge face (GF) / gauge corner (GC) friction in curves should be as low as possible, < 0.2. This friction level should be maintained around the full length of the curve.
- Top of both rails should target a coefficient of friction (μ) of 0.35 in both curves and tangent. TOR (top of rail) friction should neither be less than 0.25 nor greater than 0.4.

Figure 4.5.: Friction target on the rail surface of high (outer rail in a curve) and low rail (inner rail in a curve) according to [32]. Picture provided by LB Foster Friction Management.

Friction Management is the application of the correct friction control agent (in a necessary amount) to the right location on the rail (or wheel) in the right time [31]. Using gauge face greases has been a common practice for reducing gauge face wear in the wheel rail contact since the early days of the railways [33]. If lubricants (like a gauge face grease) were applied to the top of rail, the traction and braking capabilities of a train would be drastically reduced (very low friction coefficient) imposing a safety risk to railway operations. Therefore Kelsan Technologies Inc. (now LB Foster Friction Management) developed a Friction Modifier that allows one to adjust the friction on the top of rail to the suggested values around 0.35 and generates positive friction characteristics between wheel and rail (see figure 4.4). The friction modifier consists of an engineered water based suspension of solid particles and can be applied to the rail wheel contact zone by wayside applicator bars or by vehicle mounted spray systems. Older versions of the friction modifier are also available as solid sticks that are applied to the wheel tread by brackets. After the application of the liquid form the water evaporates and a thin (sub μm scale) solid film remains in the wheel rail contact zone. The friction modifier particles interact with the existing third body particles by providing a composite shear displacement accommodation mechanism. Besides the reduced μ (0.35) also stick-slip effects (curve squeal noise, corrugation development) associated with

negative friction characteristics are overcome by the positive friction characteristics of the friction modifier [34]. The technology is nowadays widely used by North American heavy haul lines to reduce the fuel consumption of their trains. Fuel reductions of 10% or more are reported for territory wide introduction of Friction Management [35, 36]. Other fields of application deal with corrugation prevention, extension of grinding cycles or noise mitigation [37, 38, 39, 40].

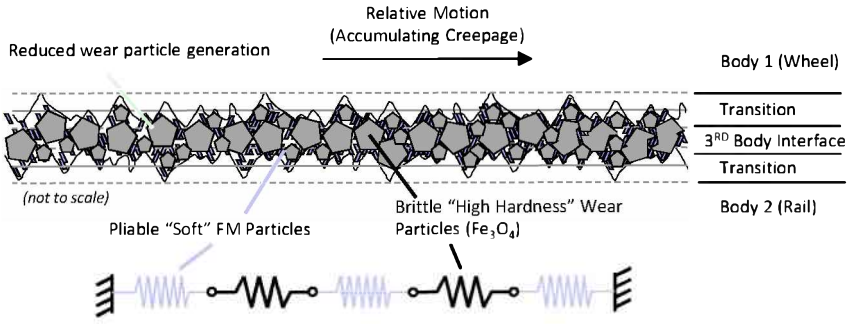

Figure 4.6.: Interaction of the friction modifier (FM) particles with the existing third body particles. FM particles and third body materials provide a shear displacement accommodation mechanism (spring model) that result in a positive traction creepage relationship. Drawing provided by LB Foster Friction Management.

5. Rolling Contact Fatigue

Rolling contact fatigue (RCF) is a family of damage phenomena that appear on and in rails due to over-stressing of the rail material [41]. The damage can either develop at the surface or sub surface as explained above (section 3.1). Due to the repeated loading cracks will form on the rail in the contact zone and will subsequently grow. Beyond safety considerations this problem is also associated with substantial economic costs for maintenance actions and rail renewals. In chapter 3 the general formation of damage is discussed. If a crack has initiated on the rail surface three different crack growth phases were identified in [42] - see figure 5.1. Phase I describes the initiation (ratchetting, shakedown theory) of cracks and their early growth dominated by the formation of micro-cracks in the highly deformed surface layer. In the second phase several mechanisms are postulated that provide further crack growth. Besides shear crack growth due to the contact loading, also fluid assisted crack growth mechanisms may be operative. A fluid can be entrapped and compressed inside a crack and thereby increases the stress intensity factor of the crack and increases the crack propagation rate. Also a mechanism of direct hydraulic transmission of the contact pressure to the crack faces without entrapment of the fluid is proposed. Finally crack face lubrication by liquids or by solid particles can reduce the crack face friction and thereby increase the crack growth rate drastically. In Phase III the crack has reached a length in the order of 10s of millimeters and is driven by the bulk stresses in the rail like bending stresses or thermal stresses. In this phase the crack is not manageable any more, rail breakage is immanent and the only solution is provided by rail exchange.

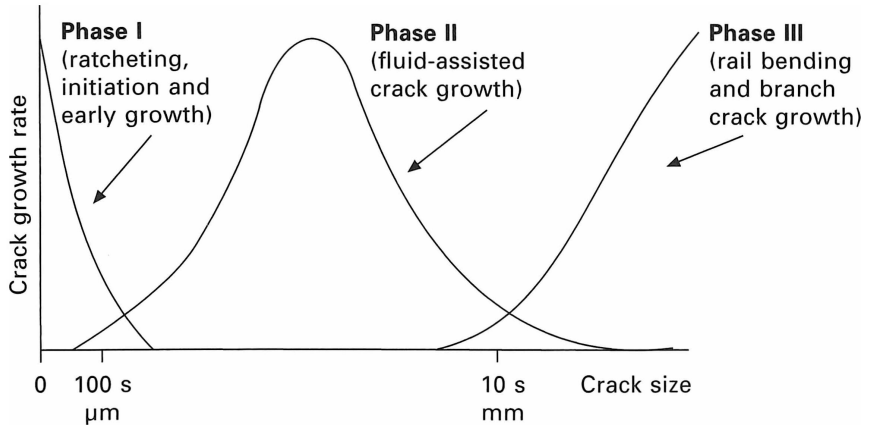

Figure 5.1.: Phases of crack growth according to [42]. For each phase different crack growth mechanisms are dominating.

There is also an interaction / competition between wear and RCF. If the wear rate is higher than the crack growth rate already initiated cracks will be removed by material wear before they can start to grow. If the crack growth rate is higher than the wear rate net crack

growth will take place. The condition where the crack growth rate and the wear rate are balanced out is called "magic wear rate" [43]. At this point no material waste will be caused by unnecessary high wear rates and on the other hand no cracks will form on the rail surface. Reaching the condition of magic wear rate by natural occurrence is almost impossible. Therefore, this terminology is now used for a preventive maintenance concept, when short cracks are regularly removed by grinding operations and rail life is extended - see figure 5.2. Finally it has to be noted that most of the ideas that try to explain the RCF phenomenon are hypotheses that wait for their proof.

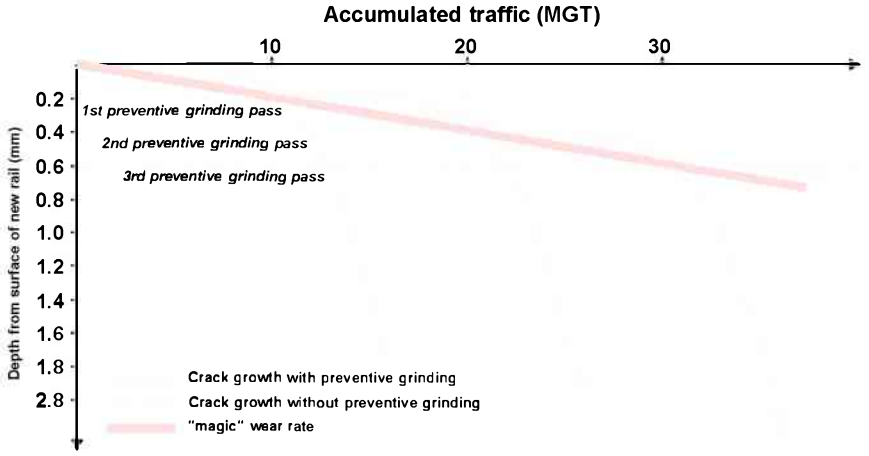

Figure 5.2.: The maintenance concept of the "magic" wear rate. Preventive grinding intervention keeps artificial wear in balance with crack formation and growth. Picture replotted from [43].

5.1. Main categories of RCF defects

This section is based on the UIC Code "Rail Defects" [44] and the track experience of the author. Figure 5.3 shows the dependence of the damage mechanisms on track radius (taken from [45]).

5.1.1. Wear

Wear has already been treated in section 3.2 but for completeness reason this topic is also shortly treated here. Wear is the predominant form of damage in sharp curves (European mixed traffic conditions in general for curves sharper than approx. R=700m - see figure 5.3) and is a general problem for heavy haul operations. Different infrastructure owners have different rail wear limits that dictate the according rail exchange. Wear can be mitigated by heat treated high hardness rail grades, by Friction Management, by rail and wheel profile optimization and by track geometry optimization. Figure 5.4 shows a typical wear pattern of a rail in heavy haul operations.

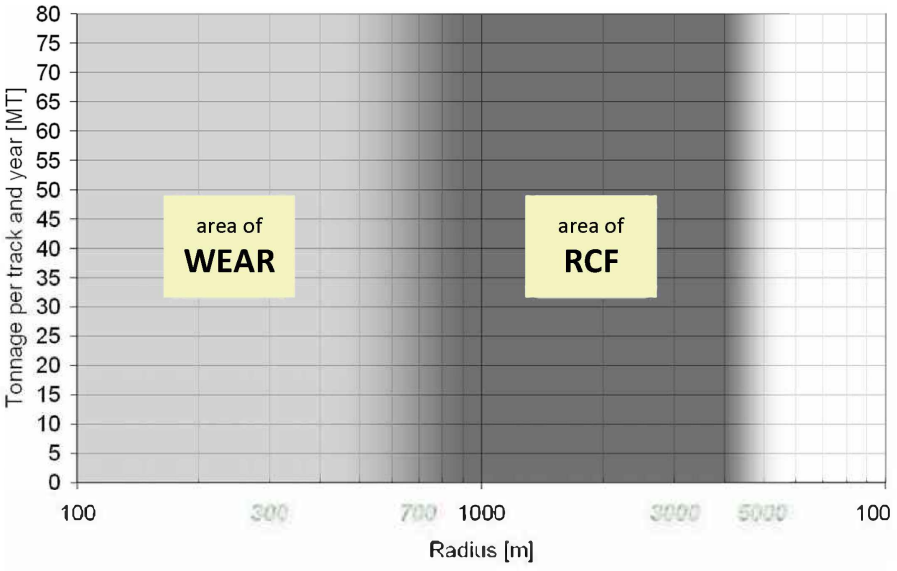

Figure 5.3.: Predominant degradation mechanism based on track curvature [45].

Figure 5.4.: Example of worn rail in heavy haul operations. Photo by voestalpine.

5.1.2. Corrugation

Corrugation can be considered for a special periodic form of wear and is often classified into short and long wave corrugation. However, a more detailed classification by wavelength fixing and damage mechanisms results in 6 different types [46]. Corrugations cause high dynamic forces between wheel and rail, damage the ballast and/or other track components and result in noise. The main reason for the periodicity are resonances of the unsprung mass of the vehicles on the track stiffness (this is referred to as wavelength fixing mechanism) and other resonance phenomena. As the topic of corrugation would go beyond the scope of this thesis due to its complexity actual research work is recommended for further details [46]. Corrugation can be prevented by wear resistant rail grades, friction management or by special vibration absorption systems like the use of rubber booted sleepers. Grinding can be seen as a corrective measure against corrugation. Figure 5.5 shows a typical form of corrugation on a low rail in a curve.

Figure 5.5.: Corrugation on a low rail in a curve, metro system in Scandinavia. Picture provided by P. Torstensson from CHARMEC.

5.1.3. Head Checks

Head Checks are one of the main topics of this thesis. Head Checks are also referred to as gauge corner cracks periodically formed at the gauge corner that grow following a shallow angle into the rail material. The periodicity is dependent on the rail grade and the loading conditions. In a certain depth the cracks can sometimes turn down and cause a detail fracture (complete fracture of the cross section) of the rail. Head Checks are typically found on the high rail in medium to shallow curves (typically with a radius $>$ 700-1200m). Sometimes periodic cracks can also be found on the rail head caused by high traction forces (station exits, signals etc). Theses cracks are sometimes also referred as Head Checks or transverse Head Checks and are treated by a combination of preventive maintenance and appropriate rail grade selection. Figure 5.6 shows some typical forms of Head Checks.

Figure 5.6.: Typical Head Checks at the gauge corner of the rail head. Photo by voestalpine.

5.1.4. Spalling

If Head Checks do not turn down, several neighboring cracks will combine and can cause rail material to break out of the rail surface. This form of defect is called spalling. Figure 5.7 shows some characteristic spalling in combination with Head Checks.

5.1.5. Shelling

Shells are mainly a problem in heavy haul operations. Cracks initiate beneath the surface at non-metallic inclusions at the gauge corner of the rail. An elliptical (shell like) shaped crack will grow with characteristic beach marks starting at these inclusions. First it will grow mainly parallel to the rail surface. When reaching a critical length the crack will turn down and cause a detail fracture of the rail (complete transverse rail fracture). With modern steel production (vacuum treatment) and state of the art rail inspection techniques at the rail production plants this failure nowadays only found in track in rails of older manufacturing date. Figure 5.8 shows typical shelling and a detailed fracture of a rail caused by a shell defect.

5.1.6. Squats

Squats pose at the moment a huge problem in mixed and passenger traffic operations. They are classified in three categories (light, medium and severe)[47]. In their final stage they cause a characteristic widening of the contact band with a visible v-shaped crack on the rail surface. Underneath the rail surface the crack grows in a bowl like shape towards the other side of the rail head where the crack may return to the surface again. The cracks can reach a depth of 8-10mm and sometimes can lead to rail breaks. They can appear as singular events or in an epidemic form. The formation is associated with low wear regimes, high traction forces, locally changing friction conditions and vertical dynamics caused by high stiffness of boogies and/or track structures. They are difficult to detect in their early stage and if they have grown too deep the only economic way of correction is rail exchange. If they have not

Figure 5.7.: Spalling and Head Checks on a badly worn rail head. Photo by voestalpine.

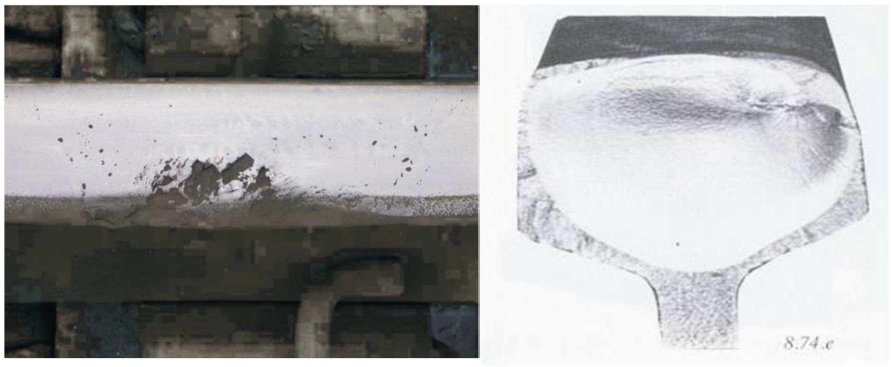

Figure 5.8.: Shelling at the gauge corner of the rail and detail fracture (complete transverse rail fracture) of a rail due to a shelling defect. Photos by voestalpine.

yet grown beyond 2-3mm they can be milled or ground away. This topic is at the moment a major concern of worldwide R&D work. For more detailed information see [48, 49, 50]. Figure 5.9 shows the three classes of Squats. Also this defect goes beyond the scope of this thesis.

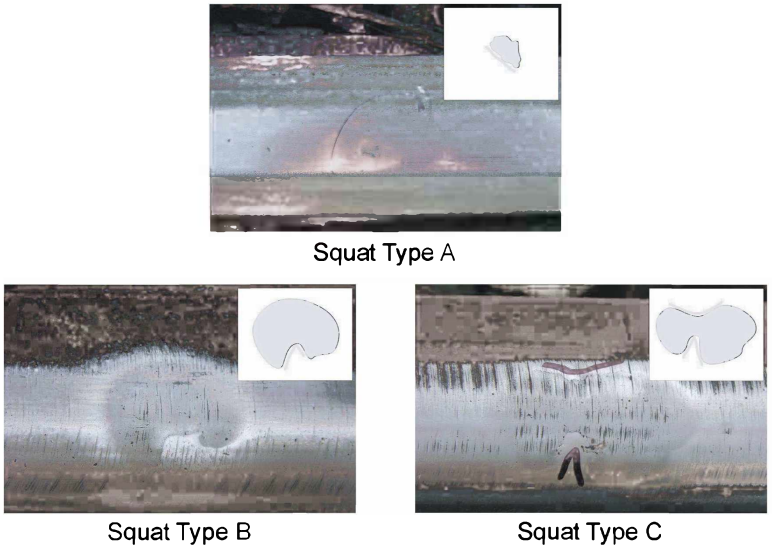

Figure 5.9.: Categories of Squats. Squat A: surface depression with small crack. Squat B: v-shaped surface crack with large surface depression due to sub-surface crack below. Squat C: full-size Squat with v-crack and opposite surfacing crack. Photos by voestalpine.

5.1.7. Belgrospies

Belgrospies are a defect associated with dedicated high speed lines with train speeds higher than 200km/h [51]. They form as crack nests at corrugation peaks. They can be treated by corrective or preventive grinding. Figure 5.10 shows a typical Belgrospie defect.

Figure 5.10.: Belgrospie defect on a high speed line. Photo provided by voestalpine.

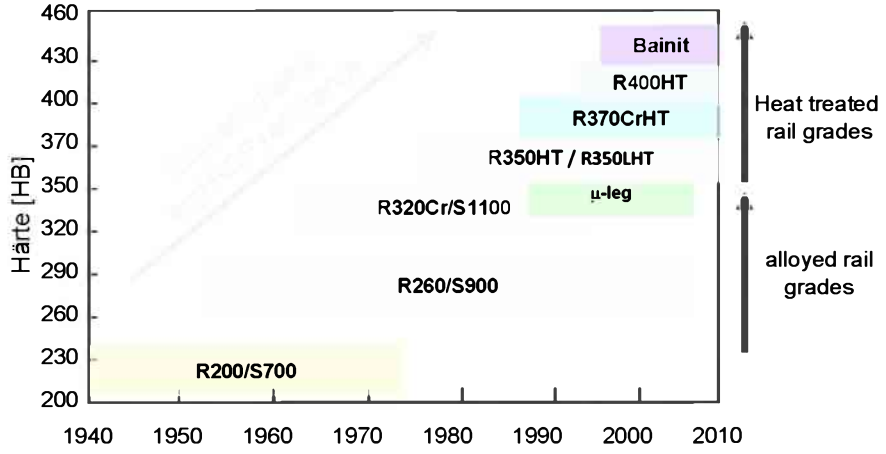

Figure 5.11.: Rail grade development since 1940. Drawing by voestalpine based on [52].

5.2. Rail grade development

Rail grade development has always been driven by extending the rail life and thereby saving costs. During the last two centuries the steel producing processes were continuously improved: puddle steel, Bessemer steel, Siemens Martin Steel and finally Linz-Donawitz Steel (oxygen blowing steel). The improvement in steel quality resulted in an improvement of steel strength, reduction of sudden rail failures and increase of wear resistance. Also developments in secondary steel making processes like vacuum degassing further improved the cleanliness of the rail steel [2]. With the improvement of the steel production processes the chemical composition of the rail steels was also improved. Alloying elements like Mn and Si were added to improve the mechanical properties of the rail steel and the levels of the unwanted elements like phosphorous and sulfur were reduced. Since the 1980's, more focus was put towards the RCF resistance of rail steels. This lead to the development of heat treated pearlitic steels and bainitic steels for rails. Figure 5.11 shows the general development of rail steels since 1940 [52, 2].

5.2.1. Pearlitic Rail Steels

Most rails nowadays are manufactured from low alloy carbon-manganese steel with medium to hypereutectoid levels of carbon (according to the Fe-C diagram). The typical structure of such a steel would be pearlite (lamella structure of soft, ductile ferrite and hard, brittle Fe_3C Carbide) with varying contents of pro-eutectoid ferrite. The pearlitic microstructure provides a good balance of hardness and strength with toughness and ductility. In the last century the rail grade development was targeted at increasing the material strength without reducing the toughness properties. This was first done by increasing the carbon content to the eutectoid concentration (R200 to R260 rail steel). Later alloying elements like Cr were added to further improve the rail hardness (R320Cr). As the alloying elements had a negative influence on the weldability of rails and also increased the rail price heat treatment of rails was introduced in the late 1980's [53]. By accelerated and controlled cooling of the rail head the lamella distance in the pearlitic structure is reduced and thereby the hardness of the material increased with only minor reduction of toughness properties. The heat treatment

process can be done either by using the rolling heat of the rail (in line process) or by reheating the rail head prior to the cooling process (offline process). For the cooling process several methods are in use at the moment: cooling by air, water mist, water spray and quenching bath. voestalpine Schienen uses an inline quenching bath process to produce HSH® (Head Special Hardened) fine pearlitic rail grades with a hardness between 350BHN and 440 BHN. The latest development in that area are so called hypereutectoid rails with a carbon content of up to 1% and hardness levels of 400-440BHN. Figure 5.12 gives an overview of actual pearlitic rail grades according to EN13674-1:2011 [54]. Figure 5.13 shows the European rail grade recommendation that was an output of the Innotrack project [45] and is based on yearly tonnage and curve radius.

Steel Grades		Chemical Composition [% by mass]				Mechanical Properties		
		C	Si	Mn	Cr	R_m [MPa]	A_5 [%]	Hardness [HBW]
Standard Rail Grades	R200	0.40 – 0.60	0.15 – 0.58	0.70 – 1.20	≤ 0.15	≥ 680	≥ 14	200 - 240
	R220	0.50 – 0.60	0.20 – 0.60	1.00 – 1.25	≤ 0.15	≥ 770	≥ 12	220 - 260
	R260	0.62 – 0.80	0.15 – 0.58	0.70 – 1.20	≤ 0.15	≥ 880	≥ 10	260 - 300
	R260Mn	0.55 – 0.75	0.15 – 0.60	1.30 – 1.70	≤ 0.15	≥ 880	≥ 10	260 - 300
	R320Cr	0.60 – 0.80	0.50 – 1.10	0.80 – 1.20	0.80 – 1.20	≥ 1,080	≥ 9	320 - 360
Heat Treated Rail Grades	R350HT (350HT HSH®)	0.72 – 0.80	0.15 – 0.58	0.70 – 1.20	≤ 0.15	≥ 1,175	≥ 9	350 - 390
	R350LHT (350LHT HSH®)	0.72 – 0.80	0.15 – 0.58	0.70 – 1.20	≤ 0.30	≥ 1,175	≥ 9	350 - 390
	R370CrHT (370LHT HSH®)	0.70 – 0.82	0.40 – 1.00	0.70 – 1.10	0.40 – 0.60	≥ 1,280	≥ 9	370 - 410
	R400HT (400UHC HSH®)	0.90 – 1.05	0.20 – 0.60	1.00 – 1.30	≤ 0.30	≥ 1,280	≥ 9	400 - 440

Figure 5.12.: Pearlitic rail grades according to the European specification EN 13674-1:2011[54]..

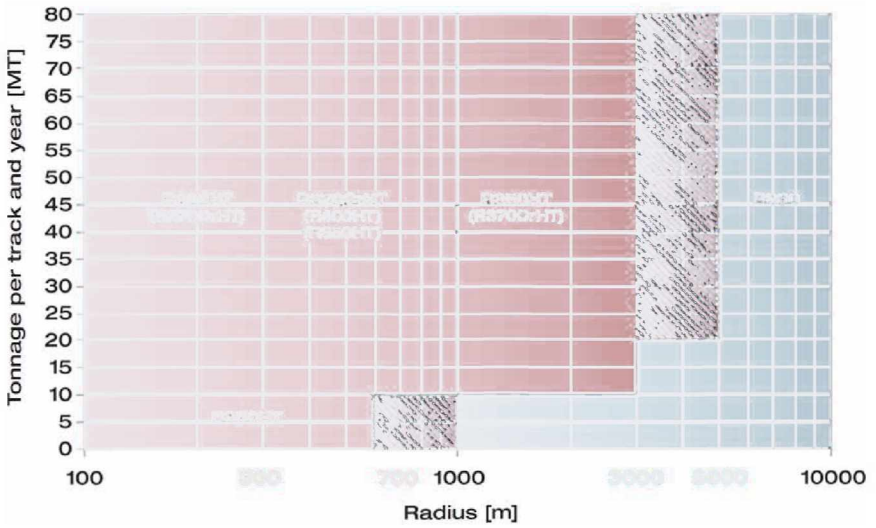

Figure 5.13.: European rail grade recommendation, output of the Innotrack project [45]. Picture by voestalpine.

5.2.2. Bainitic Rail Steels

Heat Treated pearlitic rail steels provide excellent wear resistance but they still develop RCF defects that are related to high maintenance costs. With the idea of rail heat treatment soon the idea of producing bainitic rails was born as this type of microstructure was expected to have improved RCF resistance. The classical bainitic structure is also a two phase material of ferrite and cementite but due to higher cooling rates no longer forms a lamella structure any more (upper bainite: carbide precipitation along ferrite plates, lower bainite: carbide precipitation with ferrite plates) [55]. By adding alloying elements like Mo, Cr or B, carbide free bainitic steels can be produced by natural air cooling. This bainitic structure consists of ferrite and MA phases (phase of retained austenite and martensite) [56]. Recent developments aim at producing a multi-phase bainitic structure that contains phases of ferrite, ferrite and Fe_3C and minimal contents of MA phases. The MP type of bainite can either be produced by an advanced inline heat treatment process or by alloying and air cooling followed by a cost intensive post production annealing process [57]. Laboratory and track test results so far support the advanced RCF resistance of bainitic rail grades. However, the wear resistance is reduced by a factor of two compared to pearlitic rail grades with the same hardness level [57]. The bainitic rail grades analyzed in this thesis represent the "lower bainite" type and the "carbide free" type (annealed and as-produced).

Part II.

Test procedure and examination methodology

6. Rail-wheel test rig

6.1. Background

In 1999 voestalpine Schienen GmbH und Co KG developed a full scale test rig that should be capable of provoking a "vertical split head" failure in rails. For that reason a very high vertical force was assumed to be necessary resulting in the rig design of applying the vertical load through a lever (factor 2). As no vertical split head failure was produced even with vertical loads up to 100t, the test rig was altered to be able to apply also a lateral load and to be able to adjust an angle of attack between wheel and rail. During work published in the author's diploma thesis [58] a hydraulic motor was attached to the wheel axle in order to be able to apply a longitudinal loading. But due to slip control issues and limited hydraulic power this extension of the test rig never generated the expected functionality with respect to longitudinal loading. Since then several minor updates (e.g. displacement sensors, new PLC, computer visualization etc.) have been applied to the test rig, due to malfunctions or out of the necessity of providing new or improved functionality.

6.2. Test rig characteristics

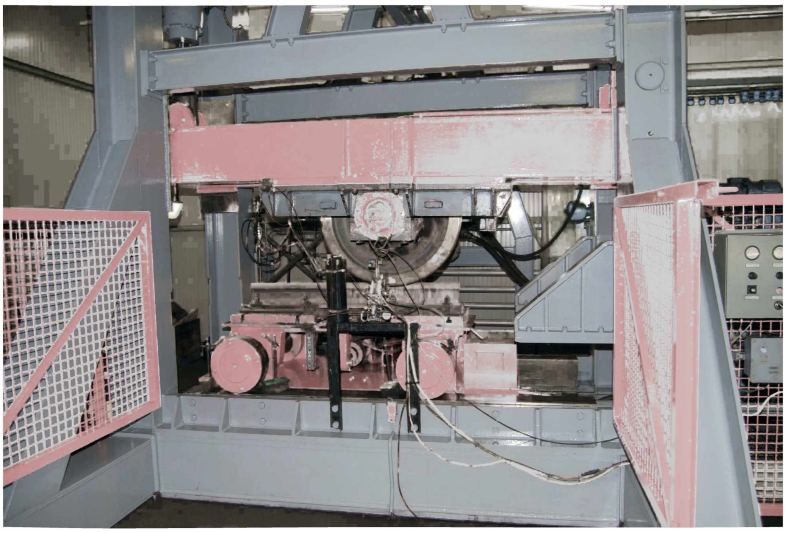

Figure 6.1.: Full scale rail wheel test rig at voestalpine Schienen GmbH, linear test rig concept.

The test rig at voestalpine Schienen GmbH represents a linear test rig concept. A single piece of rail with a length of up to 1.5m moves linearly back and forth underneath a full size railway wheel. The rail is attached to a rail carriage which is moved by a hydraulic

system. Picture 6.1 gives an overview of the test rig. The rail is fixed to a steel base plate by conventional rail clamps. The base-plate itself is directly attached to the carriage table. Elastic layers between rail and base plate could be used to simulate some track elasticity but such layers were not used for the the testes described in this thesis. The following forces can be applied to the rail wheel contact:

- A vertical force of up to 100t can be applied through the wheel by a lever that provides a factor of two load increase compared to the load that is provided by the vertical force hydraulic cylinder (up to 50t). The minimum load is limited to 12t due to constructive restrictions.
- A lateral force up to 15 t is provided by pressing the rail against the wheel flange. The upper part of the carriage table can be moved by a hydraulic cylinder in lateral direction.
- A theoretical longitudinal force of up to 3.5t should be applied through a hydraulic motor on the wheel axle. Due to slip control problems and due to limited hydraulic power only either no slip or full slip (wheel-burn) could be produced.

An angle of attack can be adjusted between wheel and rail in order to simulate curving. This angel can be set to 0, 0.5° or 1° at preset positions. Angles in between can be adjusted by fixing the wheel at a previously measured angle. The rail inclination (rail cant) is adjustable by using an appropriate base plate or by putting a wedge between base plate and rail. Typical inclinations of rails in track are 1:40 or 1:20 [59]. The test rig also provides means to alter the friction conditions in the wheel rail contact:

- Rain simulator: a mixture of water and compressed air can be sprayed directly to the wheel-rail contact via an adjustable spray nozzle. The spray intensity can be adjusted manually by a water valve. The spray interval (every x cycles) and spray duration (no. of cycles with water spray active) are controlled by the PLC and can be adjusted in the visualization. Over-applied water is collected by gutters situated all around the carriage table and is then piped to a collecting tank.
- Wheel lubrication: a lubricant can be applied through a SBB (Switzerland Federal Railways) locomotive grease spray nozzle directly to the wheel flange. The nozzle is adjustable concerning spray direction. The spray amount and application interval are adjustable parameters in the control system.
- Friction modifier: Kelsan Technologies (now LB Foster Friction Management, Canadian company, inventor of a friction modifier for top of rail) developed a special adapted friction modifier application device (Figure 6.2). It consists of a friction modifier storage tank with ultrasonic level sensor, a fluid pump, a spray nozzle, a heater with subsequent air blade and a separate control unit that is connected with the PLC. The spray nozzle produces an atomized friction modifier spray by mixing the friction modifier fluid with compressed air. The nozzle is adjustable in vertical and lateral directions and also the spray angle can be adjusted. The air blade is used for drying the friction modifier once applied to the rail surface. The amount of friction modifier which is pumped through the nozzle feeder hose can be manually adjusted with a gauge. Spray interval and spray duration are controlled by the PLC. The spray can be directed to the whole rail head or only to parts of the head (TOR only, gauge corner only) by shielding devices.

The test rig can simulate uni-directional or bi-directional traffic conditions. For bi-directional running the wheel stays loaded all the time while the rail carriage moves back and forth. It

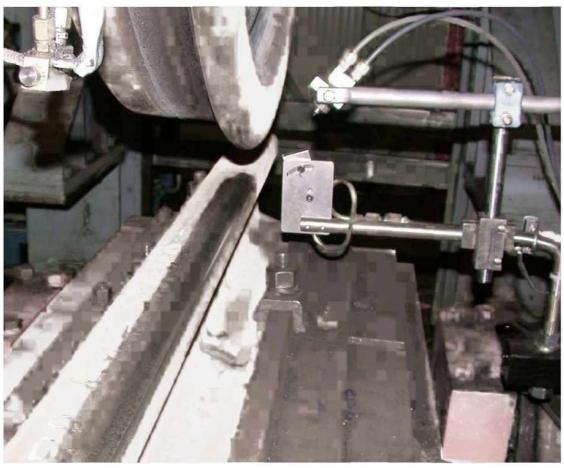

Figure 6.2.: Parts of the friction modifier application device: spray nozzle (with hoses for compressed air and liquid FM) and heater air blade.

is necessary to move the wheel once a day for about 1/3 of the circumference in order to provide uniform circumferential wheel wear. For uni-directional running the wheel is lifted up while the rail carriage is returning at the end of a pass, and then gently set down on the rail to start another rolling cycle. The speed of the test rig is limited to 1m/s, allowing a maximum of 33,000 wheel passes in a 24 hour period in uni-directional running mode and approx 40,000 cycles per hour in bi-directional running mode. The loaded contact length on the rail is divided into three parts:

1. The first 0.2 m in which the hydraulic system is powering up and accelerating the rail carriage.
2. The rail test area (0.5 m) with stable load and speed conditions. All rail examinations were done on this section.
3. Carriage stopping distance (0.2 m).

A typical load cycle for uni-directional operation mode would consist of the whole movement part when the wheel stays in contact with the rail but also includes the whole back-stroke, when the wheel is lifted up until it lifts down again on the rail. Forces are measured within the hydraulic cylinders. Rail and wheel positions are recorded in all three dimensions with displacement sensors. Room temperature and air humidity are recorded during each test. All measured data are stored in a database for post processing and test evaluation. The test room is air conditioned that allows to keep a constant room temperature. Nevertheless the air humidity in the room changes with the outside air humidity. In winter there is also a heater in the room to keep the temperature above the freezing point while the test rig is not operational.

7. Test procedures

7.1. Previous work

The tests described in the diploma thesis [58] produced only on one rail three Head Check-like cracks at the gauge corner - see figure 7.1. Quite some time was spent by the author to find test rig settings that provided repeatable generation of multiple Head Checks within 100,000 loading cycles. These pre-tests will not be further described in this thesis; nevertheless some of these tests can be found in the report of the EU funded project Railconfat [60].

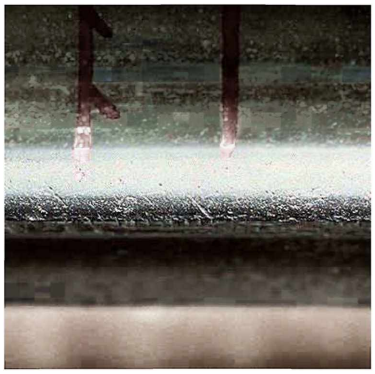

Figure 7.1.: 3 Head Check-like cracks on the gauge corner of a rail produced during a test in 1999. [58]

7.2. General Parameters

Table 7.1 lists the general parameters that were kept constant for every test, started always with a new rail in as-produced condition and a new or re-profiled wheel. After the installation of wheel and rail the alignment of both was checked to make sure there is no unwanted angle of attack between wheel and rail. The surfaces of wheel and rail were cleaned with a cleaning fluid in order to have no grease on the rail that would cause a test to be not usable. Also a test form was filled for every test that contained the preset test parameters and was also used to record important observations during a test.

7.3. Specific Parameters for friction modifier tests

For the test series with the friction modifier the following additional parameters were preset:

- Friction modifier application interval: every 250 cycles.

Parameter	Description
Wheel Type	OBB R7 freight car wheel with UIC ORE 1002 wheel profile
Traffic	uni-directional
Test length	100,000 cycles (except for special tests)
Vertical Load	23t
Lateral Load	4t
Angle of Attack	0° (lateral contact forced by lateral load)
Rail cant	0
Rail profile	60E1 (former UIC60)
Room temperature	approx. 25°C

Table 7.1.: General test parameters.

- Direction of the friction modifier spray nozzle: full contact coverage (top of rail and gauge corner).
- Application amount: approx. 0.25ml per spray cycle.
- Heater cycles: 1.

A typical friction modifier application cycle consists of the following steps:

1. Activation of the heater air blade system 10 cycles before application in order to provide a hot air stream.
2. Stop of the rig at the wheel set down position and complete lift-up of the wheel (limited by hydraulic cylinder stroke).
3. Activation of the friction modifier pump and compressed air.
4. 0.5 s wait time before the carriage starts to move at normal speed while spray is still active.
5. Deactivation of the pump and compressed air as soon as the carriage reaches the end position.
6. Slow speed backwards move of the carriage to provide sufficient dry time.
7. As soon as the carriage reaches the wheel lift down position, the heater air blade is deactivated and the wheel lifts down again to continue with normal load cycles.

8. Examination methodology

8.1. Photo documentation

Surface photo documentation was done at least at the end of every test. Only the more recent tests have photo documentation done at the MiniProf wear measurement intervals (see below). Multiple brands of digital still cameras were used: Nikon Coolpix 5700 and 8700, Sony DSC F505 and Nikon D40x.

8.2. Wear measurements and calculations

8.2.1. Measurements

Wear measurements were done using a Greenwood MiniProf device (for more information see http://www.greenwood.dk). This instrument is capable of measuring transverse profiles of rails. The software MiniProf for Windows Version 2.3.x and 2.4.x was used for the measurements and subsequent analysis. Three measurement points (R1, R2 and R3) were marked on the test rails. The first point was located in the center of the rail. The other two were marked on the rail in rolling direction 10cm and 20cm away from the first point. Wheel measurements were done at two opposing measurement points (WH1 and WH2) with a specially developed MiniProf adapter that allows the usage of a MiniProf rail device for wheel measurements. All the wear measurement were done at predefined intervals: after 0, 2000, 5000, 10000, 20000, 50000, 75000 and 100000 cycles.

8.2.2. Standard Rail Wear Calculations

As a first step the profiles were aligned using the MiniProf for Windows alignment tools for wheel and rail with reference to a new rail and wheel profile. MiniProf for Windows can calculate the wear parameters W1, W2 and W3 that are defined according to figure 8.1. W2 and W3 can be adjusted by the parameters L and A which is the angle of the tangent attached to the initial rail profile. L is a vertical distance measured from top of rail and was fixed to 12mm. A was varied to 9.9° - 35° - 45° - 70° in order to cover the whole contact region on the rail. The 45° calculation represents a standard calculation for track analysis. The angles 9.9° - 35° - 70° were derived from [58] and represent three main regions within the contact path on the rail surface at the test rig - 9.9°: TOR - low wear, 35°: gauge corner with head checks, 70°: high wear region on the rail side. For all wear calculations the 0 measurement (start of the test) of each measurement point was used as a reference. This method is in this thesis referred to as W-wear calculation and is only applied to rails.

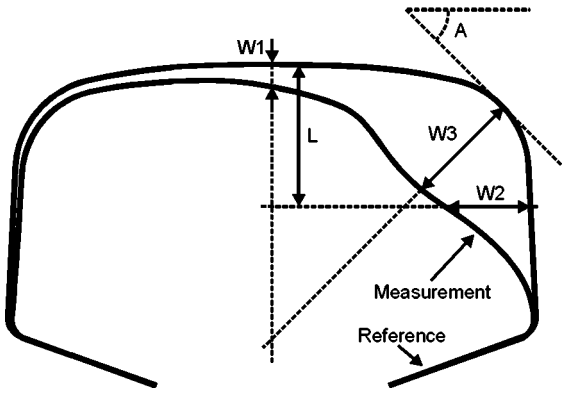

Figure 8.1.: Definition of wear parameters W1, W2 and W3 defined by distance L (12mm) and tangent angle A (9.9°, 35°, 45°and 70°).

dL [mm]	Area Lost [mm^2]	Area Gained [mm^2]	Total Area [mm^2]	Contact length [mm]
0.5	25.292	0.053	25.239	68.25 - 114.75
0.4	25.292	0.038	25.254	68.2 - 114.6
0.3	25.292	0.067	25.225	68.25 - 114.75
0.26	25.292	0.078	25.215	68.25 - 114.79
1.0	25.291	0.004	25.287	68.5-114.5

Table 8.1.: Worn area calculation parametric study, influence of parameter dL (length segment on the rail or wheel profile) on area calculation.

8.2.3. Lost area calculations

MiniProf for Windows provides the functionality of lost area calculations for wheel and rail measurements. The preset parameter dL represents a length segment on the wheel or rail profile that is used for the calculation (see figure 8.2). Using a length element as short as, or in the same length range as the average point spacing (the MiniProf device records the profile as a number of x-y coordinate points) results in failing of the calculation algorithm and causing complete data scatter. Using dL at least 0.02mm longer than the average point spacing provides useful data. A parametric study was done using the files R1_0 and R1_100000 from R260 dry#1 test. The average data point spacing was for R1_0: 0,257 and for R1_100000: 0,256. The results are shown in table 8.1.

The results show that the accuracy of the calculation is not directly influenced by the width of the step dL as long as the area is completely enclosed by the upper and lower boundaries of the contact length. If there are only parts of areas within the contact length, the accuracy is influenced by the length of dL and the relationship of dL to the average data point spacing of the profiles. For all examinations dL was set to 0.5mm to have high enough accuracy concerning contact length but also avoid too much data scatter in calculation caused by the calculation algorithm.

All the area calculations were exported to .mpr files using the MiniProf software. The area results files contain the position on the profile [mm] in 0.5mm steps starting on the left side of the profile, the corresponding "area gained" value in [mm^2] and the corresponding "area lost" value in [mm^2]. Microsoft Excel 2007 and 2010 was used to make further calculations

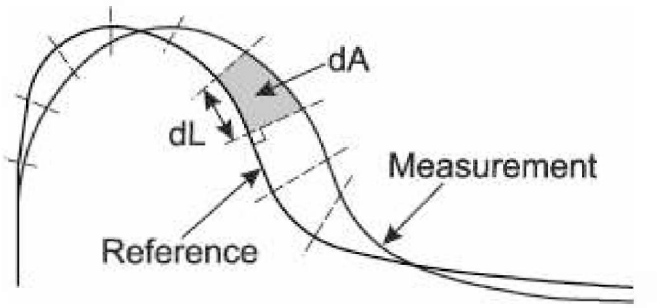

Figure 8.2.: Parameter definition (dL: length segment on profile and dA: area segment between new and worn profile) for area calculation according to the software MiniProf for Windows V 2.4.x.

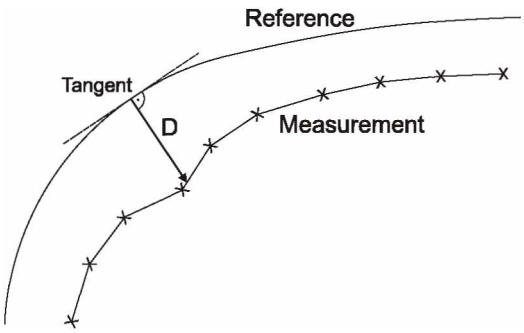

Figure 8.3.: Definition of residual calculation. Normal distance (perpendicular to tangent on reference profile) between reference and measured profile.

with these files - see below.

8.2.4. Residuals calculation

The residuals are defined according to figure 8.3 as the normal distance between the two profiles. MiniProf for Windows was also used to calculate residuals for wheel and rail profiles. The exported result files contain the tangent angle, the center angle and the residual distance D [mm] and the position on the profile [mm] starting on the left side of the profile (as displayed on screen). Microsoft Excel 2007 and 2010 was used to make further calculations with these files - see below.

8.2.5. Calculation of contact width and area loss

A special MS Excel 2007 macro was programmed in order to determine the contact width and the area-loss of each measurement. The macro first converts the .mpr files to .xlsx files. After that the contact width is determined using the "residuals" files. In order to reduce calculation time possible contact positions are reduced to the right half of the rail and to a region between wheel flange top and wheel tread center. The criterion for "contact" was

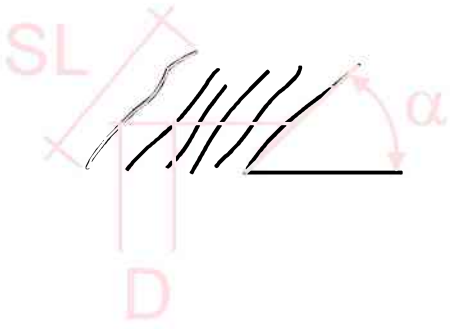

Figure 8.4.: Head check surface characterization parameters.

set to D $\geq$ 0.1mm as the accuracy of the measurement in combination with the accuracy of the alignment of the profiles was found to be 0.1mm or better (concerning "D"). The so determined positions of upper and lower contact end were used in combination with the "area files" to determine the corresponding area loss of wheel and rail.

8.2.6. Normalized wear calculation

In order to overcome slight differences in test rig set-up, a normalized wear calculation for rails was developed. This calculation only considers the wear rates between 50,000 and 100,000 cycles where a steady wear rate for every test was established. The normalized wear is defined by dividing the area loss value [mm^2] by the contact width [mm]. The resultant is a normalized wear rate in [mm].

8.3. Magnetic Particle Images (MPI)

Magnetic particle imaging was used at the end of each test to visualize the surface cracks. While magnetizing the rail with a hand electromagnet a magnetic, UV fluorescent powder (type Ferromor NDF Fluorescent Powder, ELY Chemical Co Ltd) was applied to the rail. The rail surface was then photographed with an attached scale under UV light conditions. For the most recent tests (R350LHT, R370CrHT) a MPI spray (type Diffu-Therm MPS-F) was used instead of the powder resulting in a better resolution of the cracks. The image analysis software ImageJ 1.44p (http://imagej.nih.gov/ij/ - Image processing and analysis in Java) was used to determine surface crack length *SL*, angle α and crack distance *D* (see figure 8.4). The listed values represent averaged values over a certain rail sample length. For the parameter *SL* the "segmented line tool" of the software was used to redraw the cracks. The crack distance *D* was measured in the middle of the crack band.

A detailed crack pattern examination was done using a representative 2cm long MPI sample for each rail grade. With this sample the crack-pattern was redrawn as accurately as possible. Again a crack length and crack distance examination was conducted as described above. Three examination lines were chosen for that examination: line 2 in the middle of the crack band, line 1 in the middle of the upper half and line three in the middle of the lower half of the crack band (see figure 8.5).

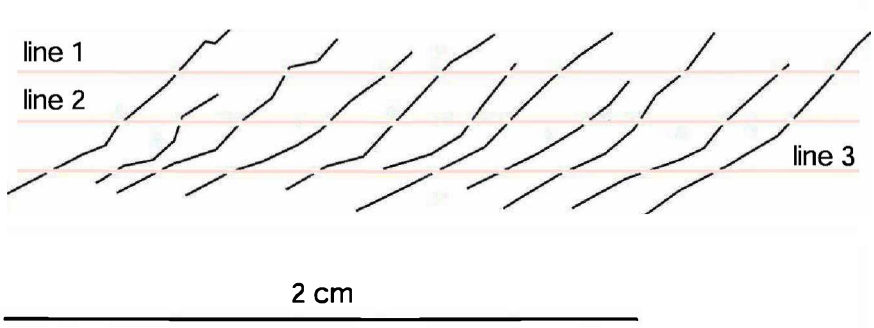

Figure 8.5.: Detailed crack examination on a 2cm MPI sample (R260) using 3 analysis lines.

8.4. Metallographic examinations

Rail sections were cut out of the rail between positions R2 and R3. First a surface analysis was done according to [58] to determine the position N on the rail surface where only deformation in lateral direction occurred - neutral line with no longitudinal creep and pure rolling. After that a transverse micrograph was taken at this position N and also at the position of head checks if any were present. Finally in the case of visible head checks, a longitudinal section was taken according to the ERRI procedure [61] in order to determine the depth of the cracks. All the metallographic work was done by the metallographic workshop at voestalpine Schienen GmbH.

8.5. Creepage Calculation

A creepage was calculated using the Carter's equation from [62].

$$S = \left(\frac{2 \cdot (v_t - v_u)}{v_t + v_u} \right) \cdot 100\%, \tag{8.1}$$

where v_t represents the the train speed and v_u represents the circumferential speed of the wheel for a given radius. As in this thesis creepage in reference to different wheel-radii in the contact zone was calculated, the equation was transformed to:

$$S = \left(\frac{2 \cdot (r_N - r_u)}{r_N + r_u} \right) \cdot 100\%. \tag{8.2}$$

In this transformed equation the parameter r_N represents the wheel radius at the position *N* on the rail where the circumferential speed of the wheel equals the speed of the rail (no longitudinal creepage - position of pure rolling). The parameter r_u represents a wheel radius of concern. This equation was used then to determine the creepage at certain positions on the rail profile relative to the position *N* on the rail at the end of selected tests. These positions are listed in figure 8.6.

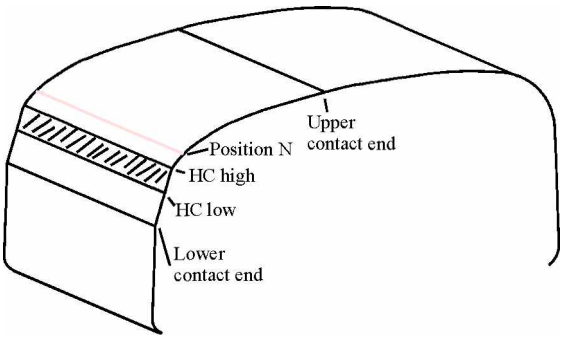

Figure 8.6.: Creepage calculation positions at the end of a test. Neutral position N: only lateral creep is acting on the rail surface. HC high/low: upper and lower end of the Head Check (HC) band.

8.6. Plastic Flow examination

In order to determine the depth of plastic flow the metallographic images taken at position *N* (no longitudinal creepage) were used. The software ImageJ V1.44p was used to make these examinations.

8.6.1. Procedure A

After setting the scale of the image the surface of the image was enhanced by redrawing the surface with a segmented line of the thickness of 6 and color white. The line was included in the picture by applying the command "Measure and label". After this step a threshold function was applied to the image using the RenyiEntropy "Thresholding method"[63] with the "Threshold color" setting B/W (Black and White). The "Color space" was either chosen RGB or HSB depending on the contrast conditions of the pictures. The upper and lower limits were set to auto and the option "Dark background" was activated. After that step the plug-in "3D interactive surface plot" was applied to the image with the parameters:

- Lines.
- Thermal LUT.
- Grid Size: 512.
- Smoothing: 6.
- Perspective: 0.2.
- Scale: 1,84.
- z-Scale: 1.0.
- Max: 100%.
- Min: 0%.

The perspective was chosen that the resulting picture represented a 2D surface plot of the x and y coordinates (projection perpendicular to the x-y plane in z direction). In this visually

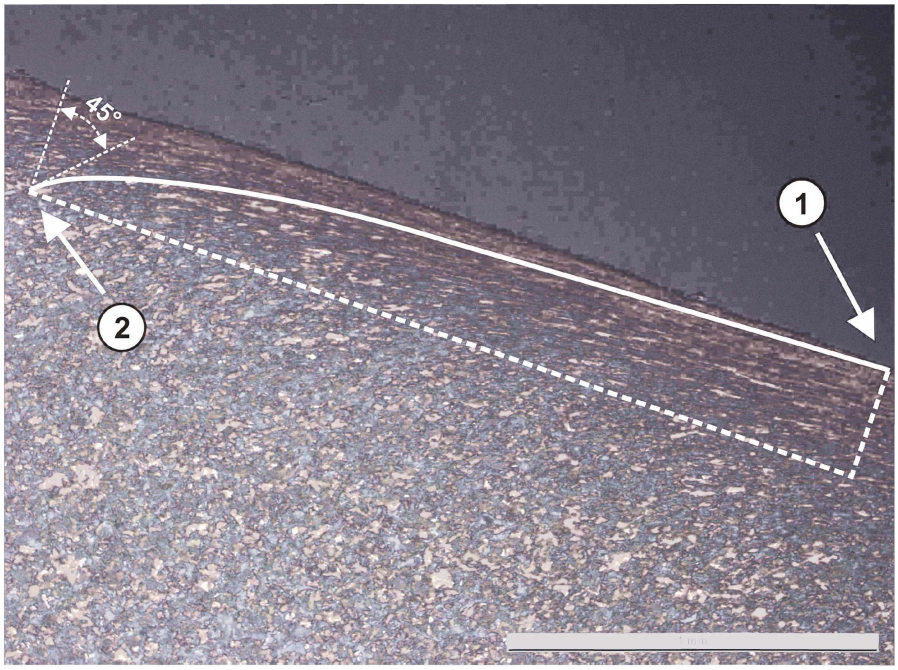

Figure 8.7.: Determination of depth and extension of plastic flow according to procedure B. Starting on the rail surface ① and following the deformation until an angle of 45° is reached ②. This examination was conducted by Kelsan personnel.

enhanced picture the the depth of plastic deformation was measured perpendicular to the surface using the ImageJ measuring utilities.

8.6.2. Procedure B

For the test series in connections with the FM another procedure was initially chosen to compare surface and subsurface plastic flow procedure. Pictures of transverse micrographs were taken and a line was drawn by hand following the deformed microstructure from a starting point on the surface (① - figure 8.7) until it reached an angle of 45° (② - figure 8.7). Between these two points the lateral and depth distances of plastic flow were determined. This examination was conducted by Kelsan personnel and not by the author of this thesis. This examination was conducted at wear measurements points 9.9° (which refers to the TOR region) and 35° (which refers to the HC area).

Part III.

Experimental work

9. Rail grades

9.1. Pearlitic rail grades

One "as-cooled" grade and 4 heat treated rail grades from the production of voestalpine Schienen GmbH with pearlitic micro-structure were used for the test rig tests. An overview of the general parameters of these rail grades can be seen in table 9.1. The main difference between these tested rail grades consists in hardness and tensile strength which are a result of the lamella distance of the pearlitic micro-structure. The lamella distance is influenced by the heat treatment process and slight differences in chemical composition. The grades R370CrHT and R400HT also do have a voestalpine brand name, as they were developed long before they were registered in the EN 13674-1:2011 [54] specification. The R370CrHT corresponds to the brand name 370LHT HSH® and the R400HT corresponds to the name 400UHC HSH®. Also the R350HT and R350LHT rail grade has now the brand name R350HT HSH® respectively R350LHT HSH®(HSH stands for Head Special Hardened).

	Chemical Composition						Mechanical Data		
grade	C	Si	Mn	P_{max}	S	Cr	R_m [MPa] min	A_5, [%] min	Hardness [HB]
R260	0.62-0.80	0.15-0.58	0.70-1.20	0.025	0.08-0.025		880	10	260-300
R350HT	0.72-0.80	0.15-0.58	0.70-1.20	0.020	0.08-0.025		1175	9	350-390
R350LHT	0.72-0.80	0.15-0.58	0.70-1.20	0.020	0.08-0.025	<0.3	1175	9	350-390
R370CrHT	0.68-0.84	0.38-1.02	0.65-1.15	0.025	0.025	0.35-0.65	1280	9	370-410
R400HT	0.88-1.02	0.18-0.42	1.15-1.35	0.025	0.0258	<0.3	1280	9	400-440

Table 9.1.: Tested steel grades according to EN 13674-1:2011.

9.2. Bainitic rail grades

In this examination two different types of rails with bainitic structure were used. The B430 grade represents the second generation Bainitic rail grade development of voestalpine. This rail grade has a lower bainitic structure which is achieved by quasi-isothermal heat treatment. The TB1400 was a development by Thyssen Schienen Technik which was acquired by voestalpine in 2001. The TB 1400 represents a carbide free bainite. The rail is not heat-treated during the production process and is cooled to room temperature on a cooling bed. In order to achieve the desired micro-structure with air-cooling it is necessary to add a number of alloying elements. The chemical composition and general mechanical parameters are listed in table 9.2.

	Chemical Composition						Mechanical Data		
grade	C	Si	V	Mo	Ni	Cr	R_m [MPa] min	A_5, [%] min	Hardness [HB]
B430	0.80		0.15	0.15	0.20	0.50	1400	>9	>430
TB1400	0.40	1.10	0.10	0.70		1.10	1400	>9	>400

Table 9.2.: Tested bainitic steel grades according to internal voestalpine specification.

10. Wheel grade

The European standard EN 13262:2004 [64] defines the properties of railway wheels. According to [65] railway wheels are forged or cast. The rim of the wheels is typically heat treated to improve wear resistance and to increase crack resistance due to compressive residual stresses. This heat-treatment is typically done as total quenching (E) or rim chilling (T). The standard grade in Europe is ER7T because of its mechanical properties (hardness and toughness). Table 10.1 lists the chemical composition and table 10.2 lists general mechanical properties of the ER7 wheel used for the test rig tests.

Chemical Compositions										
C	Si	Mn	P	S	Cr	Cu	Mo	Ni	V	Cr + Mo + Ni
0.52	0.40	0.80	0.020	0.015	0.30	0.30	0.08	0.30	0.06	0.5

Table 10.1.: Chemical composition of test rig wheel grade ER7 according to EN13262:2004.

Mechanical Data			
R_{eh} [N/mm^2]	R_m [N/mm^2]	A5 [%]	Hardness [HB]
≥520	820 / 940	≥14	235

Table 10.2.: Mechanical data of test rig wheel grad ER7 according to EN13262:2004.

11. Test Overview

11.1. Dry Tests

11.1.1. R260

A number of 17 pre-tests (as part of voestalpine internal research) were done in order to assure repeatable head check generation within 100,000 load cycles. These tests will not be part of this thesis.

Altogether 2 tests were done with R260 grade under dry contact conditions that were used for the examinations in this thesis:

- Kelsan Test #1 (R260 dry #1).
- Kelsan Test #14 (R260 dry #2).

These tests were part of the FM test series but as they were done under dry conditions they were also used for the dry test series. As the test nomenclature changed over time, the tests are renamed in this thesis according to the actual test rig nomenclature - names in brackets. The test R260 dry #1 was started with a slightly used wheel profile. If results are generally addressed as R260 dry then they represent the averaged values of these two tests. Otherwise the results are labeled with the name of the according test.

11.1.2. R350HT

Altogether three tests were done with the grade R350HT and dry contact conditions:

- R350HT dry #1.
- R350HT dry #2.
- R350HT dry #3.

The wheel of test R350HT dry#1 was used also for test R350HT dry#2 - this test represents results with a used wheel. If results are generally addressed as R350HT dry then they represent the averaged values of these three tests. Otherwise the results are labeled with the name of the according test.

11.1.3. R400HT

Only one test was done with this grade: 400UHC dry#1 (R400HT dry #1). As repeatability of the tests was already proven for R260 and R350HT tests, no repeat test was done for R400HT.

11.1.4. TB1400

Two tests were done with this grade in two different conditions:

- TB1400 nA dry#1 (CF-B nA dry #1): this rail was in the as-rolled condition,
- TB1400 A dry#1 (CF-B a dry #1): this rail was tempered at 550°C for 1h in a laboratory furnace.

The post production process of tempering is necessary because of residual stresses, especially in the foot of the rail that could cause accelerated crack growth and rail failure. Furthermore, the as-rolled structure contains a low amount of martensitic structures that will also be transformed during the tempering process. The hardness of the rail is not changed due to that tempering process.

11.1.5. B430

One test was done with this rail grade: B430 UB dry#1 (LB dry #1). This rail grade was in track for some track tests and was later replaced by the newly developed 3rd generation bainitic rail grade as it did not show the expected RCF resistance.

11.1.6. R350LHT and R370LHT

The conditions of these tests are different compared to the conditions of the other tests as a necessary test rig repair had to be done in 2009. The "eye" of the vertical hydraulic cylinder (where the cylinder is connected with the wheel beam) was defective and had to be replaced. Due to this repair the clearance between the cylinder eye and wheel beam was drastically reduced resulting in totally different contact conditions. As the whole lift up and lift down cycle was not position-controlled but time-controlled, a change in clearance resulted in different lift up ways resulting in different initial contact conditions after lift down. Several attempts were made to change the timings of vertical and lateral lift up but these attempts did not succeed in reproducing the initial contact conditions. After having found a set of timings that produced repeatable head check generation within 100,000 cycles this set-up was used for all subsequent tests. For both rail grades one usable test each was conducted with this set-up:

- R350LHT dry#2 (R350LHT dry#1).
- R370LHT dry#3 (R370LHT dry #1).

11.2. Tests with the Friction Modifier (FM)

11.2.1. Pretests

In order to determine the right application rate of the friction modifier a series of pretests was done. According to [20] a typical application amount would be 225ml of friction modifier per km of rail in curve. Converting this number to the test rig conditions means that an amount of approx. 0.225ml should be applied per application-cycle at the test rig . A gravimetric method was chosen to select the right pump settings: the spray nozzle was dismounted from

the test rig and 10 application cycles were done directing the spray nozzle to a small plastic bowl which was previously weighed. After these 10 applications into the bowl the weight of the bowl containing the wet friction modifier was determined again. With the density of the friction modifier the amount applied per spray cycle was determined. Once the right pump settings were found this test was repeated in regular intervals for verification purposes or after longer time periods, during which the friction modifier application device was not used. The angle of the spray nozzle was adjusted so that the whole expected contact area was covered with the friction modifier. This was controlled before each test by attaching an adhesive paper tape onto the rail head over the whole rail length. If the coverage after several spray passes was obviously unbalanced, the angle of the spray nozzle was corrected.

After having set all these parameters three specific tests (standard test conditions) were done with only the number of wheel cycles between the applications varied:

- FM500 - friction modifier application every 500 cycles, rail grade R260,
- FM250 - friction modifier application every 250cycles, rail grade R260.
- FM50 - friction modifier application every 50 cycles, rail grade R260.

Two aspects of these test rails were analyzed: appearance of head checks and rail wear at the 35° angle. These three tests were then compared to the R260 dry#1 test results - see figure 11.1. The test with FM500 shows some reduced wear compared to the dry test but nevertheless some head checks formed on the rail. It was also found that these head checks did not form as regular as under dry contact conditions, resulting in a reduced "head checks per cm" value. Both tests, FM250 and FM50, developed no head checks on the rail surface and also their wear results were on the same level. The slight difference in wear results can be explained by the inaccuracy of the measurement / calculation method especially in low wear regime. Due to these results the application interval of FM250 was chosen to be the standard condition.

11.2.2. Tests with friction modifier (FM) application

Due to the experience with the pretests only one test with R260 and friction modifier application was done: Kelsan Test 5 (R260 FM250 #1). For the grade R350HT two tests were done: R350HT FM250 #1 and R350HT FM250 #2. If results are generally addressed as R350HT FM250, then they represent the averaged values of these two individual tests. Otherwise the results are labeled with the name of the according test. In order to examine the long term behavior two tests with 400,000 cycles each were done: R260 LT FM250 #4 and R350HT LT FM250 #1. Due to some unexpected problems (contaminated wheel, hydraulic leak, mechanical defect) at the test rig three LT tests with R260 failed completely and could not be used. Also during the R350HT FM250 #1 test a mechanical defect occurred at the test rig that interrupted the test. After restarting the test the rail R350HT FM250 #2 was accidentally installed and the LT test was continued with this rail and this test did not reach the full 400,000 cycles.

11.2.3. Friction modifier (FM) and pre-existing cracks

A special test series was done to examine the effect of a dry friction modifier on pre-existing cracks on a rail. Experience from Kelsan showed that the wet friction modifier can cause

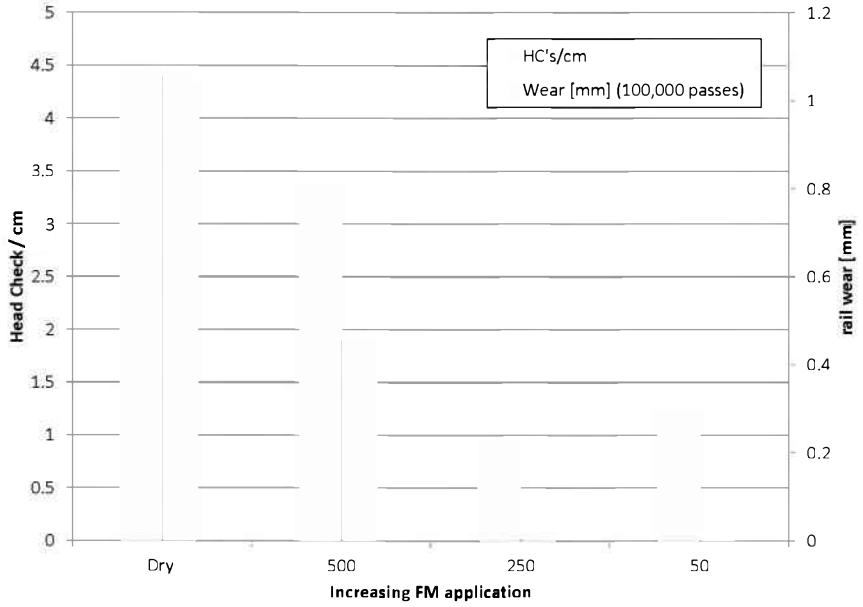

Figure 11.1.: Comparison of tests with different friction modifier (FM) application intervals with dry contact conditions. The FM250 condition was chosen to be the standard condition as it did not develop any Head Checks.

accelerated crack growth if cracks are present on the rail surface[66]. However, it is unclear if the dry friction modifier can also cause accelerated crack growth by reducing the friction between the crack flanks [67].The test setup consisted of two phases: a 25,000 cycles dry phase in order to form cracks on the rail head and a subsequent 75,000 cycles FM250 phase. Three tests with two rail grades were done in this context:

- R260 dry-FM #1 - due to some more technical problems at the test rig this test was extended to 200,000 cycles. During the first 100,000 cycles no cracks formed on the rail. For time restriction reasons this test was not restarted after fixing the problem at the rig but was continued and after 125,000 cycles cracks were present on the rail surface. The friction modifier device was then turned on (FM250) for the 75,000 subsequent cycles.
- R350HT dry-FM #1 - no problems during this test.
- R350HT 25k dry #1 - for having a direct comparison to the R350HT dry-FM #1 test the wheel of this test (which was not very worn) was used to make a 25,000 cycles dry test.

Part IV.

Results and Discussion

12. Wear

12.1. Dry Contact Conditions

12.1.1. Normal test conditions

For every test the wear calculations were averaged over the measurement points (R1, R2 and R3 on the rail and WH1 and WH2 on the wheel). Figure 12.1 indicates that wear was not constant over the length of a rail. For both R260 dry tests there is a noticeable increase of rail wear from point R1 to point R3. This increase is a consequence of the hydraulic control system and could not be solved during the course of the tests in this thesis as a major renewal program would have been necessary. Due to this fact the rail wear calculations are always averaged over the measurement points. A difference can also be noticed in the resulting rail wear values after 100,000 cycles for the two R260 dry tests. This can be explained by the fact that R260 dry#1 started with a pre-worn wheel and R260 dry#2 started with a new wheel. The pre-worn wheel resulted in an initially already more conformal contact compared to the new wheel and thereby reduced the absolute rail wear during the test.

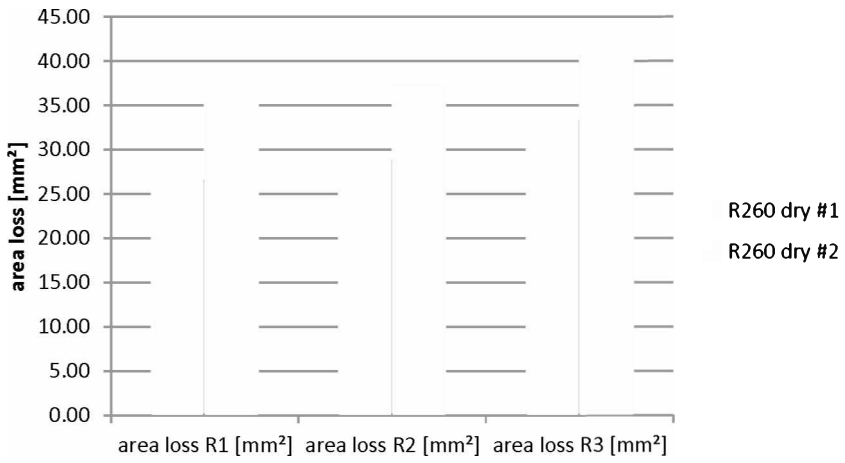

Figure 12.1.: Area loss values after 100k cycles for R260 tests. Values shown for all rail measurement points R1, R2 and R3. R260 dry #1 started with a more conformal contact due to a pre-worn wheel resulting in less rail wear due to the reduced contact pressure.

Figure 12.2 shows the W-wear (see figure 8.1 on page 49) calculations for both tests highlighting the difference even more clearly and thereby shows the effect of an initially more conformal contact. At calculation position W1 there was no contact resulting in no rail wear at all. Negative wear can be explained by plastic flow of the rail material due to the high contact loads. Besides a trend that all of the calculated rail wear values show lower results

for R260 dry #1, the calculation positions that are orientated towards the top of rail (9.9°, 35° and 45°) especially show considerably lower values compared to the corresponding W2 and 70° values for that test. For R260 dry #2, however, all the rail wear calculations except for the 9.9° position are located quite close to each other. Furthermore, during the first approx 25,000 cycles the rail wear rates are very high. This is explained by a wearing-in phase when rail and wheel profiles conform to each other. After a certain degree of conformality between wheel and rail is reached, the rail wear rates stay constant for the rest of the test at a considerably lower value compared to these first 25,000 cycles. This represents a specific effect of the test rig, as always the same wheel is in contact with the same piece of rail in exactly the same position for every load cycle.

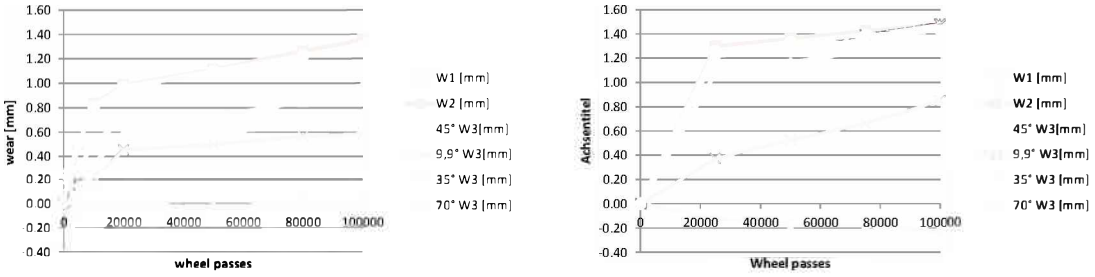

Figure 12.2.: Comparing the W-wear results (W1, W2 and W3 at different tangent angles) of R260 dry tests over whole test length. Left: R260 dry #1, right: R260 dry #2. Lower rail wear of R260 dry#1 due to initially conformal contact due to a pre-worn wheel.

A similar trend can be seen for the R350HT dry tests. Figure 12.3 compares the W-wear results for all three tests. R350HT dry#2 represents the test with a pre-worn profile (wheel from R350HT dry #1). Again the effect of the more conformal contact can be seen as described at R260 dry results though this effect is not as pronounced as with R260 due to the higher wear resistance of R350HT rail grade.

When analyzing the test R400HT dry #1 (figure 12.4) it can be clearly seen that due to the high wear resistance of this rail grade the W-wear calculations do not produce applicable results. For that reason another calculation method was chosen - the area loss calculation that takes the whole worn area into account. The results for all tested pearlitic and bainitic rail grades can be seen in figure 12.5. Comparing first the pearlitic grades, the expected trend that with increased rail hardness the rail wear decreases can be found. The following factors in rail wear resistance can be calculated (reference R260): R260 : R350HT : R400 = 1 : 1.4 : 3.9. Analyzing the bainitic grades it can be seen that the LB grade with a hardness of 430 BHN has a rail wear resistance in the region of the R350HT. This effect can be explained by the microstructure of the lower bainite which consists of a needle like structure of ferrite and cementite. The pearlite on the other hand forms the typical lamella orientation of ferrite and cementite. Due to that composite structure the cementite can add more of its high wear resistance properties to a pearlitic material compared to a LB material [68]. The CF-B structure differs totally from the pearlitic structure [56]. The CF-B nA shows a rail wear resistance in the region of a R260 grade. In the tempered version (CF-B A) the rail wear resistance is drastically reduced resulting in 1.5 times higher final rail wear compared to R260. It also seems that for the CF-B grades the wearing-in process is extended up to 50,000 cycles. Also the area loss of the corresponding wheels was calculated. Figure

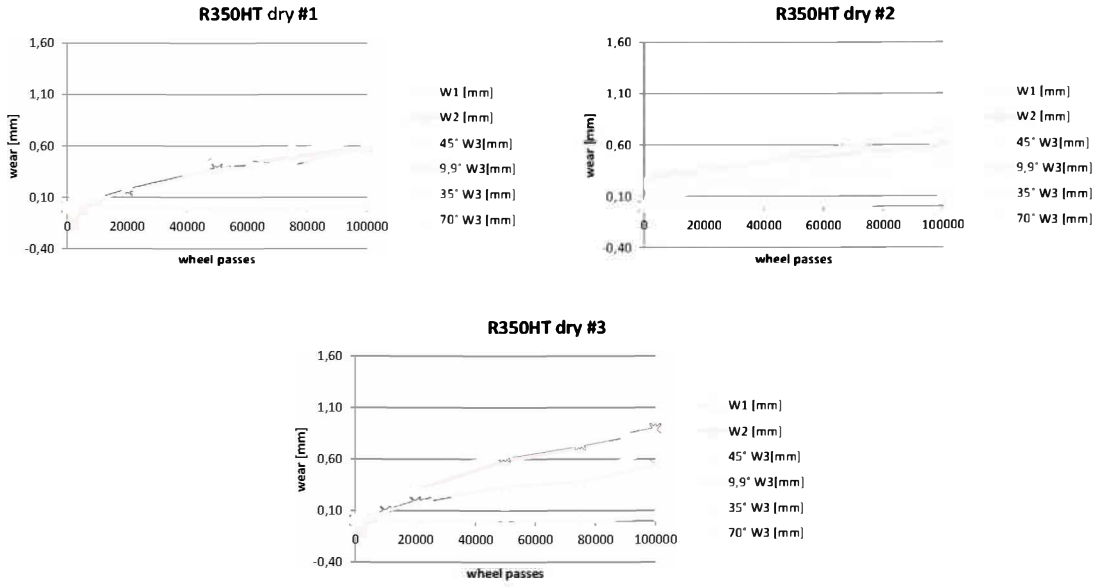

Figure 12.3.: Comparing the W-wear results of all R350HT tests, R350HT dry #2 represents the test with pre-worn wheel profile. Not very distinctive difference between the two tests due to higher wear resistance of R350HT compared to R260.

12.6 shows that the wheel wear results are situated within a very small band of variation. Only the test with the LB rail grade produced slightly higher wheel wear. These address the question of how a variation in rail grades influences the wheel wear if the wheel grade is kept constant and represents the partner with the lowest hardness / wear resistance. This corresponds with the results published by TTCI in [69]. However, the available data does not allow the prediction how rail and wheel wear rates might change by using different wheel grades (higher harness pearlite, bainitic wheel).

When analyzing the rail wear rates after the wear-in in process (50,000 to 100,000 cycles) the wear rates of all grades seem to be on the same level. Differences in wear rates can only be found during the wear-in period. For that reason a more detailed analysis was done considering also the width of the contact band. Figure 12.7 shows the different calculated widths of the contact band. All rail grades except R400HT show similar widths. The difference for the R400HT can be explained either by the higher wear resistance of that grade resulting in a reduced width of the contact band or by the fact that due to the calculation method and high wear resistance the width of the contact band being underestimated (especially in the low wear regions on TOR). Pictures with a an included ruler that would allow an approximate measurement of the width of contact band were only taken for CF-B nA - 48mm width after 100,000 cycles - and R400HT - 40mm width after 100,000 cycles. These results indicate that for the R400HT the width of contact band is underestimated due to the calculation method and also that for the other rail grades an error is made (due to the calculation method) but it can be considered of minor relevance. For some rail grades there is an unusual data scatter during the first 25,000 cycles - this is also a consequence of inaccuracy caused by the measurements and the calculation method under low wear conditions.

For the wheel the situation is different due to the machined surface (machining lines resulting in higher roughness) and the higher inaccuracy of the measurement method due to the wheel

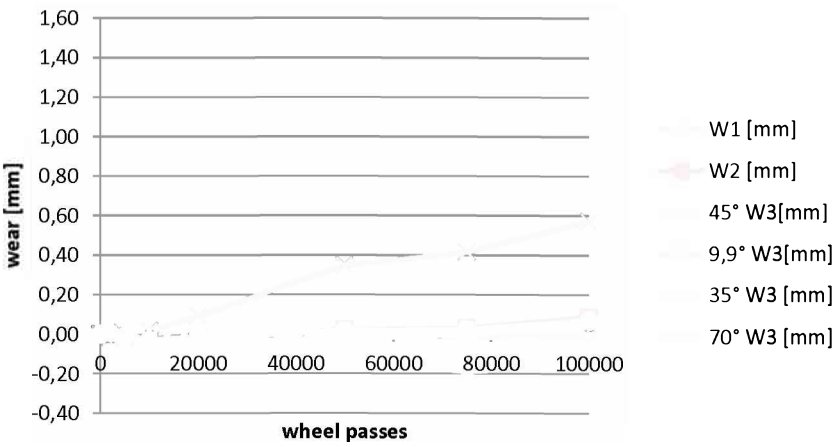

Figure 12.4.: W-wear results of R400HT dry#1; due to high wear resistance of R400HT only 9.9° W3 shows measurable values.

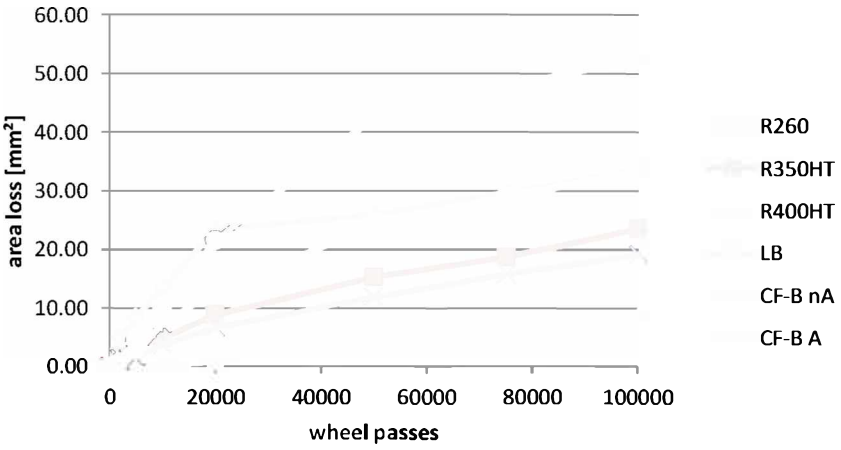

Figure 12.5.: Rail area loss results for all tested pearlitic and bainitic grades with dry contact conditions. Rail grade dependent wear resistance of pearlitic steels. LB is situated close to R350HT, CF-B nA near R260. Only CF-B A shows very high wear rates.

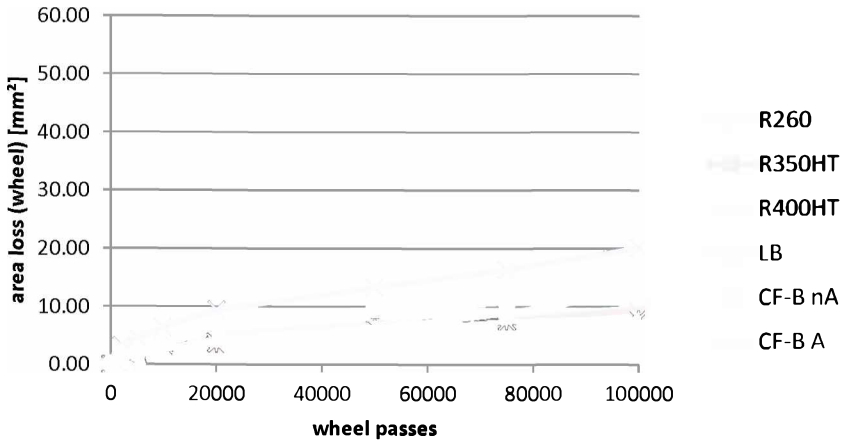

Figure 12.6.: Wheel area loss results for all wheels (R7 grade) vs. pearlitic and bainitic rails (dry contact conditions). All wheel wear results are within a small band of variation. Only the wheel of the LB test shows slightly higher wheel wear values.

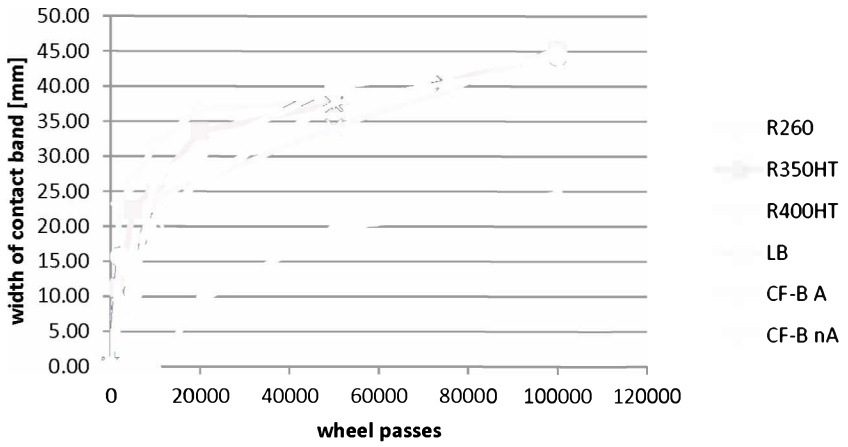

Figure 12.7.: Calculated width of contact band for the tested rails; dry contact conditions; probably underestimation of width of contact band for R400HT due to high wear resistance of this rail grade.

adapter for the MiniProf Rail instrument. According to figure 12.8 the calculated width of contact band on the wheels is lower compared to the calculated width of contact band on the rails. The same explanation provided above (contact width of the rail) can be given: due to the decreased accuracy of the measurements the general data scatter of the measurement superimposes the out-most parts of the contact areas (low wear) resulting in a reduced calculated width of contact band as these areas are considered as "no contact regions" by the algorithm. As a consequence the width of contact band calculation for wheels will not be used for further examinations.

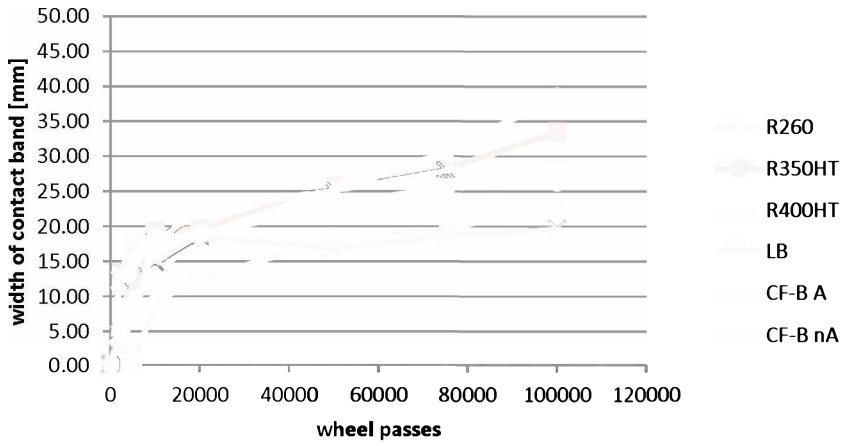

Figure 12.8.: Calculated width of contact band of the wheels; dry contact conditions; scatter of results caused by higher inaccuracy of wheel wear measurement.

In order to calculate a contact condition independent wear parameter the "normalized wear" figure is introduced by dividing "area loss" with "width of contact band" between 50,000 and 100,000 wheel passes. This figure shall help in determining whether the wear rates (inclination of wear over wheel passes curves) for all rail grades really stay at nearly the same level or not. Figure 12.9 shows the result of this calculation and also here the wear rates for all the grades are nearly the same. The final wear at the end of the test is influenced only by the initial wear during the first 25,000 wheel passes. Comparing these results with track test results [70] shows a clear difference (see figure 12.10). Different rail grades result in clearly different wear rates under real track conditions.

12.1.2. Test series with deviating contact conditions

As described in 11.1.6 the contact conditions at the test rig for these two tests were not comparable with the previous tests due to some necessary test rig repairs. For this reason the results are shown separately. Figures 12.11-12.14 show the results concerning wear behavior. Looking at figure 12.11 the wear behavior of both rail grades is almost identical. This could be explained by the fact that according to EN13674-1:2011 [54] the allowed hardness values for these grades provide some overlap - a R350LHT near the upper limit and a R370CrHT at the lower limit might have the same hardness values. This can not, however, be verified any more, as the samples were accidentally destroyed. Compared to figure 12.5 the absolute area loss values are clearly reduced as a result of the differing initial contact conditions. The area

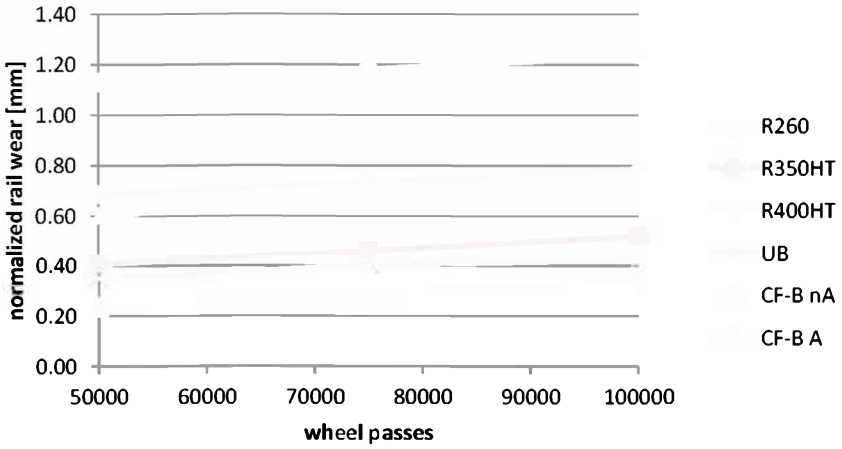

Figure 12.9.: Normalized rail wear calculation (steady state 50k-100k cycles), calculated "area loss" divided by "width of contact band" to overcome differences in rail wear behavior caused by the test rig (initial contact condition). All rail grades show very similar wear rates. Final rail wear at the end of a test only influenced by initial wearing-in process.

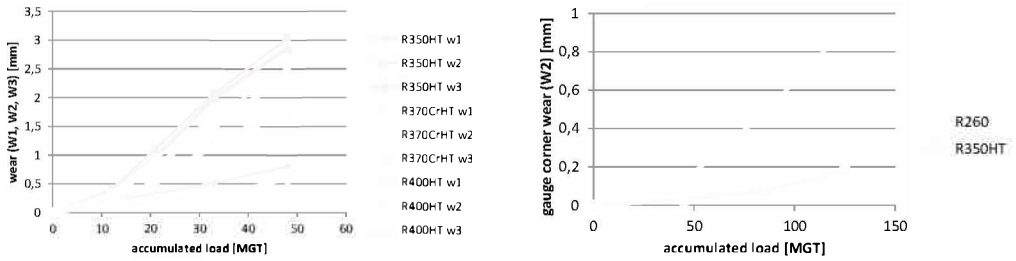

Figure 12.10.: Track test results from the database of voestalpine, partly published in [70], rail grade dependent wear behavior over accumulated load (MGT - million gross tons). A normalized wear calculation as in figure 12.9is not possible due to the lack of necessary input data like the width of contact band.

loss of the wheels is situated in the same region as the tests before (see figure 12.6). The lower values for R350LHT compared to R370CrHT are well within the data scatter range observed for the other tests. Also the contact width results (figure 12.13) show reduced values compared to the other dry tests. As with the worn area also here the R350LHT shows reduced wear data compared to R370CrHT. When calculating the normalized wear (figure 12.14) the results represent what may be expected by the material properties of these two grades and also what may be expected from track test results. The R350LHT displays clearly higher wear results compared to R370CrHT. Also in the context of the other tested grades the normalized wear results of these two tests fit now very well witrh the overall picture (figure 12.15) - the R350LHT is situated close to the R350HT and the R370CrHT is situated close to the R400HT. This is a very good indication that the normalized wear calculation can be used to compare test rig tests with initially different contact conditions.

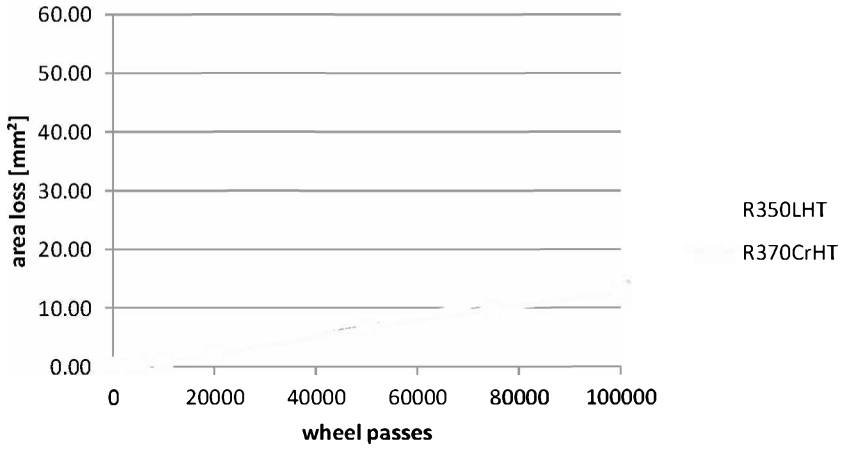

Figure 12.11.: Rail area loss of tests R350LHT and R370CrHT. Similar wear behavior due to very similar initial material properties (surface hardness).

12.2. Friction Modifier contact conditions

12.2.1. Standard friction modifier (FM) conditions

Concerning the wear examinations the test series with the friction modifier focused on the calculation positions W2 9.9° representing the top of rail area, on W2 35° the area with Head Checks and on W2 70° the area with high wear. Figure 12.16 compares the dry results with the friction modifier results for grade R260. After some very low initial wear (the time necessary to get a friction modifier saturation on the rail surface) wear is almost stopped or reduced to a wear rate that is situated below the accuracy of the measurement. Negative wear values can be explained by plastic flow of the rail surface material. For the grade R350HT the results are similar - figure 12.17. Wear is reduced almost to zero due to the friction modifier application. There is no measurable initial wear and also no negative wear was found. This is evidence for the improved resistance against plastic flow of the R350HT compared to the R260 grade. The area loss calculation shows the same trends as the w-calculations. Friction modifier application at the test rig arrests the wear of the rails. Only

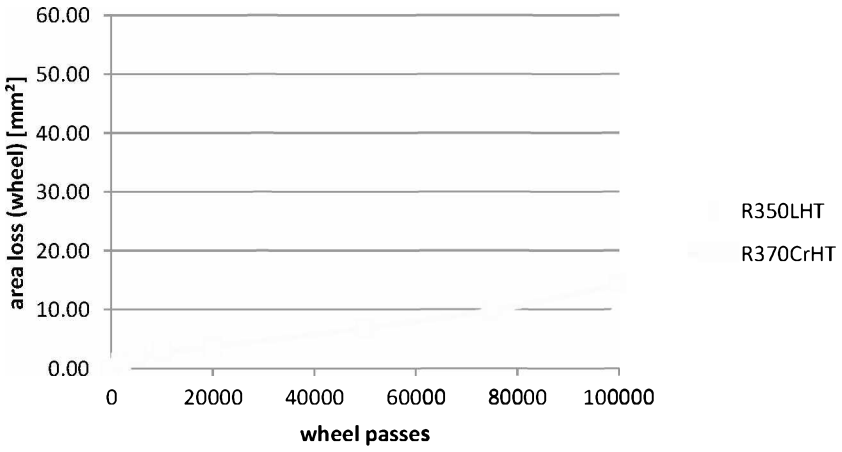

Figure 12.12.: Wheel area loss for tests with R350LHT and R370CrHT, similar wear behavior as shown in figure. Different values can be explained by data scatter caused by the level of accuracy of the measurement. 12.6.

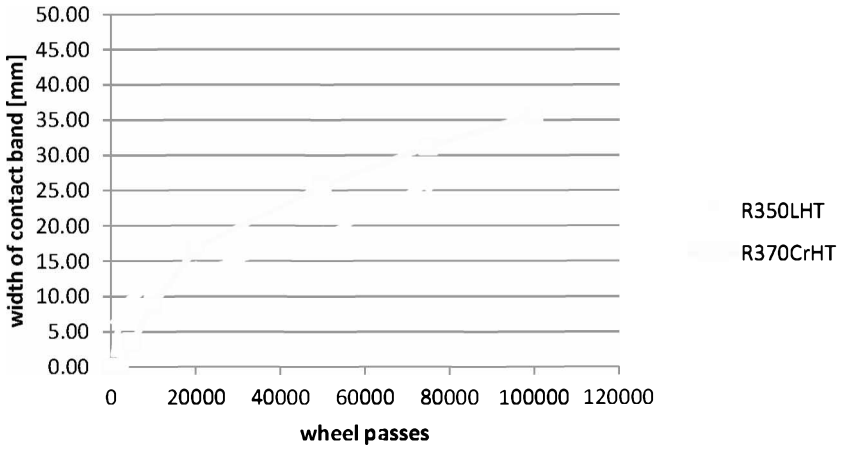

Figure 12.13.: Rail width of contact band calculation for tests R350LHT and R370CrHT.

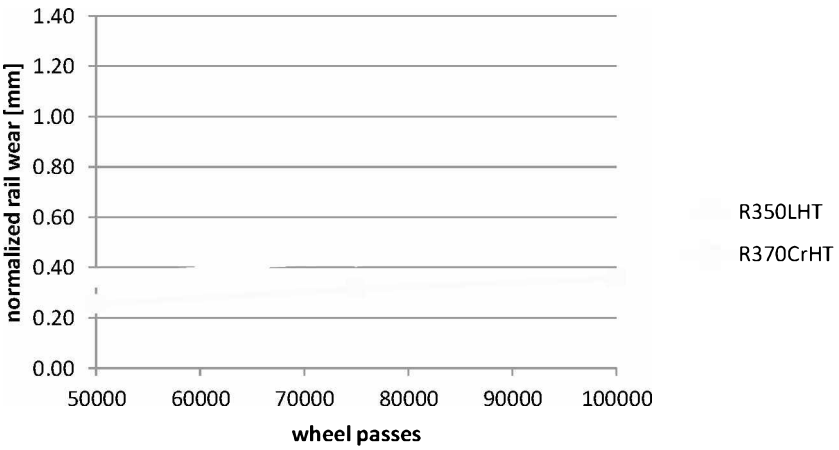

Figure 12.14.: Normalized rail wear calculation for tests R350LHT and R370CrHT; some (expected) difference is visible with the application of the normalized wear calculation method.

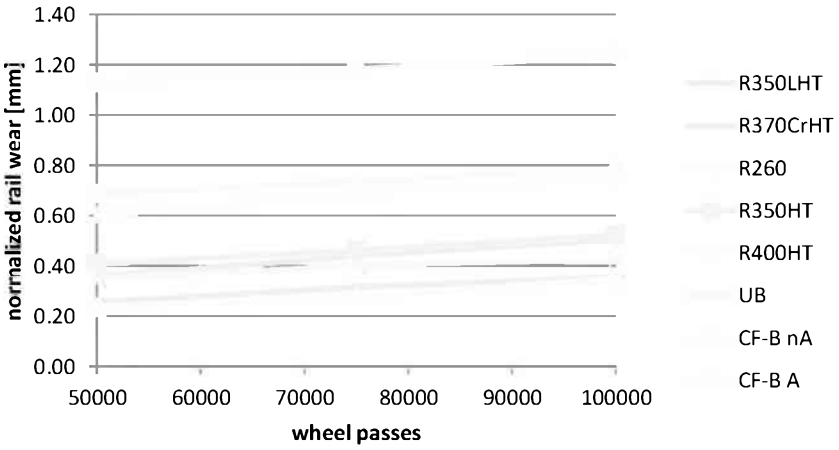

Figure 12.15.: Normalized rail wear for all tested rails, dry contact conditions, R370CrHT and R350LHT show the expected and comparable results in relation to the other rail grades.

R260 FM250 shows some initial wear followed by a very low wear rate.

12.2.2. Long term tests

The results for the LT tests clearly indicate that wear is also reduced for the 4x longer duration of these tests. The fluctuation of wear rate results of R260 FM250 LT is a consequence of the generally very low wear rate which is in the range of the accuracy of the measurement system. As described in subsection 11.2.2 the R350HT test was continued after some test rig problems with the rail of R350HT FM250 #2 accidentally - For that reason the tests was run only until 386,720 wheel passes. Furthermore the final measurement was lost during a hard disk problem. Only an W-wear examination from [71] is available - this result was used to extrapolate the area loss value for R350HT FM250 LT at 386,720. Due to the almost non existent wear this procedure is not believed to influence the results in an unacceptable way.

12.3. Preexisting cracks experiments

In this special FM test series the influence of a dry FM on preexisting cracks was examined. As reported in subsection 11.2.3 the results for the R260 dry-FM tests can not be used due to test rig problems that resulted in unusual high wear rates. For completeness the W-wear rates are shown in figure 12.20. Figure 12.21 presents the results with the R350HT grade. There is a deviation for the first 25,000 cycles between the two tests that can be explained by the fact that the wheel from test *R350HT dry-FM* was used for the *R350HT 25k dry* test. It can also be seen that after turning on the FM device after 25,000 cycles the wear was stopped almost instantly for the *R350HT dry-FM* test.

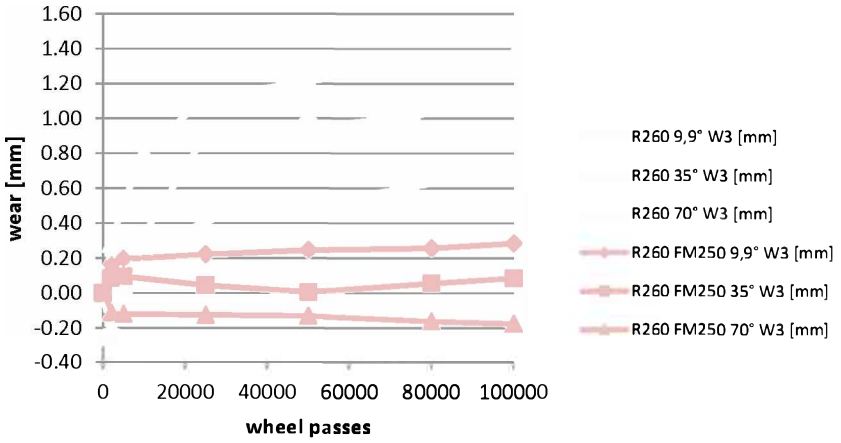

Figure 12.16.: Rail wear results for R260, dry and FM250 (Friction Modifier application every 250 wheel passes) conditions; selected tangent angle w3 calculations. Rail wear reduced due to the FM application. Negative rail wear is cause by plastic flow of the rail material.

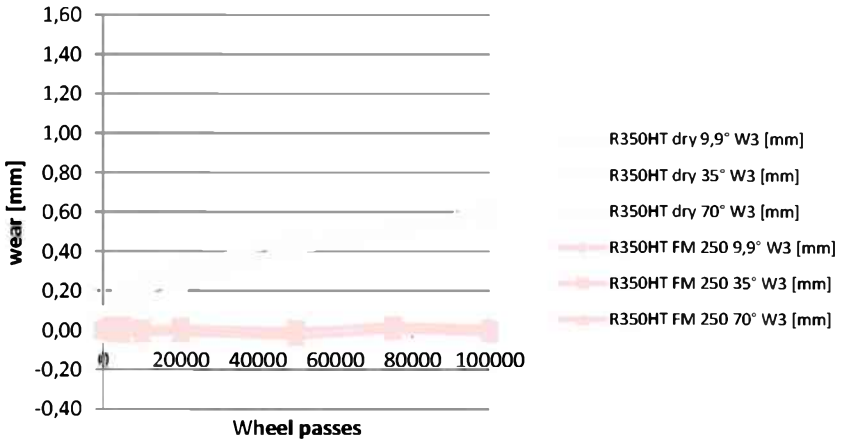

Figure 12.17.: Rail wear results for R350HT, dry and FM250 (Friction Modifier application every 250 wheel passes) conditions, selected tangent angle W3 calculations. Wear reduced beyond measurability due to friction modifier application. No indication of plastic flow for the R350HT material.

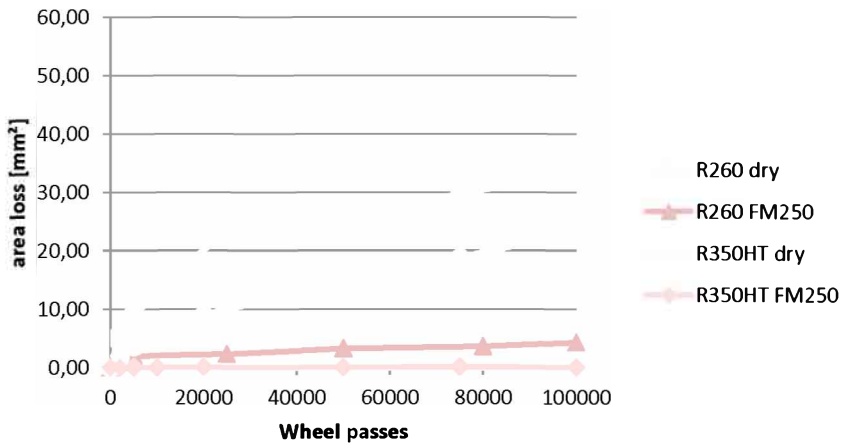

Figure 12.18.: Rail area loss comparison for R260 and R350HT, dry and FM 250 (Friction Modifier application every 250 wheel passes) conditions. Rail wear reduced beyond measurability due to friction modifier application for both grades.

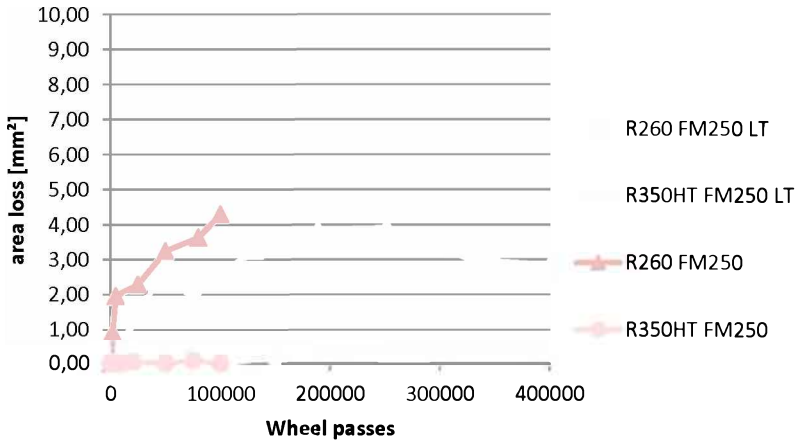

Figure 12.19.: Rail area loss comparison of normal duration (100k cycles) FM tests with long term (400k cycles) tests for grades R260 and R350HT. No increase in rail wear during the long term tests for both rail grades.

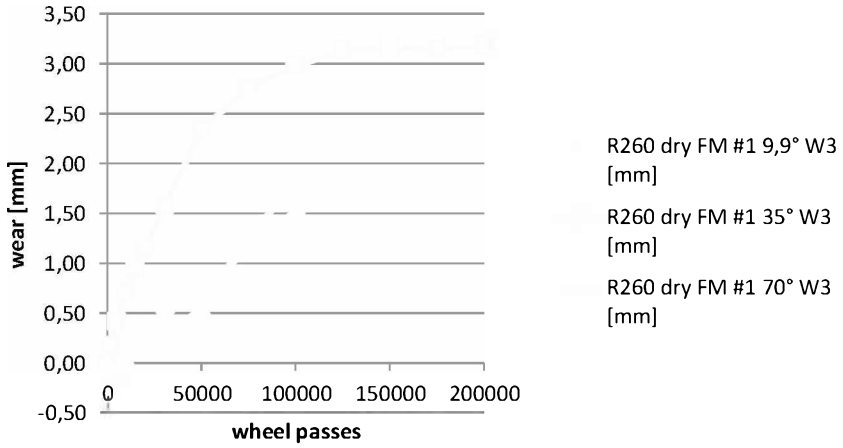

Figure 12.20.: R260 dry-FM test (dry conditions followed by friction modifier conditions); selected rail W-wear calculation. Test rig problems during the first 100k cycles caused high rail wear. Friction Modifier application started at 125k cycles. Beyond 125k cycles wear drastically reduced due to friction modifier application.

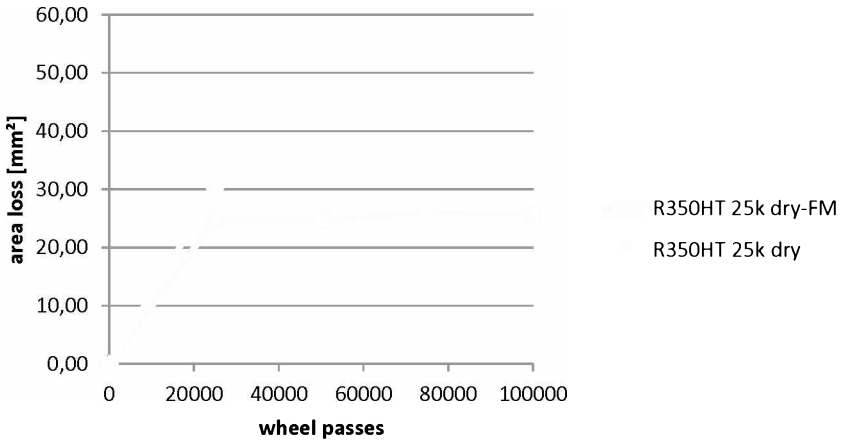

Figure 12.21.: Rail area loss calculation for R350HT 25k dry and R350HT dry-FM (dry conditions followed by friction modifier conditions). Friction modifier application activated at 25k cycles. Wear reduced beyond measurability after 25k cycles due to the friction modifier application (test rig conditions).

13. Plastic Deformation

13.1. Dry Contact Conditions

13.1.1. Normal test conditions

Figure 13.1 shows the plastic deformation data for the dry contact condition tests at position N according to procedure A (see section 8.6.1). The CF-B grade is not listed on this chart as the metallographic structure differs strongly compared to the other rail grades and does not allow for use of this method for determination of plastic deformation. There is a clear difference in plastic deformation between R260, R350HT and R400HT. With increasing rail grade the plastic deformation at the end of the test decreases. The LB grade shows a deformation resistance in the region of R350HT. Plastic deformation (surface and subsurface) is the first step to provoke material damage. Consequently a material (e.g. R350HT) that develops less plastic deformation (with the same loading conditions) compared to another material (e.g. R260) is likely to develop less damage (see figure 13.1).

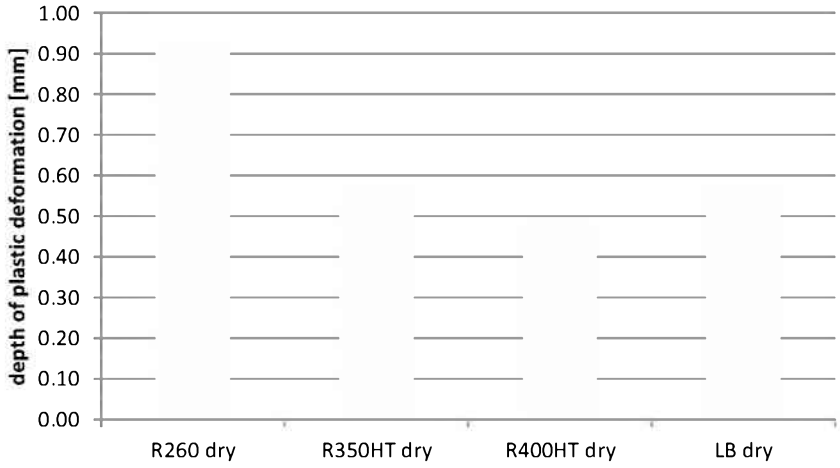

Figure 13.1.: Depth of plastic deformation for dry condition tests, decreasing plastic deformation for increasing pearlitic rail hardness. Examination method (procedure A) for LB grades not applicable due to different material structures.

13.1.2. Test series with deviating contact conditions

The findings for R350LHT and R370CrHT are similar to the previous results. Again with increasing rail grade the plastic surface deformation is reduced (figure 13.2). It can be seen comparing R350LHT (figure 13.2) with the results of R350HT in figure 13.1 that the test

rig conditions were different between these two test series. This results in higher plastic deformation depth for R350LHT and R370LHT compared to R350HT.

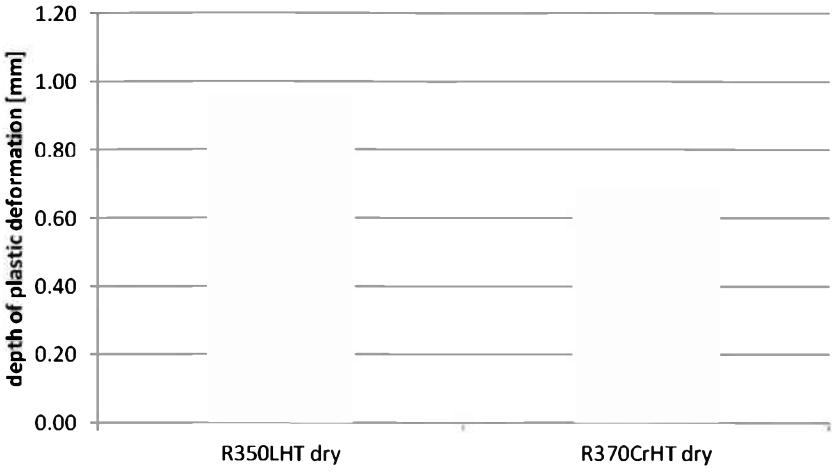

Figure 13.2.: Depth of plastic deformation for R350LHT and R370CrHT according to procedure A.

13.2. Friction Modifier contact conditions

Mainly examination procedure B (see subsection 8.6.2) was used for these tests and the wear measurement point *35° W3* as analyzed. In order to provide comparable results with the previous data method A was applied to position N for the friction modifier tests. Figure 13.3 shows the plastic deformation results of all friction modifier tests (100k and 400k passes) and the corresponding dry tests for both rail grades. The reduction of plastic deformation as a consequence of the friction modifier application for both rail grades after 100k cycles is clearly indicated. Additionally the R350HT grade dry shows even lower plastic deformation values compared to the R260 grade with friction modifier application. The long term tests (400k cycles) for both rail grades show slightly increased deformation depth but more than doubled transverse extension of the deformed structure compared to the equivalent 100k tests. Due to the friction modifier application the traction force is reduced compared to dry conditions. Increasing the test duration increases the accumulation of traction forces acting on the rail surface resulting in the higher transverse deformation extension. Once again the increased material performance of the R350HT rail grade can be seen as this grade shows lower deformation values are observed compared to the R350HT 100k dry conditions even after 400k cycles. Comparing these results now with results obtained through procedure A at position N the findings are slightly different (figure 13.4). Again the reduction of plastic deformation as a consequence of the friction modifier application for both rail grades after 100k cycles is clearly displayed, although the difference between R260 FM250 and R350HT dry is not as distinctive as with procedure B at 35° W3. These results, however, only correspond to the red bars in figure 13.3 as no transverse analysis can be performed with method A and, furthermore, the locations on the transverse rail profile differ. The LT tests show results close to the corresponding 100k tests results concerning deformation depth. Comparing both examination methods it is obvious that the combination of deformation

depth and transverse deformation distance needs to be examined to capture the full material response.

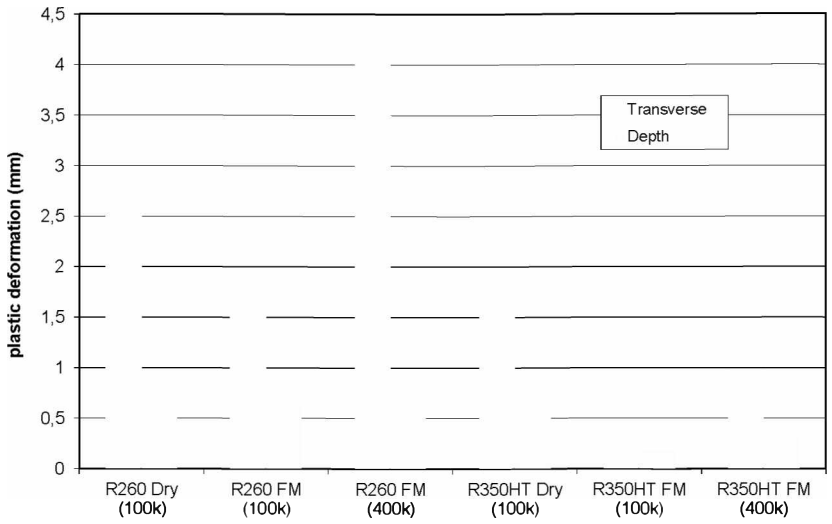

Figure 13.3.: Plastic deformation analysis (depth and transverse extension) according to procedure B at 35° W3 point, depth and transverse extension. Increased resistance against plastic deformation for R350HT under both dry and friction modifier contact conditions clearly visible.

13.3. Pre-existing cracks experiments

Comparing the *100k dry* test with the *25k dry* test (figure 13.5) the values for transverse direction are increased in an amount of approx. 20% whereas the deformation depth is reduced by about the same percentage. The similar dry+FM test results suggest that the main deformation of the material happened during the first 25k dry cycles whereas almost no additional deformation occurred during the subsequent 75k cycles with friction modifier application. Nevertheless it is important to keep in mind that the contact conditions between the original 100k dry tests and the combined tests have significantly changed as mentioned before. This fact might explain the differences observed (*100k dry* test and *25k dry*). Furthermore, also the examination method itself provides the potential for a certain degree of inaccuracy also resulting in the noted differences.

This degree of inaccuracy is significant for both procedures (A and B). However, if only using these methods in a comparative way the conclusions provide sufficient accuracy. For more precise and objective examinations another method like e.g. the EBSD method [72] is suggested.

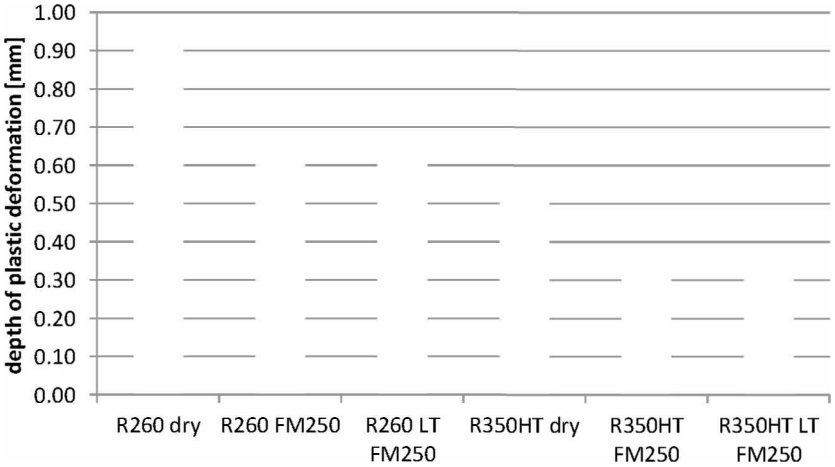

Figure 13.4.: **Depth of plastic deformation analysis according to procedure A at position N for R260 and R350HT, dry and friction modifier conditions. Results are very comparable / almost the same as shown in Figure 13.3 despite different procedure and position on rail (procedure B was done at 35° W3 position).**

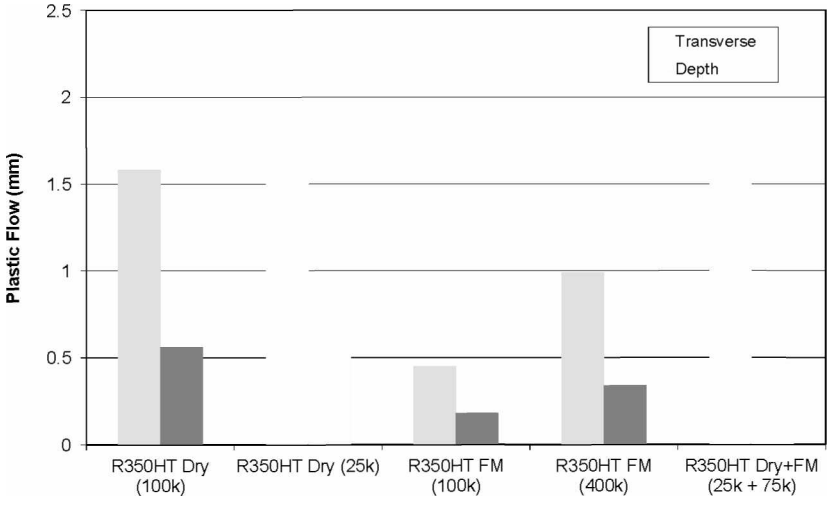

Figure 13.5.: **Plastic deformation comparison of "dry followed by FM" tests with dry and friction modifier tests, grade R350HT, examination procedure B. Plastic deformation for dry+FM and 25k dry on similar level as 100k dry test.**

14. RCF cracks

14.1. Crack depth analysis

The crack depth analysis was done by the metallographic lab of voestalpine Schienen GmbH. Based on the ERRI method [61] this examination was further developed resulting in the fact that for the first tests (R260 dry and R350HT dry) the output data are not available in the same quantity and detail level as for all subsequent tests. As not all of the rail samples were kept over time, some of the examinations can not be. Figure 14.1 shows the crack depth results for all dry tests. In the graph the average crack depth over the analyzed sample length, the standard deviation, maximum and minimum values are displayed. There is a clear decrease in crack depth between R260, R350HT and R400HT in all the listed values. The LB grade shows crack results in the region of the R400HT. The other bainitic grade CF-B in both conditions (A, nA) developed no cracks during the length of the test. The tests done with different contact conditions (R350LHT and R370CrHT) show similar average crack depth results; R350LTH has slightly deeper average crack depth. R370CrHT shows very high scatter in the crack depth distribution and has even deeper maximum crack depths compared to R350LHT.

In track it is quite difficult to get accurate crack depth information. One usually not practiced method would be to remove the rails at the end of a test from track and then to perform metallographic examinations. The other method consists of using eddy current (EC) devices to measure the crack depth. These devices, however, have two disadvantages:

1. The information about crack depth is calculated by the directly measured crack length and an assumed crack growth angle. Due to the fact that this angle is changing with crack length, rail grade and contact conditions, exact depth information can not be extracted out of measured crack length and assumed crack angle.
2. Very tight cracks can not be measured as individual cracks. The crack spacing is influenced again by rail grade and contact conditions.

Eddy current systems are nevertheless used by many infrastructure owners to determine wether there are cracks present on the rail surface. DB (Deutsche Bahn - German Railways) for example also tries to make a rough crack depth categorization with the obtained depth information [73]. Figure 14.2 shows crack results measured by eddy current and subsequent metallographic examination [74]. Generally eddy current is underestimating the crack depth (due to the angle preset). The difference between eddy current and real crack depth is in order of 35%-25%. Nevertheless the trend that with increasing rail strength the crack depth is reduced can be seen with both examination methods. Table 14.1 shows further crack depth results from another track test measured by eddy current only [75]. Again there is a decrease in crack depth between R260 and R350HT. R370CrHT stays on the same level as R350HT, and R400HT shows increased crack depth values compared to R350HT. It is not clear whether these results represent real depth information or inadequate readings. This outlines the complexity of the problem to measure HC depth in track with eddy current.

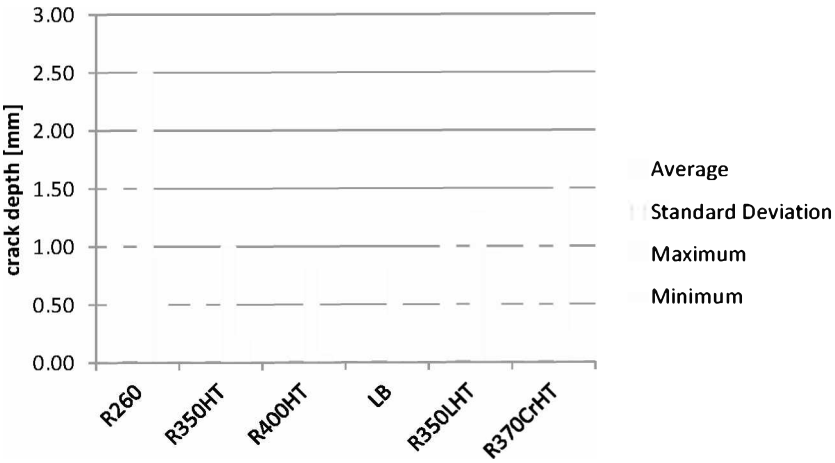

Figure 14.1.: Crack depth of all dry tests according to ERRI method [61]. Decreasing crack depth for increasing pearlitic rail hardness. The LB grade is situated close to the R400HT. The CF-B grades did not develop any cracks. R350LHT and R370CrHT were done with different contact conditions.

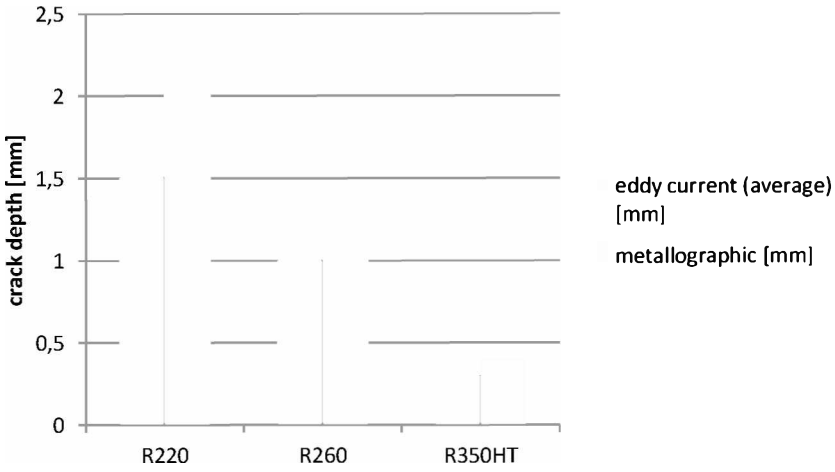

Figure 14.2.: Crack depth, measured by eddy current device and measured by metallographic analysis; track test of voestalpine, R=3300m. Same trends can be seen for both methods [74].

grade	crack depth (eddy current) [mm]
R260	0.8
R350HT	0.35
R370CrHT	0.35
R400HT	0.55

Table 14.1.: Crack depth measured with eddy current after 66 MGT accumulated load (voestalpine track test near Hannover, R=1436m). Uncertainty about the accuracy of the measurement.[75]

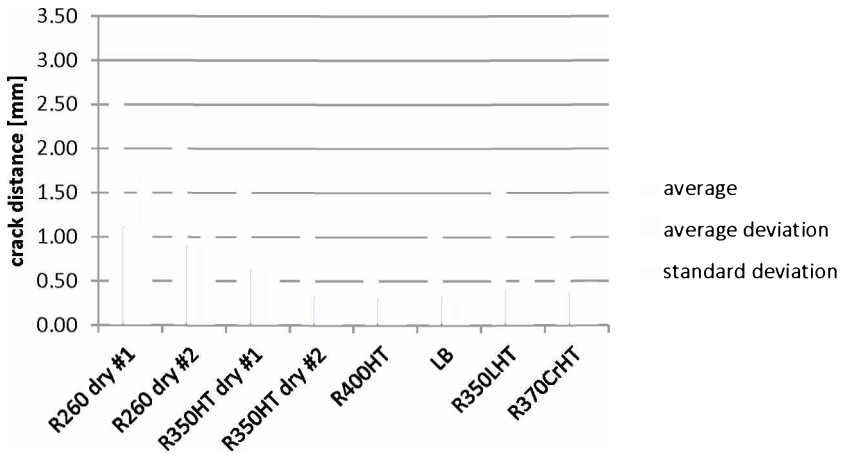

Figure 14.3.: Crack distance examination for all tested grades using an image analysis software; decreasing crack distance with increasing rail hardness of pearlitic steels; R350LHT and R370CrHT performed under different contact conditions.

14.2. Surface analysis

Using the MPI pictures of selected tests a surface crack analysis was performed according to section 8.3. Figure 14.3 shows the results for crack spacing. With increasing rail hardness the crack distance is clearly reduced. Also within the R260 and R350HT tests there is quite a difference between the tests. R260 dry#1 and R350HT dry #2 were done with a pre-worn wheel profile, although the influence of the pre-worn wheel profile on the crack spacing is quite divergent for the the rail grades (R260: increased crack distance, R350HT: decreased crack distance). The R400HT shows the smallest crack spacing and the LB grade is situated between R350HT and R400HT. Also between R350LHT and R370CrHT the trend is as expected: decrease of crack spacing with increasing rail grade. Concerning surface crack length, there is no clear picture available (figure 14.4). Some rail grades seem to be situated around 8mm surface crack length but others differ quite strongly. It is important to keep in mind that the surface crack length is influenced by the position and angle of the camera that was used to take the MPI photo. Both parameters can vary between tests. Consequently these results can only be seen as a rough trend. The crack angles shown in figure 14.5 are not influenced by the camera position. There is no rail grade dependency visible on the crack angle. All crack angles are situated in a band between 28° and 42°. The formation of the crack angles is probably more dependent on the profile development than on the rail grade as the profile development directly influences the creep distribution in the contact patch and the creep distribution again influences the crack formation.

In order to explain the rail grade dependent formation of different crack spacings a more detailed examination was performed using a 20mm rail sample of one test per grade. Figure 14.6 gives an overview about that detailed analysis over the 20mm samples. All the samples were scaled according to the included reference scale. With decreasing crack distance (increasing rail grade, hardness, material strength) the crack length density increases. For the R260 grade a long surface crack is followed by a short one which is again followed by a long crack. For the R350HT grade there are again long cracks (ranging form the lower end to the upper end of the crack band). A series of different cracks with medium or small length is

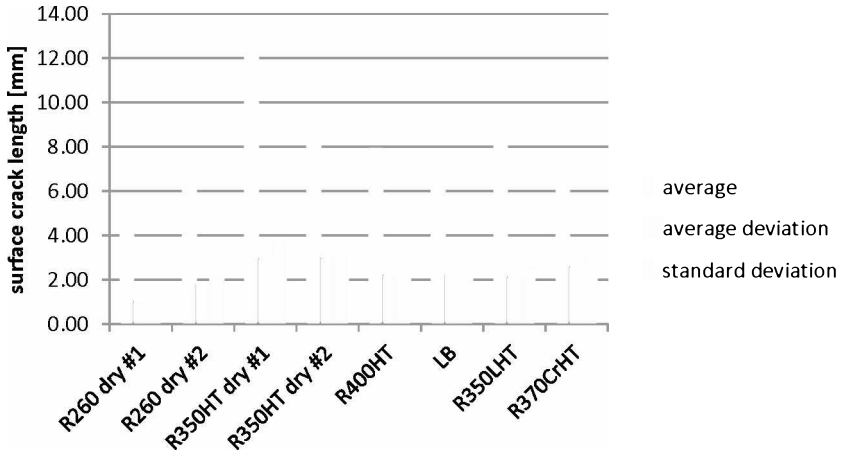

Figure 14.4.: Surface crack length for all tested rail grades. Except R350HT dry#1 and R260 dry #1 all lengths are situated on a similar level.

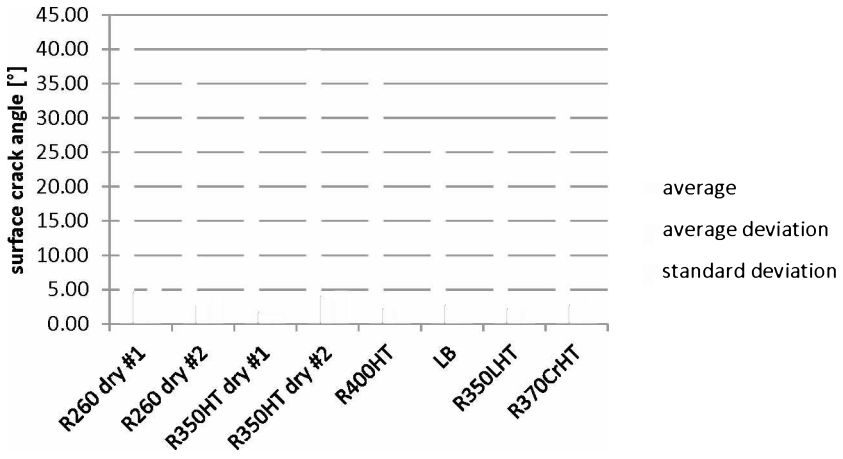

Figure 14.5.: Surface crack angle examination for all tested rail grades. Average angle variation between 28° and 42° independent on rail grade.

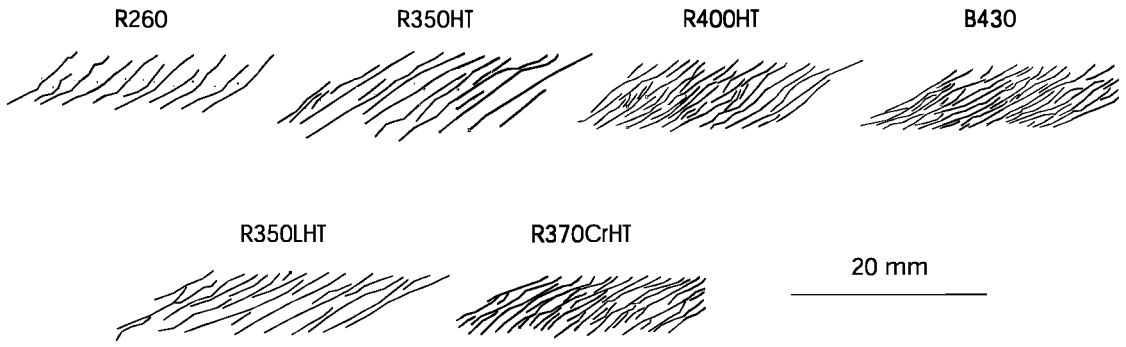

Figure 14.6.: Detailed crack analysis of 20mm MPI samples of selected rail grades. Decreasing crack distance with increasing rail hardness.

situated in the majority of cases between these long cracks. For the R400HT and LB grade this trend intensifies. Again there are a number of long cracks on the surface, but several medium and short cracks are located in-between that show some degree of crack branching on the surface. The same trend can be seen comparing R350LHT and R370CrHT. The results of the detailed three lines analysis is presented in figure 14.7. For all rail grades tested with the standard conditions the crack spacing of the middle line (line 2) is the smallest and this indicates that the distribution of long and short cracks has along line 2 the highest density. This trend can not be seen for the rails tested with alternative contact conditions (R350LHT and R370CrHT). Generally the trend that with increasing rail grade the crack spacing decreases can be seen again. Averaging over all three lines does not change the outcome (figure 14.8). In this figure the R350LHT and R370CrHT seem to fit well to the other test results despite the deviating contact conditions. Average crack spacing (over all three lines) is for R350LHT slightly higher compared to R350HT and the results for R370CrHT are situated between R350HT and R400HT.

Finally a correlation is made dividing the average crack spacing by the measured deformation depth (figure 14.9). The results for the 50x magnification metallographic images show a clear trend: There is a factor of two between crack spacing and deformation depth. The R350HT grade might deviate because the deformation depth was extrapolated using the a 100x magnification picture as no 50x magnification picture was available. The deviation of the R370CrHT could be located well within the accuracy of the method. The 100x magnification pictures may not show that trend due to that fact that a 100x magnification in combination with the focal length of the digital camera in the microscope provides too much magnification to capture the full amount of plastic deformation.

14.3. Pre-existing crack experiments

Only a crack depth distribution was measured for the tests R350HT 25k dry and R350HT dry+FM, as the focus of this test was on the interaction of the dry friction modifier (the water has evaporated) with already existing cracks on the rail surface. In figure 14.10 an increased average and maximum crack depth values for the R350HT dry+FM test can be seen, although it is not clear if this is caused by the longer test duration (more load cycles) compared to R350HT 25k dry or by a misalignment of the vertical cut through the crack band

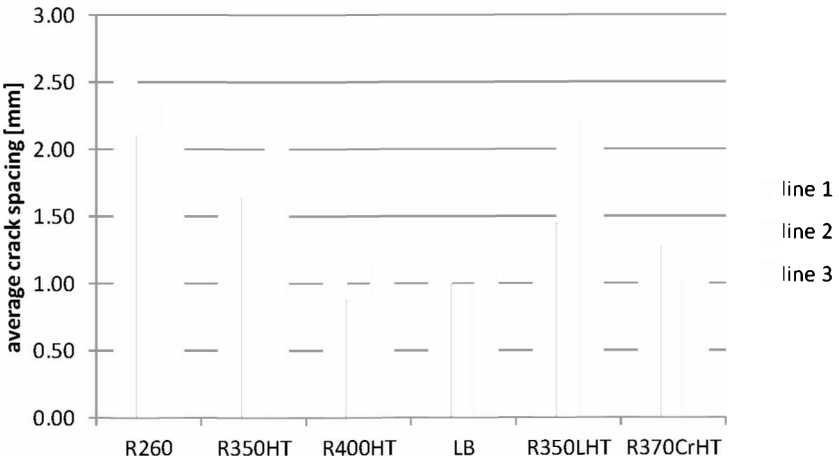

Figure 14.7.: Detailed three lines crack spacing analysis of 20mm MPI samples, line 2: middle line; line 1: center line for upper half; line 3: center line for lower half. Detailed explanation, see figure 8.3 on page 51.

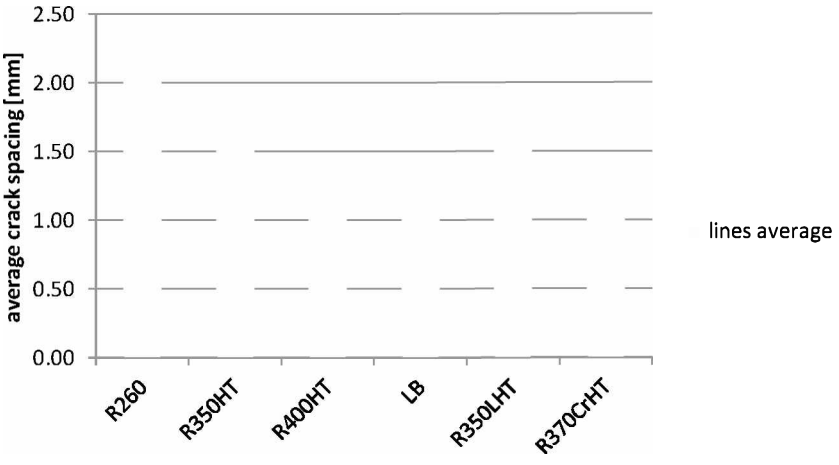

Figure 14.8.: Average crack spacing (averaged over the three lines); detailed analysis of 20mm MPI samples; rail grades distinguish with respect to hardness.

for the Head Check examination. Comparing with results from the literature [76, 67, 66] this can not be interpreted as accelerated crack growth. It is strongly recommended as future work to perform a special test series investigating the effect of different third-body materials on pre-existing cracks on the rail surface.

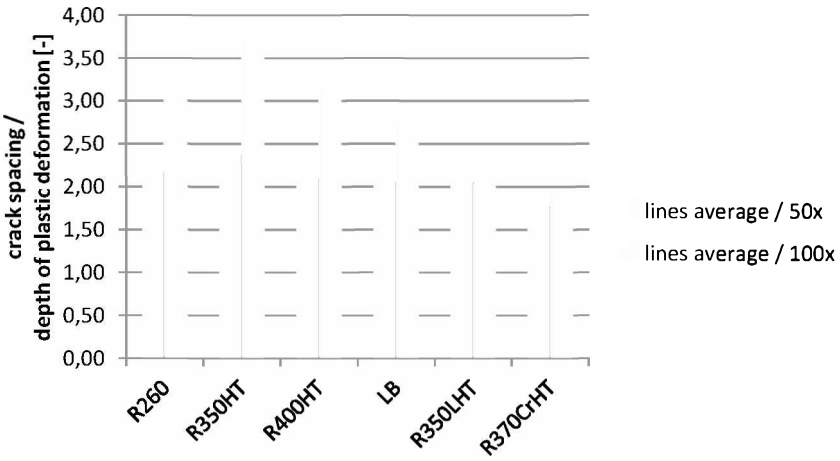

Figure 14.9.: Correlation between crack spacing and deformation depth; 100x magnification does not show the full amount of plastic deformation. A factor of 2 can be observed by comparing with the 50x magnification pictures.

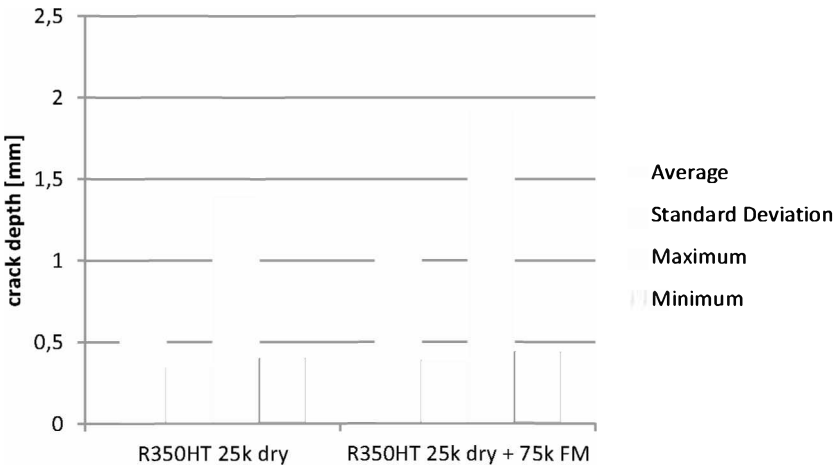

Figure 14.10.: Crack depth distribution of tests with preexisting cracks for grade R350HT; increase in crack depth for R350HT dry+FM (no explanation possible due to lack of data).

15. Creepage

Creepage calculations according to section 8.5 on page 52 were done only for selected tests. A creepage distribution over the whole rail profile of test R260 dry #1 can be seen in figure 15.1. The calculated results concerning certain positions on the profile for selected grades are shown in table 15.1. Especially of interest are the creepage values for the upper and lower head check area (see figure 8.6 on page 53). There is a preferred creepage region where head checks form. It seems that head checks initiate somewhere in between 0.47% and 1.40% creepage but with the availabe data it is not possible to state where exactly they form and how they extend concerning their surface length.

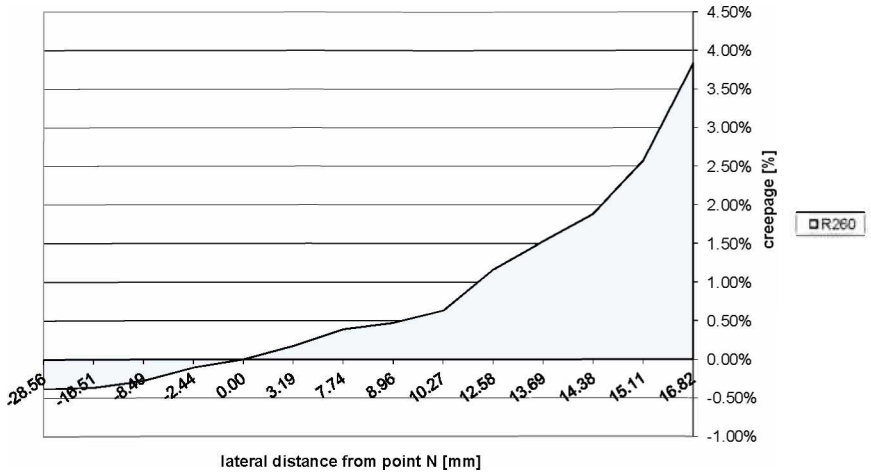

Figure 15.1.: Creepage calculation over the whole contact width of test R260 dry#1 after 100,000 wheel passes.

grade	Lower End	Upper End	HC low	HC High
R260	3.83%	-0.38%	1.53%	0.47%
R350HT	3.09%	-0.95%	1.40%	0.27%
R400HT	2.30%	-0.74%	1.65%	0.27%
LB	3.23%	-0.83%	1.52%	0.35%

Table 15.1.: Creepage calculation for selected tests for specific locations on the transverse profile according to section 8.5 on page 52.

16. Differences vs. real track conditions

Although the results from the test rig show the same trend as observed in track, the absolute values differ because of several differences and limitations that come along with this laboratory experiment:

- Loading: The load (23t wheel load) at the test rig is constant and, at least, two times higher compared to European load conditions (22,5t axle load = 11,25t wheel load). Even when comparing with typical heavy haul conditions of up to 35t axle load (e.g. North America, Australia...) the load at the test-rig is still increased. This will influence the damage and wear behavior of the rail.
- One wheel: There is no second wheel available at the test rig. One of the key characteristics of the railway system is the self steering behavior of a wheelset in a curve [77]. Due to the lack of a wheelset no steering forces will act on the wheel in the rig.
- Lateral contact: In track the lateral wheel-rail contact is controlled by steering capabilities of a vehicle. The lateral contact in the test rig is determined by a given combination of vertical and lateral load.
- Longitudinal forces: In track accelerating and braking forces are applied to the rail-wheel contact region by the traction and braking systems. These activated forces will change the creep conditions in the rail-wheel contact patch and thereby influence the formation of rail damage and wear. The test rig is not capable of applying these external longitudinal forces.
- Identical wheel and rail: In track a certain rail segment is loaded by thousands of different wheel profiles resulting in thousands of different contact locations on that rail segment. So wear and RCF are a result of this contact location distribution. At the test rig always the identical wheel and rail are positioned to each other in the identical way during the whole test. So wheel and rail adapt to each other according to the loads and the material properties of both partners.
- Climate conditions: In track the climate conditions can vary from sunshine to rain resulting in changing friction conditions. The friction conditions will also be influenced by any third body material in the wheel rail contact ([31] and chapter 4 on page 27) like sand, leaves, oxides, etc. At the test rig the climate conditions are kept approximately constant and, therefore, the friction conditions also stay rather constant. Additional third body layer materials aside from wear debris and oxide particles will not be present.

17. Simulation Work

voestalpine Schienen GmbH does not have in house simulation capabilities to simulate rail-wheel contact phenomena. For that reason voestalpine has a number of R&D collaborations with external partners, mainly universities or university competence centers. Some of them are listed in this chapter.

17.1. Material Center Leoben - MCL

voestalpine Schienen GmbH runs an R&D collaboration with the MCL since 1999. Even before this date some specific simulation work was done by the Department of Mechanics at the Montanuniversitaet Leoben. The work before 1999 will not be considered here. Furthermore, the collaboration was orientated to a specific rail part and a specific switch part financed by voestalpine Schienen's sister company VAE. This summary only considers the work done in the rail part.

In the first project phase between 1999 and 2006 the collaboration was organized as a Christian Doppler Lab (CDL) [78] - "Funktionsorientiertes Werkstoffdesign - Modul B: Gefügebeeinflussung und Schädigung durch Beanspruchung" (1999-2004) and then as a direct collaboration with the MCL (2004-2006). First a comprehensive, dynamic 3D model of rail and wheel was developed using the software ABAQUS. The model consisted of a a full wheel and a 3m piece of rail including sleepers with all necessary masses, springs and damping elements to simulate real track behavior (figure 17.1). The rail was inclined and the wheel had a preset angle of attack. The output of this model consisted of contact stresses (vertical, tangential), elastic deformation of wheel and rail, slips between wheel and rail as well as the dynamic vibration behavior of the overall system. As this model is operating in a time domain mode a decrease of wheel-speed from 150km/h (typical simulation speed) to 75km/h (keeping all other parameters constant) directly results in a doubling of the total simulation time from 30h to 60h. Due to the high calculation time and the complexity this model was only used as a reference concerning the output of more simplified models. A 2D analysis of a small part of the rail surface showed that for pure rolling conditions compressive residual stresses develop beneath the surface after a few repeated wheel passes. On the rail surface, however, tensile stresses were found after these few passes. When applying traction the shear stress maximum was found to be at the rail surface. It was recommended to conduct further calculations with realistic surface roughnes as this will have a huge influence on the plastic deformation and residual stresses at and near the rail surface. Consequently also a 2D micro model (0,45mm length and 0,2mm height per contact-partner) with real surface roughness of wheel and rail was developed (figure 17.2). Several simulations with varying parameters were performed. It was found that the surface roughness has a strong influence on the plastification of the material down to 0,2mm distance beneath the rail surface. The amount of surface roughness has only minor influence on the plastic deformation. Increasing the traction coefficient from 0.01 to 0.3 or increasing the creepage by the factor of 5 will result in doubling the plastic

deformation. Increasing the contact pressure by a factor of 2 will result in more than doubled plastic deformation. Even with very low contact pressure of 100MPa a significant plastic deformation was observed (due to the surface roughness influence) [79, 80, 81].

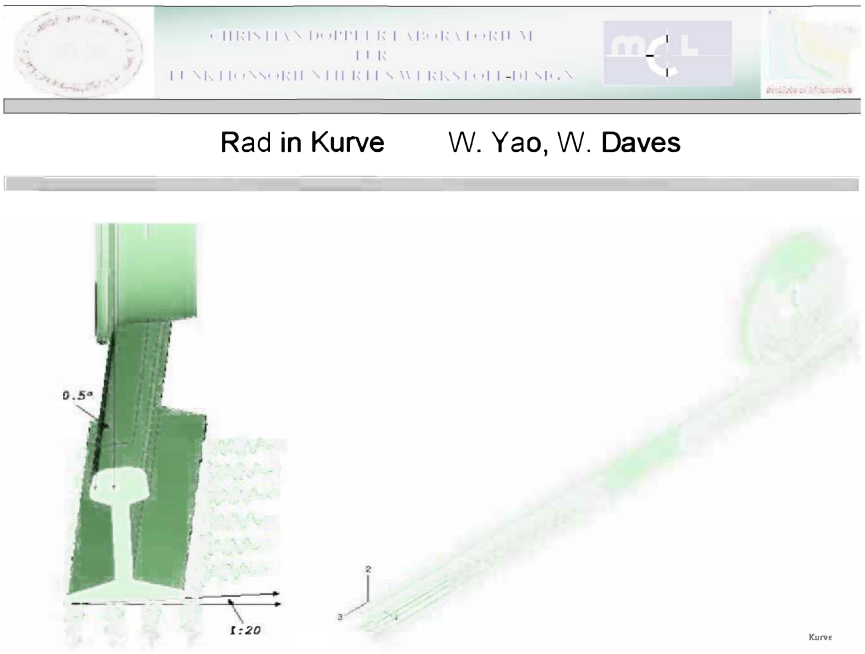

Figure 17.1.: 3D simulation model of a 3m piece of rail including sleepers and a full wheel, developed at the MCL, picture taken from [81].

In the second project phase (2006-now) a hierarchical system approach was developed (using the findings of the first phase). The first step consists of a MBS (multibody system) simulation or a simulation with the comprehensive 3D FEM (finite element method) model. As the calculation times for the 3D FEM model are very high the input of a MBS simulation is preferred. The output of the first step (displacements, velocities and forces) is used as input for the second step. This step consists of a quasi-static FEM model considering only parts of wheel and rail (10cm rolling length). It is possible to simulate elastic (wheel) and elastic-plastic (rail) material behavior. This model provides contact pressures and slips for the third step. The outputs of forces and location/size of contact area can be used for verification and comparison with the first simulation step. Finally a third model - FE micro model - is used to simulate contact pressure distribution within the contact patch, stresses and strains at and near the surface and deformation behavior at and near the surface. This is also a quasi-static model with less then 1mm sliding length and realistic surface roughness. In this model only a small section of the wheel (elastic material behavior) and a small section of the rail (elastic-plastic material behavior) are modeled. A variation of several parameters was done. Comparing smooth surfaces with realistic rough surfaces it was found that for the smooth surface the maximum stresses were found in a certain distance beneath the surface (for pure rolling, see [7] and section 3.1 on page 22). With a surface roughness the maximum stresses are concentrated at the rail surface around the asperities. Replacing in the simulation the the geometrical surface roughness with a varying stress field produced comparable results. Also a vertical singular crack in the rail surface was analyzed using the J-Integral

method. For rough surfaces there was a factor of ten increase of the J-Integral values outlining the importance of surface roughness for crack growth. Recent work is dealing with crack initiation, plasticity and residual stresses at and near the rail surface. SEM (scanning electron microscope) and EBSD (electron backscatter diffraction) examinations are used to characterize the rail material concerning plasticity and crack growth. For the development of residual stresses tests with progressive wheel passes (10, 100, 1,000 and 10,000 wheel passes) were done at the test rig and afterwards analyzed. As this is still ongoing work, no conclusive results are available yet. On the simulation side a 3D explicit model for the test rig was developed. As this model is only capable of doing simulation with quite a coarse mesh (calculation time) a quasi static model (restriction: no dynamic effects) considering only parts of the wheel and rail with a very fine mesh was also developed. First simulations with the quasi-static model examined the influence of different loading conditions, rail inclinations, slips, angle of attacks and elastic layers on the contact pressure and location of the contact patch. This work is also still in progress. For further details see [82, 83, 84, 85, 86].

17.2. Virtual Vehicle Competence Center Graz - VIF

voestalpine Schienen GmbH has had a R&D collaboration with the VIF since 2006. Three projects have been executed since then. A forth project was started in February 2011 and will not be considered here as no results are available yet.

17.2.1. Project A5_S02 Gleiszustandsbewertung

The project A5_S02 "Gleiszustandsbewertung" (*track condition assessment* - 1.1.2006.-.31.12.2008) had the aim of examining the influence of different types of track alignment deviations on the vehicle response and the resulting forces on the track/rail. The tool used for these simulations was the commercially available multibody simulation software SIMPACK [http://www.simpack.com]. According to [87] a schematic summary of such a simulation process is shown in figure 17.3. For the simulations VIF used a nonlinear vehicle model of a passenger car with the SF400 boogie provided by the project partner Siemens TS. 500m length of a standard track with a right hand curve and a left hand curve were simulated. The simulation only considers elastic deformation of wheel and rail. The output of such a simulation consists of global results like the forces (normal, tangential, track forces...), creepages (lateral, longitudinal, spin), contact area, friction power etc... Global means that no distribution of a parameter is calculated within the contact patch. Only one single resulting value per parameter (forces, creepages,...) is calculated for the contact patch. In order to get a distribution within the contact path a second step simulation has to be done using the appropriate algorithm and software code. VIF used the FASTSIM code that uses the CONTACT algorithm developed by Kalker [17]. The FASTSIM code was modified by the VIF (see A5_S01) so that it was possible to calculate all necessary contact parameters with respect to a given distribution over the contact patch. Furthermore it is also possible to include damage indicators like the surface fatigue index FI_{surf} [88] to calculate the likelihood of rail damage within the contact patch. For further details see publications [89, 90, 91, 92] and final project report [93] available at voestalpine Schienen GmbH.

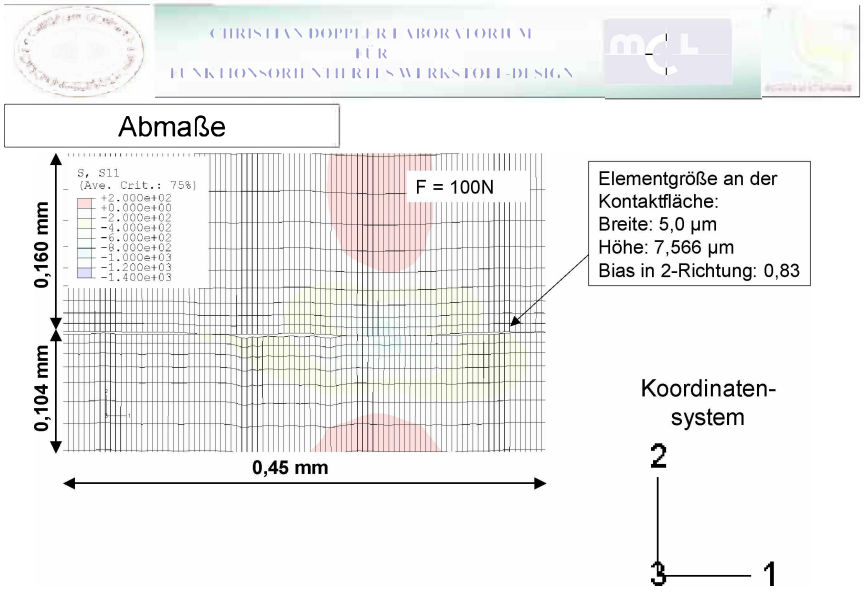

Figure 17.2.: 2D micro model including surface roughness of wheel and rail, developed at MCL, picture taken from [81].

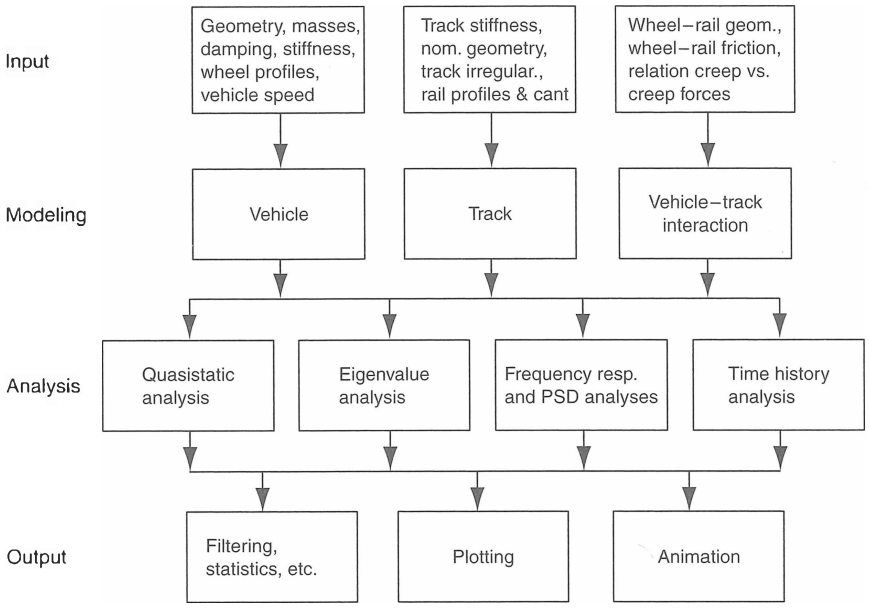

Figure 17.3.: Schematic MBS simulation precess, from [87].

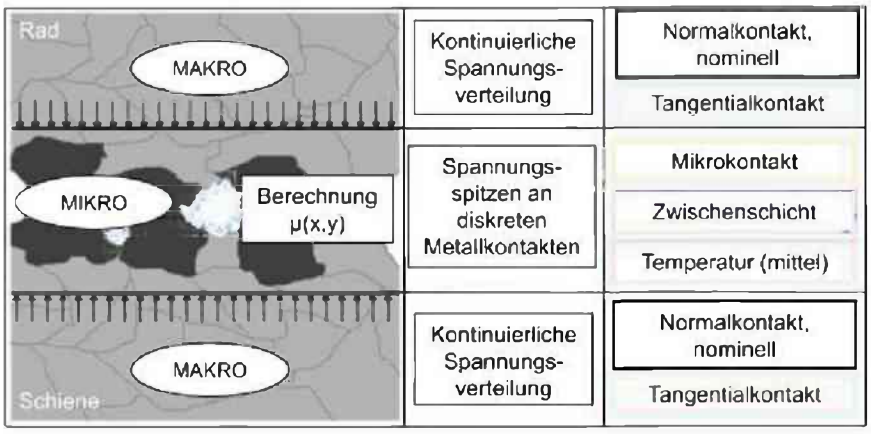

Figure 17.4.: Contact model, coupling between macro and micro scale, provided by VIF.

17.2.2. A5_S01 Rad-Schiene Kontakt Verschleiß

The aim of the project A5_S01 "Rad-Schiene Kontakt Verschleiß" (*rail-wheel contact wear*) was to develop a dynamic contact model with increased predictability of resulting forces in the contact area so that phenomena like wear and RCF could be better evaluated. Again the global output parameters from SIMPACK simulations were used as input parameters for this model. To provide better usability a graphical user interface within MATLAB was developed. Figure 17.4 gives an overview of the coupling between the macroscopic and microscopic parts of the model. A more detailed overview of the parameters that are considered in this model is given in figure 17.5. The interaction between the individual parameters are demonstrated particularly. This model was only validated by using data from the literature concerning the traction creepage relationship and its influencing parameters: surface roughness, contact temperature, normal force, speed and third body represented by a fluid. Due to the lack of material data for the highly deformed surface layer only heuristic assumptions were made for the material behavior. No practical validation of the new contact model (e.g. by using actual vehicle data) was done for time and budget reasons. For further details the see publications [94, 95, 96] and final project report [97] available at voestalpine Schienen GmbH.

17.2.3. D03/T01 Wear and RCF Phenomena in Metro Operation

On 01.10.2008 a project was initiated due to a RCF problem at Wiener Linien subway. On R350HT rails transverse head checks formed on the running surface on the top of rail and some of these head checks resulted in transverse defects of rails. The aim of the project (end: 30.09.2011, final report not yet available) was to find the reasons for the development of transverse head checks by using a combination of MBS and FEM simulation. Track-measurement car data and MBS vehicle models of the subway trains were used to conduct SIMPACK simulations. Additionally wheel profiles of selected trains and rail profiles of three selected track segments were collected and used in the SIMPACK simulations. A new contact model was developed that allows a Hertzian approach for determining and calculating conformal contact conditions. The new model uses a strip approach where the contact patch is divided into several longitudinal strips. For each strip a Hertzian cylindrical contact is assumed. The model is capable of considering normal and tangential contact. Furthermore

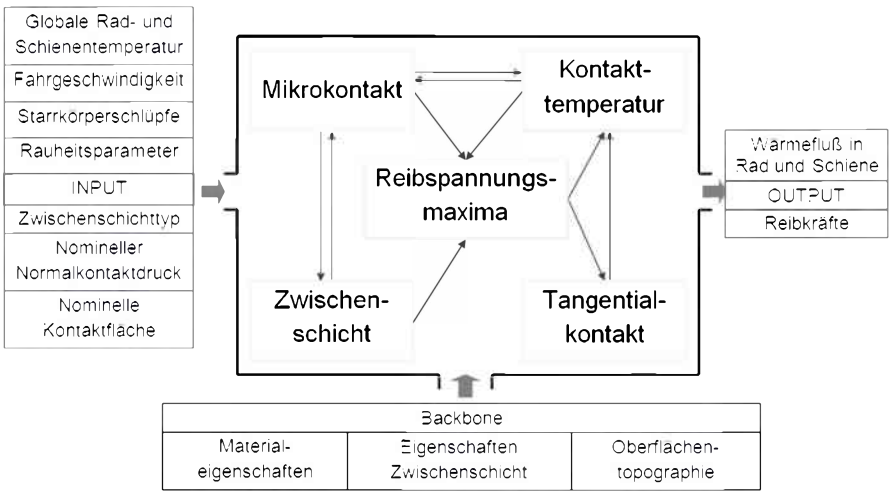

Figure 17.5.: Detailed contact model overview, provided by VIF.

a wear model according to Krause-Poll [98] was also included in the model. The FEM model is still at an early stage - it is a 2D line contact model (part of wheel, part of rail) that can simulate rotation around the wheel axis and translation in longitudinal direction. It can consider stick and slip areas, calculate plastic deformation and determine residual stresses, though it still lacks in adequate material behavior data. Simulations concerning cracks have not been done so far. For further details see the publication [99].

The full scale test rig was used for verification and calibration of the contact model. Therefore profile measurement data of R350HT test were provided to the VIF. First simulation results show qualitatively good agreement with the test rig conditions concerning wear, expected creep distribution and contact stresses. In Summer 2011 a series of special tests was done at the test rig in order to provide calibration data for the model - results will be available by the end of 2011.

17.3. Chalmers Railway Mechanics Competence Center - CHARMEC

voestalpine Schienen GmbH and the sister company VAE have been contributing as industrial partners to the competence center CHARMEC in Gothenburg/Sweden since July 2000. Only rail related projects between 2006 and now (CHARMEC Stage 5 and 6) are considered below. Relevant data for this summary was taken from the triennial reports of stage 4 [100] and stage 5 [101], from the semi annual report [102] as well as from internal voestalpine project meeting presentations. Figure 17.6 shows the interaction of the below described projects.

17.3.1. MU 11 - Early crack growth in rails

The aim of the project MU 11 was to develop a numerical model for simulating and predicting surface cracks (Head Checks) that have already initiated. A parametrized two dimensional model with only one surface crack and a rolling contact load was developed. Any possible wear rate was taken into account by wear induced crack truncation. Short surface cracks

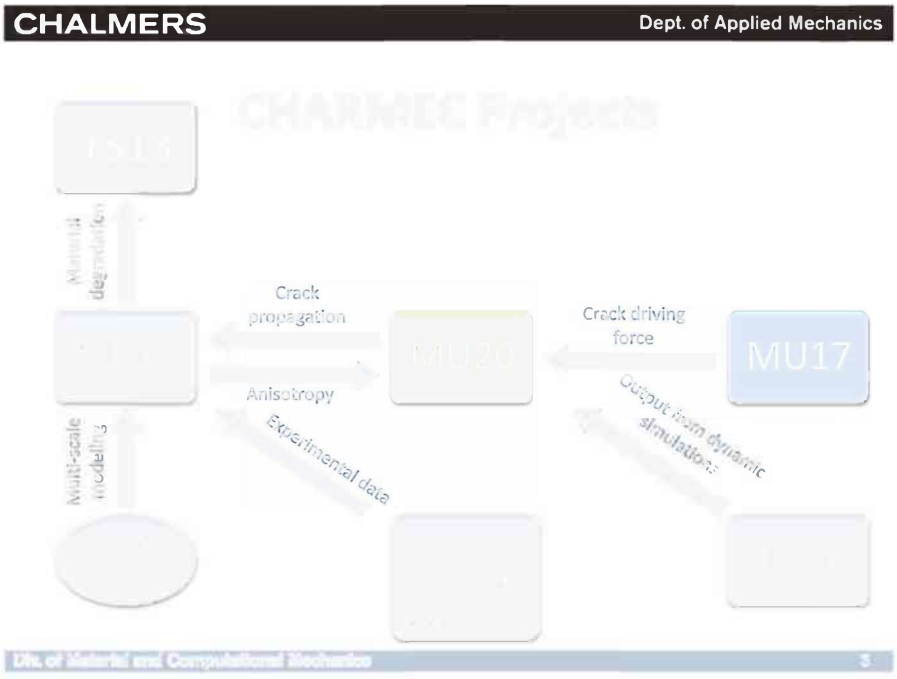

Figure 17.6.: Interaction of relevant projects of the CHARMEC competence center [103].

were found to grow by shear loading. The highest crack growth rate along the rail head surface was found in the direction of the largest reversed shear strain range. The concept of material forces was also part of the detailed study. The project was stopped as the PhD student left Chalmers after his licentiate. This project can be seen as pre-work concerning single crack growth to be included in a larger multi-crack model. The output of this project will be used in the project MU 17 (see below). Results of the project are published in [104].

17.3.2. MU 17 - Elastoplastic crack propagation in rails

MU17 can be seen as continuation of MU 11. This project deals with crack propagation with reference to loading conditions that are associated with RCF development. Models and methods of elasto-plastic fracture mechanics in combination with large plastic deformation were studied. This is of high importance for the complex interaction of multiple short surface cracks due to the changing loading conditions of a passing wheel. The main focus is put to geometrical crack parameters in combination with material properties including wheel rail surface friction coefficients. One major task of this project is the implementation of a crack driving force in the elastoplastic field at the crack tip in the FEM model (including formulation). This crack driving force (generalized J-Integral) is defined as a vectorial measure of the energy release rate due to a variation of the position of a crack tip. It was found that the developed model could simulate the effect of crack shielding (decrease of J-Integral with decreasing crack distances). This project can be seen again as a future part of a comprehensive rail wheel contact model, although the influence of crack shielding in combination with RCF defects is no fully clarified. For more details see publications [105, 106].

17.3.3. MU 19 - Material Anisotropy and RCF of rails and switches

The influence of material anisotropy on the development of RCF will be studied in this project. The anisotropy can be a result of the production process in combination with frictional rolling contact in service and maintenance activities like grinding. Mathematical models for the development of anisotropy will be calibrated against laboratory experiments. This project strongly interacts with the projects MU20 and MU24 as well as with an differently founded project *"Modeling deformation induced anisotropy, on different scales, in pearlitic steel"* that deals with multi-scale modeling of anisotropy development.

So far a hybrid micro-macro model based on wire drawing using the ODF (Orientation Distribution Function) approach was used to model evolving anisotropy in pearlitic steel. Furthermore a hardening relation was included in the model so that it can predict the hardening considering both re-orientation of cementite lamellae and the change in interlamellar spacing (needs modifications). This model was included into a simplified rail wheel contact FEM (ABAQUS) simulation using a Hertzian rail-wheel contact approach.

The next steps of this project will deal with a study on the effect of anisotropy on crack initiation and propagation (in cooperation with MU 20). For more details see publication [107].

17.3.4. MU 20 - Wear impact on RCF of rails

This project will investigate the interaction between wear and RCF. In order to simulate the rail-wheel test rig of voestalpine a 3D GENSYS model was developed. The normal contact problem was approximated by using a multi-Hertzian approach (3 contact ellipses) and the tangential problem was solved by using FASTSIM (Kalker's simplified theory of rolling contact). Plasticity of the rail material was taken into account by using a 2D ABAQUS model. Test rig data were provided to calibrate the model. The results showed good quantitative agreement with the test rig data though the results at the gauge corner differed stronger than on top of rail. This was a consequence of the conformal contact conditions at the test rig which could not be reproduced by the multi-Hertzian approach. Recent work is focusing on crack propagation laws. Three different propagation laws have been analyzed:

- Explicit Proportional Extension (EPE).
- Implicit Proportional Extension (IPE).
- Maximum Parallel Release Rate (MPRR).

The analysis showed that only the MPRR method is applicable in the context of RCF crack propagation. In collaboration with MU17 some crack propagation studies were also done. Parametric studies were conducted with the aim to assess the sensitivity of the final crack path to variations in the input parameters (angle and length of initial crack, friction conditions etc.) using the MPRR method for crack propagation. Initial results show very unstable crack direction behavior. It is assumed that the reason for this is the purely elastic material behavior in the model so far. Future work will include material plasticity and bridging from "time domain" to "cycle domain" simulation. Also the interaction between wear and RCF with reference to the T-γ approach (combined model for wear and RCF developed in the UK) will be analyzed. For more details see publications [108, 109, 110].

17.3.5. MU 24 - High strength steels for railway rails

The aim of this project is to analyze the crack initiation and crack growth in high strength rail steels under fatigue conditions. This includes well defined laboratory LCF tests as well as RCF tests at the full scale test rig of voestalpine. In depth analysis on the LCF behavior of different materials have been done (as part of the Innotrack project also [111]). Also a life predictive tool for LCF tests was developed based on strain energy density (elastic and plastic) that showed good agreement for pearlitic steels. The influence of MnS (Manganese-Sulfide) inclusions in rails was also analyzed but the results were inconclusive. Future work will focus on LCF tests of the R400HT rail and on comparison tests on the voestalpine test rig. For more details see the publications [112, 113].

17.4. Christian Doppler Laboratory "Lokale Analyse von Verformung und Bruch"

The CD lab (see http://www.cdg.ac.at) "Lokale Analyse von Verfromung und Bruch" with its module "Effect of shear deformation in rail steels" dealt between 2003 and 2009 with the problem of highly deformed rail steels. The output of this lab comprises in two doctoral theses.

In the first thesis [114] two examination methods were chosen for the material analysis: ECAP - Equal Channel Angular Pressing and HPT - High Pressure Torsion (figure 17.7). In ECAP a sample with a round or square cross section is pressed through a channel with a bend that has a predefined angle. This method represents a stepwise deformation process. At the HPT process a coin like sample is loaded by two anvils with a hydrostatic pressure. One anvil is rotated with respect to the other anvil. This method can be applied in a continuous or cyclic operation mode allowing very large strains (considerably higher than with ECAP). Comparing pure metals with rail steels it was found that HPT leads for pure metals to grain refinement until a saturation of the refinement process is reached. This also results in a saturation of the mechanical strength. In pearlitic (R260, R350LHT) and bainitic (LB) rail steels the HPT process results in an alignment of the carbides. The carbides are severely deformed, fragmented and even some dissolution of the cementite can take place. Beyond an equivalent shear strain of eight a perfect alignment of the lamella structure was found for all tested rail steels. This refinement also results in an increase of the mechanical strength (especially parallel to the aligned structure). Compared to pure metals no saturation of the mechanical strength was observed. Fracture toughness experiments were conducted using ECAP samples. It was found that crack propagation in samples with orientation perpendicular to the aligned structure was much slower compared to samples with parallel orientation. A crack has either to cross the aligned structure or can grow parallel to the alignment. This results in an increase of fracture toughness with increasing strain for the perpendicular case and a decrease of fracture toughness with increasing strain for the parallel case. For more details see [115, 116, 117]

In the second thesis [118] the work was concentrated on the open questions of the first thesis. The work focused on the effect of severe plastic deformation on the fracture behavior of different materials (pure iron, nickel and pearlitic rail steels - this summary will focus on the rail steels only). For this task the HPT device was upgraded in order to test larger specimen (coin) sizes. A clear influence of the specimen orientation on the fracture toughness was

found. In the pearlitic steel the lowest fracture toughness was found in alignment with the deformed microstructure (brittle fracture along highly deformed and aligned microstructure). On the other hand an increase of fracture toughness was observed in the other testing directions by crack deflection and delamination induced toughening. A factor of 10 was was found for the pearlitic rail steel after the strongest pre-deformation. Cyclic crack growth experiments investigating dependence on sample orientation revealed a micro structure orientation dependent crack growth. If possible the crack will follow the microstructure almost independent of the external loading. For more details see [119, 118, 120, 121].

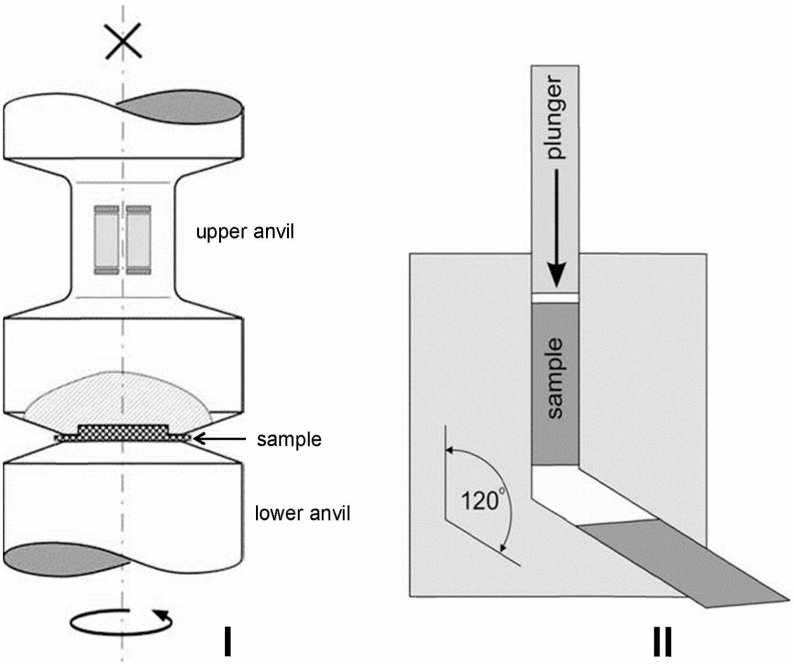

Figure 17.7.: Severe plastic deformation methodology. I: High Pressure Torsion (HPT); II: Equal Channel Angular Pressing (ECAP) [117].

18. Discussion

18.1. Wear

18.1.1. Development of wear

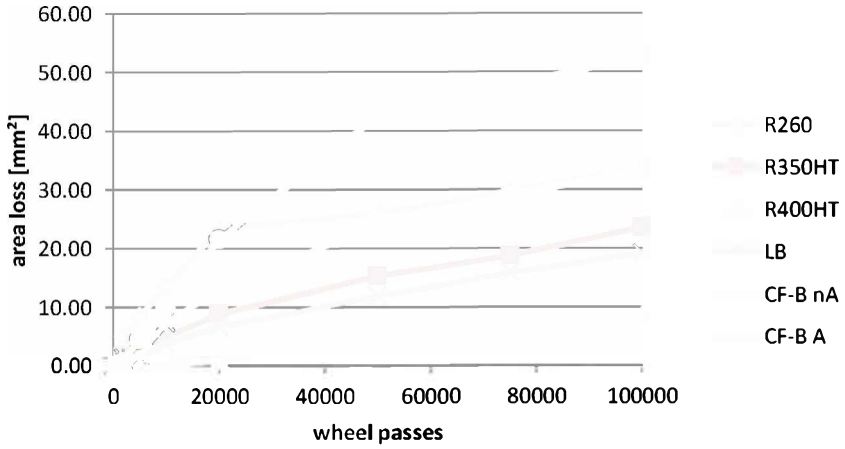

Figure 18.1.: Wear development of all test rail grades; area loss calculation; dry contact conditions; all rail grades show very similar wear rates after initial 25k-50k cycles (dependent on rail grade).

It was observed that after an initial wearing-in process (first 25k-50k cycles, rail grade dependent) all the tested rails showed very similar wear rates (see figure 18.1). This behavior has so far not been observed in track tests. Figure 18.2 is used to explain this behavior. The curves in figure 18.2-a) represent in-situ measurement of High Pressure Torsion (HPT) experiments (see section 17.4) done in [115]. It can be seen that there is a continuous hardening up to shear stress values of 3000 MPa (the test limit of the HPT device). For comparison the curves in 18.2-b) represent the values for tensile testing with micro samples taken from the HPT experiments. It is assumed that the contact forces at the test rig even under these specific high loading conditions will not go beyond 3000 MPa. The load combination at the test rig together with the specific contact characteristics (same wheel on same piece of rail at the same location for every cycle) will cause a saturation condition concerning the work hardening of the tested rail grades. This will result in very similar surface conditions (hardness) for all tested grades after the initial wearing-in process during the first 25k-50k cycles.

According to the Archard wear relation [6] the wear rate is defined by

$$V = c\frac{Nl}{H} \tag{18.1}$$

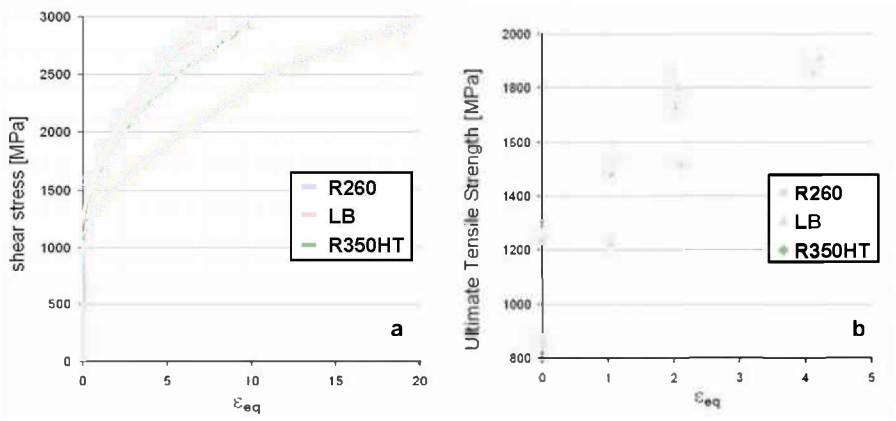

Figure 18.2.: a): shear stress - strain relationship for three rail grades. In-situ measurements of High Pressure Torsion (HPT) tests. b): Tensile test for the same rail grades as in a) for comparison. The figure illustrates that the tested rail grades exhibit a continuous hardening which permits to obtain similar hardness in the vicinity of the rail surface independent of the used rail grade. Pictures taken from [115].

with V = worn volume, c = wear coefficient, N = normal force, l = sliding length and H = material hardness. As the surface hardness of the tested rail materials has reached a similar level after 25k-50k cycles, the wear rates for all the tested rails stay at a comparable level. It is assumed that this is also valid for the CF-B grades (although no HPT curves are available) as they show also the same wear rates at the test rig. In track several factors will prevent the rails from reaching the saturation condition: lower loads, variation of thousands of wheel profiles - variation of thousands of different contact locations, traction, braking, climatic conditions etc... Furthermore the test rig results (figure 13.3 on page 80) also indicate that an R260 grade is much more influenced by the loads compared to R350HT resulting in increased plastic flow. This will also happen in track causing more variation in contact pressures (plastic deformation caused by one wheel might cause for a subsequent wheel contact conditions resulting in high contact stresses) for R260 compared to R350HT resulting in higher wear rates. These two effects will cause rail grade dependent wear behavior in track. Only in Heavy Haul operations might a surface work hardening saturation condition be reached. An indication therefore is given in [122] where a heavy haul line slowly increased vehicle tonnage over time and thereby also increased the work hardening of the rail surface resulting in reported constant and unchanged wear rates.

18.1.2. Normalized wear

The normalized wear calculation method allows the wear comparison of tests done with different initial contact conditions at the test rig. Different initial conditions can be caused by profile deviations of rail and/or wheel or by changes in the general test rig behavior due to repairs or upgrades. In order to apply this method it is necessary that the general test rig set-up (loads, dry vs. wet, inclination, AOA etc.) of the compared tests be the same. During this thesis a series of necessary repairs resulted in a change of the initial rail and wheel contact positions. This very small change in the initial "touch down position" can result in quite different wear rates and resulting contact widths (and will also influence RCF

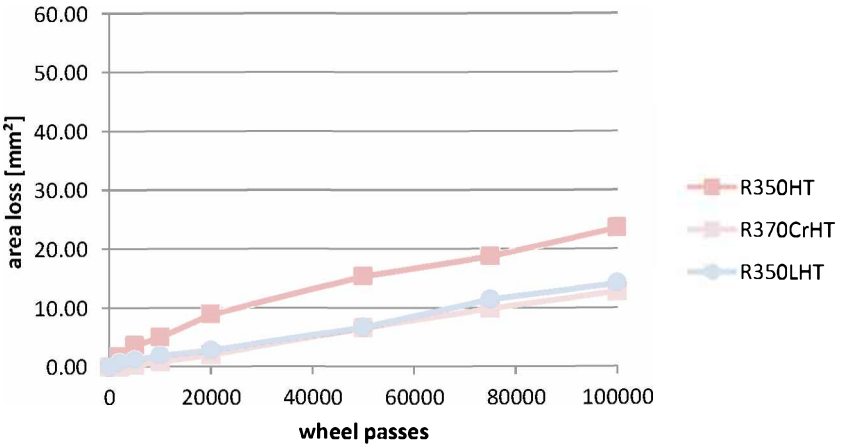

Figure 18.3.: Comparing rail area loss results for R350HT and the tests done after a necessary test rig repair - R350LHT and R370CrHT. The wear results differ due to a change of the initial test rig conditions as a consequence of necessary test rig repairs.

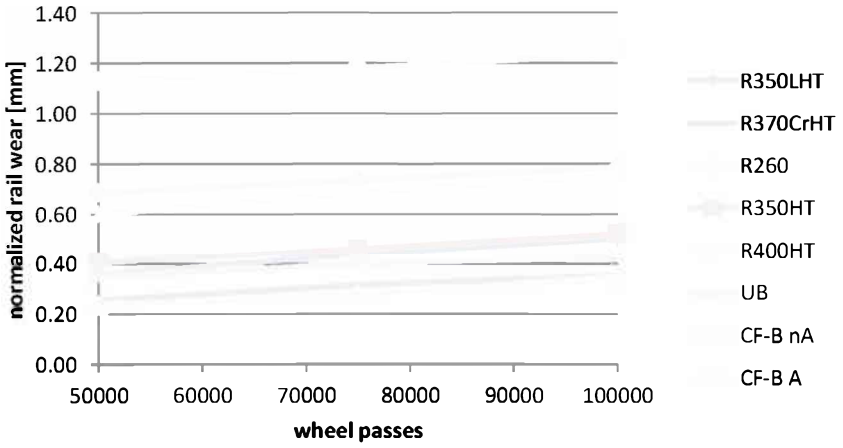

Figure 18.4.: Normalized wear calculation (area loss divided by width of contact band) of all tested rail grades. Method used for compensating small differences in initial contact conditions.

development) - see figure 18.3. The normalized wear is calculated by dividing *area loss* with *width of contact band* on the rail surface - see figure 18.4. Although the tests with R370CrHT and R350LHT were used for verification, it is recommended to use more actual test rig results for further verification.

18.2. Crack distances and plastic deformation

18.2.1. Test Rig conditions

A dimensionless relationship of the factor of 2 was found (see figure 18.5) dividing surface crack spacing (according to chapter 14) by depth of plastic deformation (according to chapter 13). It was also found that with increased rail hardness (for the pearlitic grades) both crack spacing and crack depth at the end of a test were reduced (see figures 14.1 on page 83 and 14.6 on page 86). Before developing a hypothesis that explains the crack spacing in relation to plastic deformation depth, some general statements and observations need to be considered. First any cracks analyzed here have initiated at the rail surface. Due to the loading conditions these cracks will grow driven by the shear stresses from the contact. As published in [119, 123] cracks tend to follow the highly deformed and aligned pearlitic microstructure quite independent of the external loading mode as the aligned pearlitic microstructure provides predefined crack paths. Furthermore, shear stresses will decrease with increasing distance from the surface - this also depends on the dimensions of the contact patch, though only the lateral dimension of the patch can be reconstructed. The longitudinal dimension can only be estimated. Also the degree of material deformation decreases with increasing distance from the rail surface (rail grade dependent). With decreasing material deformation/alignment a microstructural predefined crack growth path is not present any more and further crack growth will become more difficult (an increase of the shear stresses would be necessary to compensate this effect). It seems for the conditions at the test rig, that a crack will stop at a certain depth that is controlled by the degree of deformation and available (shear) stresses. At the test rig only the shear stresses from the contact patch are acting on the crack as no other external factors are present like rail bending, forces caused by acceleration or braking, curving of a wheelset, steering forces, rain, temperature changes, dynamic force changes etc... In addition the wear rate will be another limiting factor at the test rig once the crack propagation rate at a certain distance from the rail surface (dependent on shear stresses and material deformation) is less then the wear rate. There is also an indication in the obtained results that there is a rail grade dependent maximum crack depth. The R350HT 25k dry test resulted in an average crack depth of 0,9mm. The R350HT dry tests resulted in an average crack depth of 0,6mm. Although the contact conditions due to test rig repairs were different between these two tests this can be seen as an indication for a maximum grade dependent crack depth.

Figures 18.6, 18.7 and 18.8 illustrate the development of surface cracks over time (cycles) at the test rig. For most of the tests in this thesis only a written documentation of observations during a test is available. Consequently for R260 (R260 20.2 dry) and R350HT (R350HT 20.4 dry #9) pictures from a test series that is not examined in this thesis are used in order to give a visual indication of what was noted but not photographed during the tests of this thesis. In general it can be seen that the cracks initiate with a larger spacing compared to the crack distance measured at the end of the test. Some pictures give an indication that this minimum possible crack distance is reached before 100.000 cycles. Having a closer look

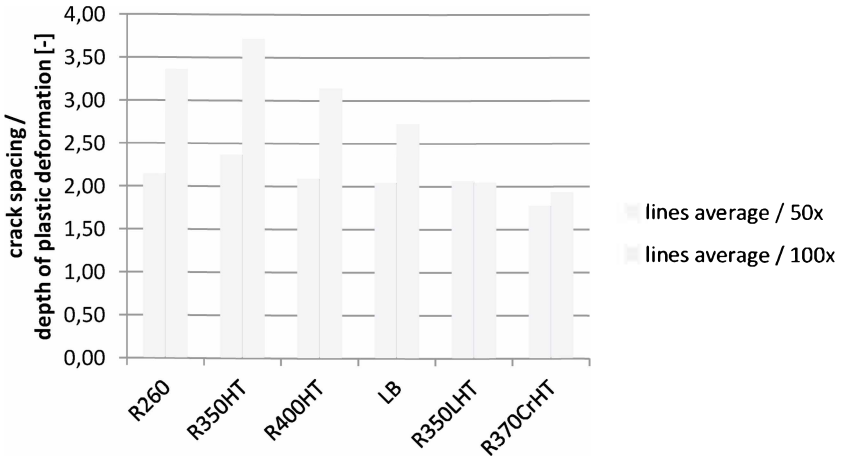

Figure 18.5.: Correlation between crack spacing and deformation depth (dimensionless); 100x magnification does not show the full amount of plastic deformation. A factor of 2 can be observed by analyzing the 50x magnification pictures - see also section 14.2 on page 84.

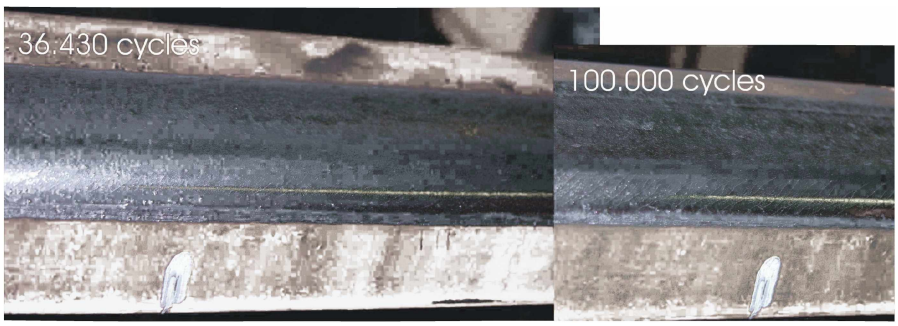

Figure 18.6.: Crack development of R260 grade at stages 36.430 and 100.000 cycles. Initiation at 36.430 with large distances. Final condition with periodic and small distances. Test R260 20.2 dry (not part of the examinations in this thesis - only used for visualization).

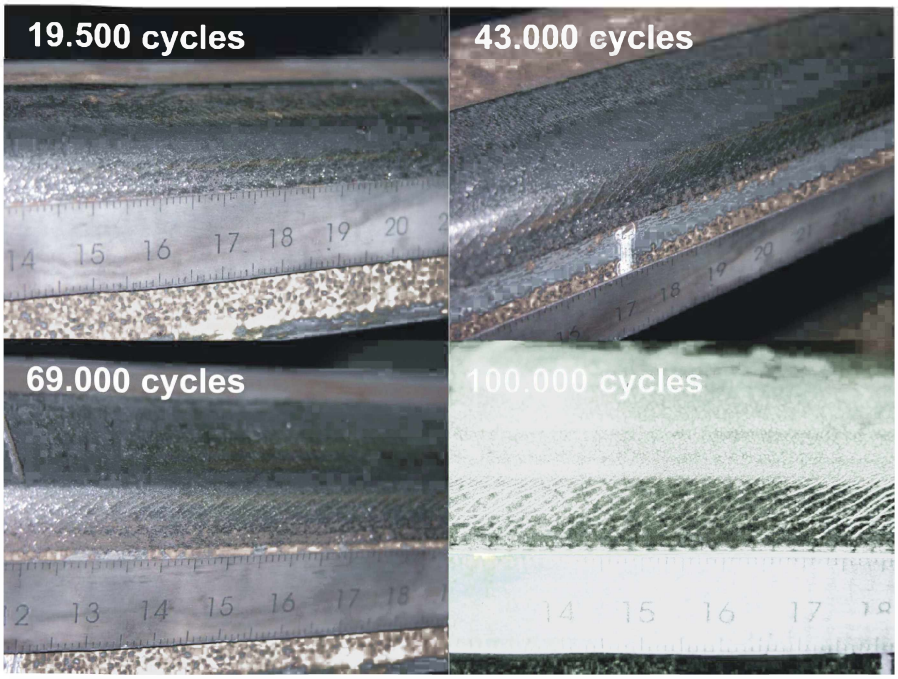

Figure 18.7.: Crack development of R350HT grade at different stages. Initiation with larger crack distances compared to final condition, test R350HT 20.4 dry #9 (not part of the examinations in this thesis - only used for visualization).

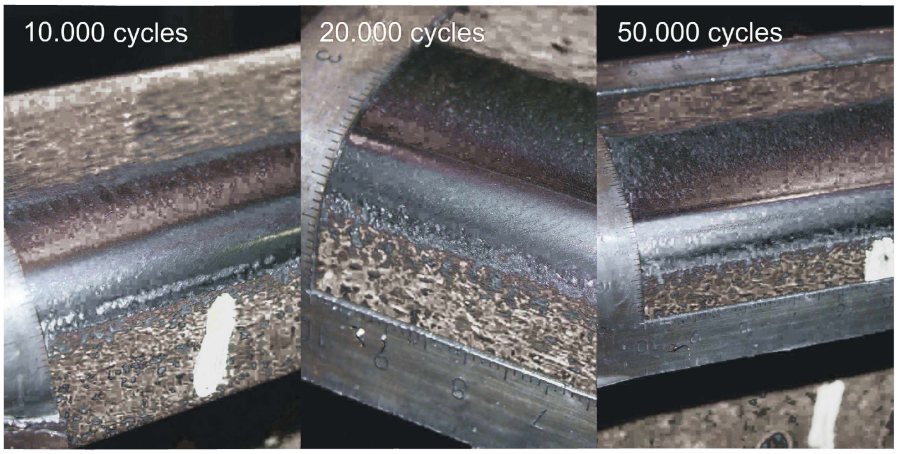

Figure 18.8.: Crack development of R400HT grade at different stages. Initiation with larger crack distances compared to final condition, test R400HT dry.

at R260 there seems to be evidence that there is random crack initiation on the surface. Available data on the R350HT and R400HT could be interpreted in the same way, though there is more periodicity visible at the time the first pictures with cracks were taken. It can also be noted that the time for crack initiation is reduced with increasing rail hardness (R260 around 30k cycles, R350HT around 20k cycles and R400HT around 10k cycles). This can be explained by the initial strength of the rail - with increasing initial strength the time (number of cycles) to reach a saturation condition on the rail surface (steady state wear rate) is reduced and crack initiation can happen earlier during a test.

According to [42] crack initiation on the rail surface will happen in the ratcheting material response condition. In order to initiate cracks on the rail surface under hydrostatic pressure a certain critical shear stress (τ_{crit}) must be reached. Figure 18.9 shows the distribution of the tangential stress along the main axis of the contact patch in longitudinal direction. This tangential stress distribution will result in a shear stress distribution on the rail surface in the contact patch along this longitudinal line. As postulated in [124] not only τ_{crit} must be reached in the contact patch for crack initiation. Additionally a shear stress gradient along a longitudinal line in the contact patch is assumed as another precondition for crack initiation. This can be explained by analyzing two adjacent points, p_1 and p_2, in the contact patch on a longitudinal line. It is assumed that point p_1 experiences the shear stress τ_1 and the neighboring point p_2 experiences τ_2. This results in a $\Delta\ \tau$ with $\tau_2 > \tau_1$. This gradient of shear stresses has maximum values in the stick zone of the contact patch close to the transition from stick to slip (as can be seen in figure 18.9). Of course in the vicinity of the beginning and the end of the contact patch the gradient also has maximum values but there the absolute shear stresses are too low.

Carter [5] based his theory on the idea that the maximum possible traction is limited by the coefficient of friction and that the coefficient of friction is constant over creepage (see figure 18.10). Measurements of traction creepage curves on a 1:5 scaled roller rig (see [125]) revealed that for dry contact conditions the maximum traction is limited by the coefficient of friction as assumed by Carter [5] but as soon as there is full slip between wheel and rail the traction creepage curve decreases again (negative friction characteristics) - see figure 18.11. This indicates that the coefficient of friction decreases with increasing creepage for full slip conditions. This creepage dependent behavior of the coefficient of friction is drafted in figure 18.12. The traction creepage curve of a friction modifier treated rail wheel contact does not show a maximum. With the friction modifier there is a continuous increase of the traction-creepage curve with increasing creepage (positive friction characteristics) - see figure 18.10. Furthermore, as the friction modifier provides a mechanism of shear displacement accommodation between wheel and rail (see chapter 4) the rail-wheel contact is in full-slip condition for all creepage conditions according to Carter [5]. It is assumed that both, the reduced traction coefficient and the positive friction characteristics will change the distribution of the tangential loading (q(x,FM) - tangential loading distribution with friction modifier) as shown in figure 18.13 to a condition with no steep gradient in the q(x,FM) curve resulting in a possible prevention of crack initiation. However, with the given data it is only possible to assume the q(x,FM) curve. Specific simulations (not content of this thesis) would be necessary to verify this idea.

At the beginning of a dry test at the test rig, the contact zone is small in lateral dimension resulting in high contact stresses. Furthermore the material has not yet (fully) work hardened. So the effective shear stress in the contact patch is far beyond the critical contact stress ($\tau_{eff} \gg \tau_{crit}$). Consequently the wear rate is very high. If the material has developed

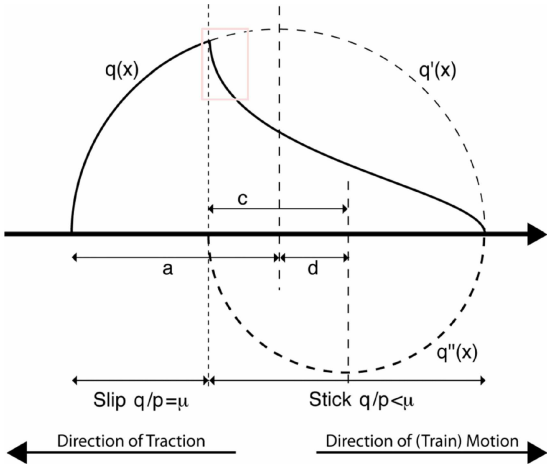

Figure 18.9.: Distribution of stick and slip due to tangential loading of the contact patch. In the vicinity of the transition from stick to slip the gradient of the curve is at its maximum resulting in high $\triangle \tau$ for two neighboring points in the contact zone. Figure edited from [13].

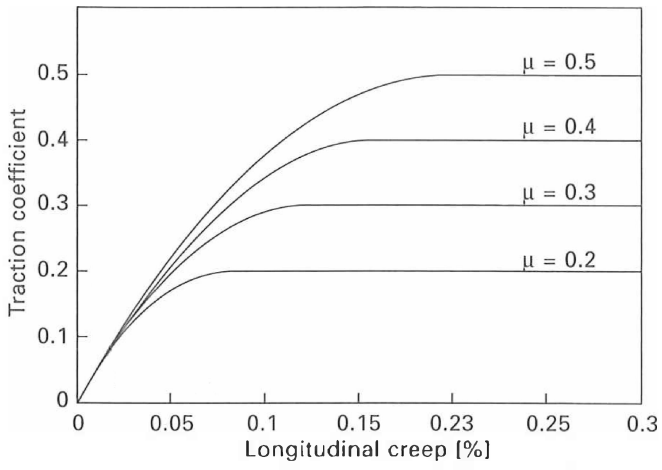

Figure 18.10.: Creep force relationship according to Carter [5] for different coefficients of friction. The maximum possible traction is limited by the coefficient of friction which is assumed to be constant over creepage. Picture taken from [8].

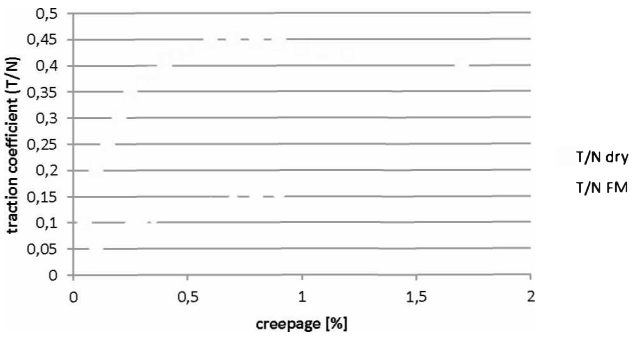

Figure 18.11.: Traction - creepage relationship measured on a 1:5 scaled roller rig for dry (T/N dry) and friction modifier treated (T/N FM) contact conditions (re-plotted from [125]). The relationship for dry contact conditions shows a maximum in the curve whereas the friction modifier treated contact condition shows a continuous increase and lower values.

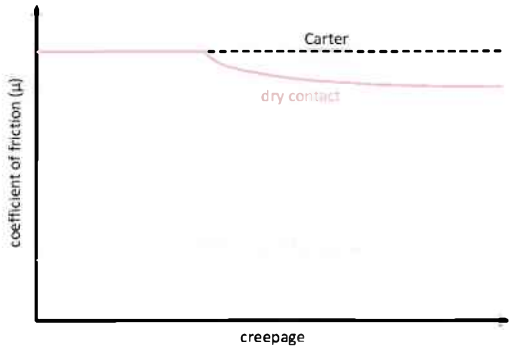

Figure 18.12.: Partly assumed general relationship between the coefficient of friction and creepage according to Carter [5], according to Matsumoto [125] (dry contact - assumed) and and for friction modifier treated contact conditions (assumed).

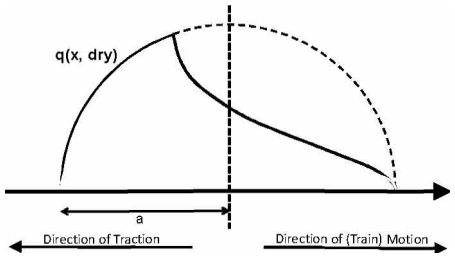

Figure 18.13.: Tangential force distribution in the contact patch for dry (q(x,dry) according to Carter [5]) and friction modifier contact conditions (q(x,FM), assumed curve) - revision of figure 18.9.

a certain degree of work hardening that is already close to the saturation condition the critical shear stress has reached a value close to the effective shear stress ($\tau_{eff} \geq \tau_{crit}$). The wear rate is already low and now first cracks will initiate on the rail surface. Looking again at figure 18.2 on page 103 it can be seen that the curves have rail grade dependent inclinations. Considering now a certain $\Delta\ \tau$ the plastic deformation for the R260 is higher compared to R350HT: If a crack has initiated the next crack will initiate for R260 at a larger distance compared to R350HT. With further increasing wheel passes the surface will continue to work harden until the saturation condition is reached. The crack spacing of newly initiated cracks will be reduced as a consequence of this. As soon as cracks start to grow they will start influencing each other by crack shielding [105]. Also the assumption that there is a rail grade dependent maximum crack depth will have an influence on the possible minimum distance through the crack shielding mechanism. These interacting mechanisms give a possible explanation for the observed reduction on crack spaces over test time and the rail grade dependent periodic average and minimum crack spacing.

In order to verify the postulated mechanism of crack space development more test rig data are necessary. A possible test set-up to provide this data wold consist of:

- Detailed visual examination (photo and MPI) of an R350HT test between 15k and 30k cycles in 1k cycles steps. Afterwards the interval of measurements can be increased to 10k cycles.
- Additional tests to analyze the crack depth at different stages.
  - First cracks visible.
  - Intermediate state.
  - Full periodicity at 30k.
  - Full periodicity at 100k.
- Characterization of the surface condition of the rails (method has to be determined).

18.2.2. Extrapolation to track conditions

Track conditions provide several additional factors and parameters that will influence the damage behavior of rails, and very often these factors or parameters are unknown or very difficult to quantify. These parameters include:

- Operation conditions: traction, braking and train speed will alter the slip conditions in the rail-wheel contact and provide additional forces on the rail surface.
- Load variation: vehicles with different static (and dynamic) loads will influence the damage development of the material.
- Wheel profiles: a specific section of track will always experience a very large number of different profiles resulting in different loading conditions.
- Different vehicles: besides closed systems like metros, there is a very large number of vehicles on the track that have all a specific and characteristic running behavior.
- Track alignment: the track alignment and track quality have a substantial impact on the running behavior of the vehicles.

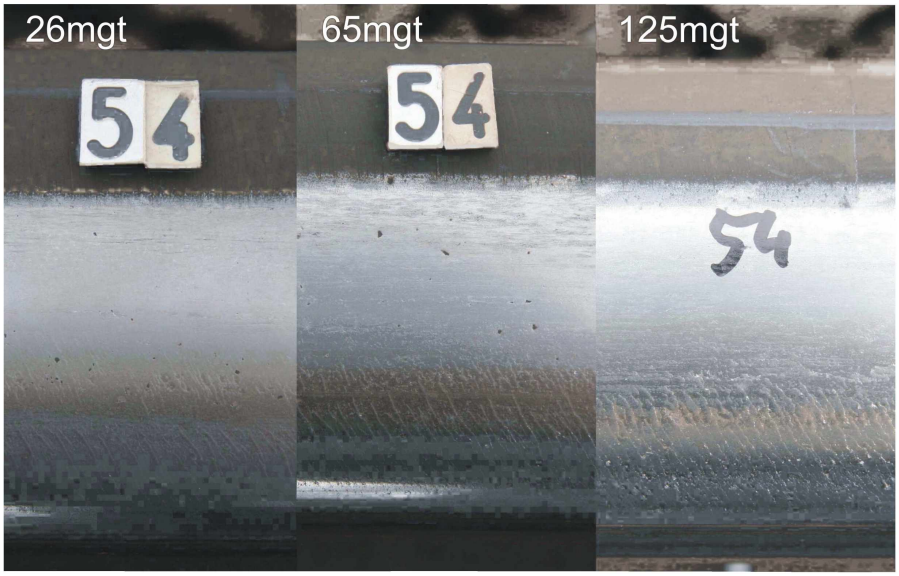

Figure 18.14.: Track tests results for grade R260; German Railways (DB), mixed traffic, curve radius: 1400m, speeds up to 160km/h, approx. 40mgt per year, a decreasing crack distance over time can be seen - pictures not in same scale.

- Environmental influences: Humidity, precipitation, leaves, lubricants, friction modifiers etc. will have a major input on the friction conditions between wheel and rail.

This list is certainly not complete but takes account of the main factors. Despite these additional factors there is evidence that the postulated mechanism is also valid for track conditions as seen in figures 18.14 and 18.15. These pictures were taken from one of voestalpine's track tests at German Railways (DB). The general conditions of this test site were:

- Radius: 1400m.
- Mixed traffic.
- Speed: 160km/h max.
- approx. 40mgt per year.

A decrease in crack spacing can be noticed over test time in figure 18.14. A more detailed analysis is presented in figure 18.15: using MPI pictures of two selected measurement points (provided by DB) a clear trend of decreasing crack spacing for both rail grades can be seen over time (time equal to accumulated load; MGT - million gross tons).

In order to compensate for all these additional (compared to the test rig) influencing factors it is necessary to have a longer examination period while analyzing rail performance in track, resulting in a specific histogram distribution for all these factors that will ideally lead to a "bell curve" and so provide stable conditions. The result of such a track test will be rail grade dependent wear and damage behavior. Though, if there are relevant changes in the distribution of one of the parameters over the examination time, the results of course will also start to change. As long as this change takes place in a slow and uniform way the system will adopt resulting in still usable track test results over time. Even more dangerous are singular events (relative to test duration) that can result in unexpected and drastic changes in the

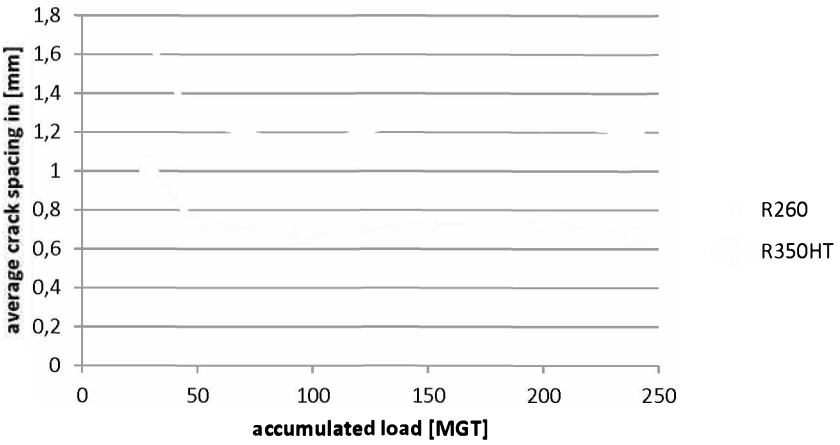

Figure 18.15.: Detailed crack spacing analysis of a voestalpine track test at the network of DB. Clear trend of decreasing average crack distances over test time/MGT (million gross tons) for both rail grades during the first 50 million gross tons. For the rest of the test stable crack spacing.

material behavior (e.g. singular track alignment errors, defective welds, out of the average weather conditions, singular wheel slips etc...). The problem is further aggravated as these singular events often happen undetected as typical examination intervals of a track test are not shorter than 6 months. Such singular events will locally change the stress conditions resulting in locally different damage behavior. Often only the consequence of such a singular event can be examined at the next track visit as the indications of the initial event can disappear very quickly (e.g. by wear).

Results obtained from the extensive track test network of voestalpine and from the EU project Innotrack [45] indicate that the mechanisms postulated in this thesis is also true for the more complex track conditions. Due to the limited amount of information available from these tests, it is proposed to have instrumented track tests (measuring forces, accelerations and distances with sensors on the rails, capturing vehicle IDs) with an visual inspection interval of at least every 4 weeks (or an automated inspection method). With this set-up more data could be generated that would help either to support or to disprove the mechanisms postulated in this thesis.

18.2.3. Additional approaches

Within the research groups dealing with wheel rail problems a number of additional theories concerning plastic flow, crack initiation and crack growth are available.

Jonas Ringsberg from Chalmers University in Sweden [126, 127, 128, 129, 130] postulated a model for life predictions of rolling contact fatigue cracks. Based on twin disk results and rail samples from track he developed a strain-life approach used together with elasto-plastic FEM analysis. This strategy can predict the position for greatest fatigue damage, the orientation of the crack planes and the fatigue life to crack initiation. The author assumed both LCF (plastic shakedown) and ratchetting material response. The author suggests the usage of the multiaxial fatigue model by Jiang and Sehitoglu [131] together with a critical plane approach

for rolling contact fatigue analysis. The author does not state anything on crack spacing in his articles. The author's simulation stops when repeated cyclic material loading has caused first fatigue crack initiation on a certain position on the rail or twin disk test roller specimen (cycles to failure) according to his damage criterion.

A group of researches in the UK has done extensive work on RCF initiation on R220 and R260 rail grades [132, 133]. The group used samples from the British rail network and from twin disk tests done at the SUROS machine in Sheffield/UK. Especially for the low carbon R220 it was found that RCF cracks initiated at the rail surface at the highly shear proeutectoid ferrite (by flaking and micro cracking). The crack will then propagate along the boundary between the proeutectoid ferrite and the pearlite. It was also found that the proeutectoid ferrite suffers from more strain hardening than the pearlite during a load cycle. For rail grades with higher carbon content (and consequently less PE ferrite) the life to crack initiation was found to be longer. The crack initiation for these grades was to some extend also observed at pearlite colony boundaries. The authors assume that plastic deformation and damage (wear and RCF) is caused by ratchetting material response. There is no direct statement on the crack spacing but the group says that the initiation and the early growth of cracks is strongly influenced by the microstructure (for a given contact condition). Further RCF crack growth will be more stress field driven. In recent work [134] 3D simulations were conducted. It is assumed that cracks start at the surface along vertical grain boundaries (prior austenite grain or pearlite nodules boundaries) normal to the direction of strain accumulations. The plastic deformation of the material will then change the orientation of the cracks accordingly.

A slightly different problem in the metro network of Wiener Linien (Vienna) was analyzed in [135]. Transverse cracks on top of rail heads of R350HT rails were the initiation point of some transverse rail breaks. Concerning the formation mechanism of these transverse head checks the authors state that normal or inclined surface flaws form on the rail surface because of the "brittleness" (the author of this thesis does not agree on the term brittleness for rail steels in general) of the head hardened rail material. Crack orientation depends on the orientation of the pearlite or austenite grain. The orientation of the initial flaws is altered by plastic deformation of the rail surface to a wedge-like shape pointing in the direction of the tangential force (acceleration or braking). These (micro-) cracks will grow slowly into the material following the deformed microstructure. The authors further explain the further formation of a specific damage pattern. This will not be considered any further as this differs too much from the effects examined in this work.

A research group in Italy [136] examined R260 rail samples vs. R8T wheel samples on a twin disk machine. They stated that ratchetting is found to be the main damaging mechanism responsible for surface crack formation. Initiated surface flakes will continue to grow along plastic bands following a shear band cracking mechanism. The cracks will stop at a certain depth on the roller specimens as crack growth and wear rate form a steady state competition.

During a discussion on one of the internal R&D coordination meetings with the University partners of voestalpine [137] the crack shielding approach by Johan Tillberg from Chalmers University [105] was discussed as a possible explanation for the periodic crack distances on the rail surfaces. The formation of the cracks is not considered in this approach. The interaction of multiple cracks with specific length and distance was discussed. Depending on crack spacing and length some cracks will continue to grow while others will stop. The discussion outlined two possible scenarios: first this would result in a specific and periodic crack depth distribution or second this would lead to a crack spacing increase with time as wear would remove the cracks that have ceased to grow.

As part of the FFG funded (program KIRAS - http://www.kiras.at) project RSS (Rail System Security) Johannes Stephanides from OBB proposed a mechanism [138] that the crack spacing on the rail surface is a consequence of friction oscillations produced by traction systems and the conditions in the contact patch its self (transition from stick to slip). The frequency of this oscillation will cause some resonance in the rail material that will lead to periodic cracking. Strain gauge measurements done at the rail-wheel test rig and at a test track as part of this project have so far not revealed any supporting indications for this theory. This work is ongoing.

18.2.4. Simulation of the rail-wheel contact

The network of simulation activities of voestalpine was presented in chapter 17. These simulations deal with certain limited aspects of the rail wheel contact as the full scale simulation would on the one hand need multiple, to date partially unknown input data (that even the test rig can not provide) and on the other hand would exceed the typically available computational power for FEM simulations at the universities resulting in calculation times ranging from several hours up to weeks. Some simulations try to overcome the computation time problems by simplifying the problem. However, this simplification holds the danger of oversimplifying the problem and thereby missing important effects. The actual models are very adequate in providing the right geometrical conditions (vehicles, full wheel and rail, parts of wheel and rail etc...). Still the problem of providing reliable and accurate input data (material parameters, contact conditions, contact locations, friction conditions etc...) remains a critical task for the simulation work. As shown above the initial contact condition between wheel and rail (and minor changes of this parameter) can have a significant impact on the results. But even on the test rig the initial contact condition is not known for all three dimensions. Furthermore, including the adequate material parameters in the simulation model is of highest importance when modeling plasticity, crack formation or crack growth. Also here the material data are not available to the necessary extent.

In summary simulations of the rail wheel contact are useful for parameter variation calculations within specific and known conditions. But the obtained results strongly depend on the quality and availability of reliable input data. To understand the important mechanisms and their sensitivity to small changes in the system as well as to provide the right data for simulation will be the challenge of future work in the rail wheel contact.

19. Summary

In this thesis the wear and rolling contact fatigue (RCF) behavior of different pearlitic and bainitic rail steels vs. a pearlitic wheel steel with a hardness of 235BHN is analyzed. All tests were conducted at the full scale rail-wheel test rig of voestalpine Schienen GmbH that is capable of producing realistic rail-wheel contact conditions in a laboratory environment. A test set-up was chosen that provided the formation of both wear and RCF within 100000 wheel cycles. Two different types of contact conditions were selected: dry rail-wheel contact and rail-wheel contact treated with friction modifier (water based suspension of dry solids that optimizes the friction levels between wheel and rail). After each test the rails were examined using non-destructive and destructive techniques. Special focus in the examinations was put on wear, plastic flow and crack development.

It was found that the wear resistance of pearlitic rail grades increases with increasing hardness. Bainitic rails showed lower wear resistance compared to pearlitic grades with the same hardness level. It was also found that after a certain time period of profile adaption between wheel and rail, the wear rate for all tested grades remained on the same level. The difference in the wear was finally affected only by the wear during that adaption phase. The wheel wear (always the softer partner) was not influenced at all by the increase in rail hardness and stayed on the same level for all dry tests. It was found, however, that wear can be drastically reduced by applying a friction modifier.

Plastic deformation results showed a similar trend compared to the wear results. With increasing pearlitic rail hardness the depth of plastic deformation was reduced. The tested bainitic grades showed a deformation resistance equal or better than the tested pearlitic grade with the highest hardness. In the case of friction modifier contact conditions the depth of plastic deformation was reduced compared to dry contact conditions.

For RCF development two trends were found: with increasing material strength of the pearlitic grades both the crack depth and the crack spacing on the surface were reduced. The bainitic grades showed - depending on their microstructure - either very low crack depth or no cracks at all. With the application of the friction modifier the formation of cracks could be prevented at the test rig.

Finally two possible mechanisms that can explain the wear and RCF behavior were revealed. First of all, the similar wear behavior observed for all rail grades after the initial profile adaption phase can be explained by that fact that work hardening (caused by the high loads at the test rig) will result in very similar surface conditions (hardness) for all tested rail grades. This will consequently lead to the similar wear behavior mentioned above. Secondly, concerning RCF a factor of two was found between crack spacing and depth of plastic deformation. It was postulated that the shear stress distribution in the contact patch (dependent on stick and slip zones), the material response to high contact loads (data obtained through HPT experiments from [115]) and the degree of work hardening can result in rail grade dependent crack spacing. Furthermore this idea is also applicable to explain the transition from wear conditions to RCF conditions.

The results and explanations obtained from the test rig experiments are compared with results obtained from track tests of voestalpine concerning wear and RCF behavior of different rail steels. Although the trends between test rig and track test are the same the absolute values of the results can differ quite extensively. A thorough analysis of the differences between track and rig is performed to give an explanation of the parameters that cause these differing results. Finally some indications are highlighted that the proposed interpretation for the rail grade dependent regular formation of head check cracks is also valid for track conditions.

Bibliography

[1] H. Laizner. Österreichs Beitrag zur Entwicklung der Eisenbahnschiene. *Berg- und Hüttenmännische Monatshefte (BHM)*, 121:392–401, 1976.

[2] H. Laizner. Österreichs Beitrag zur Entwicklung der Eisenbahnschiene. Erweiterte Fassung. *Interner Bericht*, page 40, 1976.

[3] H. Hertz. Über die Berührung fester, elastischer Körper. *Journal für die reine und angewandte Mathematik*, 92:156–171, 1882.

[4] J. Klingel. Über den Lauf von Eisenbahnwagen auf gerader Bahn. *Organ für die Fortschritte des Eisenbahnwesens*, 20:113–123, 1883.

[5] F.W. Carter. On the action of a locomotive driving wheel. *Proceedings of the Royal Society London*, A112:151–157, 1926.

[6] J.F. Archard. Contact and rubbing of flat surfaces. *Journal of Applied Physics*, 24:981–989, 1953.

[7] K.L. Johnson. *Contact Mechanics*. Cambridge University Press, 1985.

[8] S. Iwnicki, S. Björklund, and R. Enblom. *Wheel-rail interface handbook*, chapter Wheel-rail contact mechanics., pages 58–92. Woodhead Publishing, 2009.

[9] R. Lewis and U. Olofsson. Mapping rail wear and transitions. In *Proceedings of the 6th International Conference on Contact Mechanics and Wear of Rail/Wheel Systems (CM 2003)*, pages 165–174, Gothenburg, Sweden, 2003.

[10] R.D. Mindlin. Compliance of elastic bodies in contact. *Journal of Applied Mechanics*, 16:259–268, 1949.

[11] J.J. Kalker. Survey of Wheel-Rail Rolling Contact The. *Vehicle System Dynamics*, 5:317–358, 1979.

[12] H. True. *Dynamical Analysis of Vehicle Systems: Theoretical Foundations and Advanced Applications*, chapter Dynamics of Railway Vehicles and Rail/Wheel Contact, page 80. CISM International Centre for Mechanical Sciences, 2008.

[13] G. Vasic, F.J. Franklin, and D.I. Fletcher. Influence of partial slip and direction of traction on wear rate in wheel-rail contact. In *Proceedings of the 8th International Conference on Contact Mechanics and Wear of Rail/Wheel Systems (CM2009)*, pages 139–148, Florence, Italy, 2009.

[14] H. Harrison, T. McCanney, and J. Cotter. Recent developments in coeffcient of friction measurements at the rail/wheel interface. *Wear*, 253:114–123, 2002.

[15] J.J. Kalker. *On the rolling contact od two elastic bodies in the presence of dry friction*. PhD thesis, Delft University of Technology, Delft, The Netherlands, 1967.

[16] J.J. Kalker. *Three-Dimensional Elastic Bodies in Rolling Contact. Solid Mechanics and its Applications*. Kluwer Academic Publishers, 1990.

[17] J.J. Kalker. A fast algorithm for the simplified theory of rolling contact. *Vehicle System Dynamics: International Journal of Vehicle Mechanics and Mobility*, 11:1–13, 1982.

[18] J. Piotrowski. Kalker's algorithm fastsim solves tangential contact problems with slip dependent friction and friction anisotropy. In *Proceedings of Symposium of Advances in Contact Mechanics: a tribute to Prof. J. J. Kalker*, page 2, Delft, The Netherlands, 2008.

[19] K. Six, C. Marte, J. Payer, G. Trummer, P. Dietmaier, and M. Rosenberger. Application of a new contact model to wheelsets - comparison with state of the art models. Accepted as paper/presentation for the IAVSD 2011 Conference, Manchester, 2011.

[20] D.T. Eadie, D. Elvidge, K. Oldknow, R. Stock, P. Pointner, J. Kalousek, and P. Klauser. The effects of top of rail friction modifier on wear and rolling contact fatigue: Full scale rail-wheel test rig evaluation, analysis and modelling. *Wear*, 265:1222–1230, 2008.

[21] W. Daves, W. Yao, and F.D. Fischer. Surface deformation and crack initiation in wheel rail contact. In *Proceedings of the 8th International Conference on Contact Mechanics and Wear of Rail/Wheel Systems (CM2009)*, pages 45–46, Florence, Italy, 2009.

[22] A.F. Bower and K.L. Johnson. Plastic flow and shakedown of the rail surface in repeated wheel-rail contact. *Wear*, 144:1–18, 1991.

[23] R. Heyder. *Untersuchungen zum Schädigungsverhalten von Schienen in engen Gleisbögen*. Technische Universität Berlin: Wissenschaftliche Arbeiten Schienenverkehrsforschung an der Technischen Universität Berlin ; Nr. 1, Technische Universität Berlin, 2007.

[24] A.R.S. Ponter, A.D. Hearle, and K.L. Johnson. Application of the kinematical shakedown theorem to rolling and sliding point contacts. *Wear*, 33:339–362, 1985.

[25] I.M. Hutchings. *Wear: Materials, Mechanisms and Practice*, chapter The challenge of wear, pages 1–7. John, Wiley & Sons, Ltd, 2006.

[26] S.K. Biswas. *Wear: Materials, Mechanisms and Practice*, chapter Wear of metals: a material approach, pages 21–36. John, Wiley & Sons, Ltd, 2006.

[27] S. Andersson. *Wheel-rail interface handbook*, chapter Friction and wear simulation of the wheel-rail interface, pages 93–124. Woodhead Publishing, 2009.

[28] V.L. Popov. *Kontaktmechanik und Reibung*. Springer, 2009.

[29] M. Godet. The third-body approach: A mechanical view of wear. *Wear*, 100:437–452, 1984.

[30] S. Descartes, C. Desrayaud, E. Niccolini, and Y. Berthier. Presence and role of the third body layer in a wheel-rail contact. *Wear*, 258:1081–1090, 2005.

[31] J. Kalousek, K. Hou, E. Magel, and K. Chiddick. The benefits of friction management - a third body approach. In *Proceedings of the World Congress on Railway Research Conference*, pages 461–468, Colorado, USA, 1996.

[32] D.T. Eadie, E. Bovey, and J. Kalousek. The role of friction control in effective management of the wheel / rail interface. In *Proceedings of the Railway Technology Confrence at Railtex*, page 4, Birmingham, UK, 2002.

[33] D.T. Eadie, X. Lu, M. Santoro, and K. Oldknow. Wayside gauge face lubrication: How much do we really understand? In *Proceedings of the 2011 International Heavy Haul Association Conference (IHHA 2011)*, page 8, Calgary, Canada, 2011.

[34] D.T. Eadie, J. Kalousek, and K.C Chiddick. The role of high positive friction (hpf) modifier in the control of short pitch corrugations and related phenomena. *Wear*, 253:185–192, 2002.

[35] M. Roney, D.T. Eadie, K. Oldknow, P. Sroba, R. Caldwell, and M. Santoro. Total friction management on canadian pacific. In *Proceedings of 2009 International Heavy Haul Association Conference (IHHA2009)*, pages 846–854, Shanghai, China, 2009.

[36] M. Roney, S. Bell, S. Paradise, K. Oldknow, and J. Igwemezie. Implementation of distributed power and friction control to minimize the stress state and maximize velocity in canadian pacific's heavy haul/heavy grade operations. In *Proceedings of 2009 International Heavy Haul Association Conference (IHHA2009)*, pages 810–824, Shanghai, China, 2009.

[37] R. Reiff. Top of rail friction control on rail surface performance and grinding. *Technology Digest*, TD-07-039:4, 2007.

[38] D.T. Eadie and M. Santoro. Top-of-rail friction control for curve noise mitigation and corrugation rate reduction. *Journal of Sound and Vibration*, 293:747–757, 2006.

[39] D.T. Eadie, M. Santoro, and J. Kalousek. Railway noise and the effect of top of rail liquid friction modifiers: Changes in sound and vibration spectral distributions in curves. *Wear*, 258:1148–1155, 2005.

[40] D.T. Eadie, M. Santoro, K. Oldknow, and Y. Oka. Field studies of the effect of friction modifiers on short pitch corrugation generation in curves. *Wear*, 265:1212–1221, 2008.

[41] E. Magel, P. Sroba, K. Sawley, and J. Kalousek. Control of rolling contact fatigue of rails. In *Proceedings of AREMA Conference*, page 29, Nashville, USA, 2004.

[42] D.I. Fletscher, F.J. Franklin, and A.J. Kapoor. *Wheel-rail interface handbook*, chapter Rail surface fatigue and wear, pages 280–310. Woodhead Publishing, 2009.

[43] J. Kalousek and E. Magel. The magic wear rate. *Railway Track & Structures*, 3:50–52, 1997.

[44] Code uic 712 R, 4th edition, catalogue of rail defects, 2002.

[45] P. Pointner, A. Jörg, and J. Jaswal. D4.1.5 gl - definitive guidelines on the use of different rail grades. Technical report, EU 6th Framework Integrated Project Innotrack SP4 - Workpackage 4.1, 2010.

[46] S.L. Grassie. *Wheel-rail interface handbook*, chapter Rail corrugation, pages 349–376. Woodhead publishing, 2009.

[47] RAIL-TRACK PLC. Rolling Contact Fatigue in Rails; A Guide to Current Understanding and practice. Heron Press, 2001.

[48] S.L. Grassie, D.I. Fletcher, E.A. Gallardo-Hernandez, and P. Summers. "Squats" and "Studs" in rails: Similarities and differences. In *Proceedings of the 2011 International Heavy Haul Association Conference (IHHA 2011)*, page 8, Calgary, Canada, 2001.

[49] M.J.M.M. Steenbergen, G.W. van Bezooijen, and R.P.B.J. Dollevoet. The mechanisms of squat initiation and growth on train rails. In *Proceedings of the 2011 International Heavy Haul Association Conference (IHHA 2011)*, page 8, Calgary, Canada, 2011.

[50] Z. Li. *Wheel-rail interface handbook*, chapter Squats on railway rails, pages 409–436. Woodhead Publishing, 2009.

[51] H.D. Grohmann, K. Hempelmann, and A. Groß-Thebingb. A new type of rcf, experimental investigations and theoretical modelling. *Wear*, 253:67–74, 2002.

[52] P. Pointner. Materials for wheels and rails - is there a solution for extraordinary requirements? In *Proceedings of the 6th International Conference on Contact Mechanics and Wear of Rail/Wheel Systems (CM 2003)*, pages 79–85, Gothenburg, Sweden, 2003.

[53] A. Moder, P. Pointner, and G. Prskawetz. Herstellung von kopfgehärteten Schienen aus der Walzhitze. *Berg- und Hüttenmännische Monatshefte (BHM)*, 133:321–326, 1998.

[54] EN 13674-1:2011 railway applications - track - rail - part 1: Vignole railway rails 46 kg/m and above (en13674-1:2011), 2011.

[55] H.K.D.H. Bhadeshia and J.W. Christian. Bainite in steels. *Metallurgical Transactions A*, 21A:767–797, 1990.

[56] J.E. Garnham and C.L. Davis. *Wheel-rail interface handbook*, chapter Rail Materials, pages 125–171. Woodhead Publishing, 2009.

[57] P. Pointner. High strength rail steels-the importance of material properties in contact mechanics problems. *Wear*, 265:1373–1379, 2008.

[58] R. Stock. Simulation of Rolling Contact Fatigue (RCF) - an Analysis of Rail Damage on a Testing Machine Developed by VOEST ALPINE SCHIENEN GmbH & CO KG. Master's thesis, Montanuniversität Leoben, 2002.

[59] B. Lichtberger. *Handbuch Gleis*, chapter Der Aufbau des Gleises, page 34. Tetzlaff Verlag, 2nd edition, 2004.

[60] A. Galtier, J.P. Bettembourg, J.L. Perrin, A. Joeller, T. Coppola, S. Notargiacomo, and J. Grijalvo. Contact fatigue of rails under severe conditions. Final Report EUR 21137 EN, European Comission, 2004.

[61] The rolling contact fatigue performance and fatigue strength of naturally hard uic 860 grade 900 a and two head- hardened rails (340 and 370 hb). Technical Report D173/RP5, European Rail Research Institute (ERRI), 1996. German version.

[62] J.J. Kalker. Wheel-rail rolling contact. *Wear*, 144:243–261, 1991.

[63] J.N. Kapur, P.K. Sahoo, and A.C.K. Wong. New method for gray-level picture thresholding using the entropy of the histogram. *Graphical Models and Image Processing*, 23:273–285, 1985.

[64] EN 13262:2004 railway applications - wheelsets and bogies - wheels - product requirements, 2004.

[65] M. Diener and A. Ghidini. *Reliability and Safety in Railwayproducts. Fracture Mechanics on Railway Solid Wheels.* Lucchini RS (self-published), Italy, 2008.

[66] D.T. Eadie, L. Maglalang, B. Vidler, D. Lilley, and R. Reiff. Trackside top of rail friction control at cn. In *Proceedings of the 2005 International Heavy Haul Association Conference (IHHA 2005)*, pages 85–92, Rio de Janeiro, Brasil, 2005.

[67] S.L. Grassie and J. Kalousek. Rolling contact fatigue of rails: characteristics, causes and treatments. In *Proceedings of the 6th International Heavy Haul Conference*, pages 381–404, Capetown, South Africa, 1997.

[68] J. Kalousek, D.M. Fregeredo, and E.E. Laufer. The wear resistance and worn metallography of pearlite, bainite and tempered martensite rail steel microstructures of high hardness. *Wear*, 105:199–222, 1985.

[69] R. Steele and R.P. Reiff. Rail - it's behaviour and relationship to total system wear. In *Proceedings of the 2nd Heavy Haul Conference*, pages 115–164, Colorado, USA, 1982.

[70] G. Girsch and N. Frank. Lcc rail: A software tool for life-cycle-cost calculation for rails. *Rail Engineering International*, 37:8–11, 2008.

[71] R. Stock, D.T. Eadie, D. Elvidge, and K. Oldknow. Influencing rolling contact fatigue through top of rail friction modifier application - a full scale wheel-rail test rig study. In *Proceedings of the 8th International Conference on Contact Mechanics and Wear of Rail/Wheel Systems (CM2009)*, pages 661–670, Florence, Italy, 2009.

[72] D4.3.2 characterisation of microstructural changes in surface & sub-surface layers of rails with traffic. Technical report, EU 6th Framework Integrated Project Innotrack SP4 - Workpackage 4.3, 2007.

[73] H.M. Thomas, A. Dey, R. Heyder, and R. Krull. Prüfverfahren zur Früherkennung von Rollkontaktermüdung in Schienen. *EI - Eisenbahningenieur*, 59:27–33, November 2008.

[74] R. Heyder and G. Girsch. Testing of HSH® rails in high-speed tracks to minimise rail damage. *Wear*, 258:1014–1021, 2005.

[75] R. Heyder. Grinding strategies and material concepts to control rolling contact fatigue. In *Proceedings of Wheel Rail Interaction Seminar*, Chicago, USA, 2009. Presentation.

[76] J. Kalousek. Rolling radius difference - do we appreciate its significance. Technical Report CSTT-VTS-54-AAR, National Research Council Canada, Chicago, USA, 2001. presented at Wheel Rail Interaction Seminar 2001.

[77] S. Iwnicki. Simulation of wheel-rail contact forces. *Fatigue & Fracture of Engineering Materials & Structures*, 26:887–900, 2003.

[78] Christian Doppler Forschungsgesellschaft - http://www.cdg.ac.at.

[79] W. Daves, F.D Fischer, and J. Fischer. Modelling of the wheel-rail contact taking into account the microstructure and material behaviour of the contacting materials. In *Proceedings of the 5th International Conference on Contact Mechanics and Wear of Rail/Wheel Systems (CM 2000)*, pages 136–142, Tokyo, Japan, 2000.

[80] W. Daves, W.P. Yao, W. Razny, F.D. Fischer, P. Pointner, R. Stock, R. Oswald, and H. Blumauer. Dynamical finiteelement analysis - a wheel in a curve and a wheel passing a crossing. In *Proceedings of the 6th International Conference on Contact Mechanics and Wear of Rail/Wheel Systems (CM 2003)*, pages 455–460, Gothenburg, Sweden, 2003.

[81] W. Daves, W. Yao, M. Wiest, W. Ecker, and F.D. Fischer. Abschlussvortrag zum Christian Doppler Laboratorium für funktionsorientiertes Werkstoffdesign (CDL-FMD) Modul B: Gefügebeeinflussung und Schädigung durch Beanspruchung in Eisenbahnschienen. Internal presentation at voestalpine Schienen GmbH, April 2006.

[82] M. Wiest, E. Kassa, W. Daves, J.C.O. Nielsen, and H Ossberger. Assessment of methods for calculating contact pressure in wheel-rail/switch contact. *Wear*, 265:1439–1445, 2008.

[83] W. Daves. The wheel-rail/switch-system: MCL project WPD1. Internal presentation at voestalpine Schienen GmbH, June 2009.

[84] M. Candic. Investigation of plasticity and early stage cracking of rails in wheel-rail contact. Internal presentation at voestalpine, Charmec Meeting in Leoben, available on sumary CD at voestalpine, January 2011.

[85] M. Pletz. Möglichkeiten der Simulation für den Test-Rig. internal project meeeting at voestalpine Schienen GmbH, May 2010.

[86] M. Pletz. Quasistatisches Modell für den Test-Rig: Keil & Zwischenlage. internal project meeting at voestalpine Schienen GmbH, May 2011.

[87] O. Polach, M. Berg, and S. Iwnicki. *Handbook of Railway Vehicle Dynamics*, chapter 12 Simulation, pages 360–417. Taylor & Francis Group, 2006.

[88] A. Eckberg, E. Kabo, and H. Andersson. An engineering model for prediction of rolling contact fatigue of railway wheels. *Fatigue & Fracture of Engineering Materials & Structures*, 25:899–909, 2002.

[89] B. Luber, A. Haigermoser, G. Grabner, G. Schleinzer, and W. Hirschberg. Methods for classification and track geometry evaluation based on vehicle response analysis. In *Proceedings of the 11th MINI Conference on Vehicle System Dynamics, Identification and Anomalies*, pages 147–158, Budapest, Hungary, 2008.

[90] B. Luber, A. Haigermoder, and G. Grabner. Track geometry evaluation method based on vehicle response prediction. *Vehicle System Dynamics*, 1:157–173, November 2010.

[91] I. Nemeth and G. Schleinzer. Assessment of railway track models from dynamical aspects. In *Proceedings of the 7th International Conference on Railway Bogies and Running Gears*, pages 133–142, Budapest, Hungary, 2007.

[92] I. Nemeth and G. Schleinzer. Investigation into the indirect determination of wheel-rail surface roughness. In *Proceedings of the 11th MINI Conference on Vehicle System Dynamics, Identification and Anomalies*, pages 1–12, Budapest, Hungary, 2008.

[93] B. Luber, I. Nemeth, and J. Fuchs. Gleiszustandsbewertung. Kplus - Abschlussbericht vif-AB-2008-033, Kompetenzzentrum Das Virtuelle Fahrzeug, 2009.

[94] C. Tomberger, P. Dietmaier, W. Sextro, and K. Six. Friction in wheel-rail contact: A model comprising interfacial fluids, surface roughness and temperature. In *Proceedings of the 8th International Conference on Contact Mechanics and Wear of Rail/Wheel Systems (CM2009)*, pages 121–132, Florence, Italy, 2009.

[95] C. Tomberger, W. Sextro, M. Rosenberger, and P. Dietmaier. Einfluss von Oberflächenrauheit, fluiden Zwischenschichten und Kontakttemperaturen auf den Kraftschluss zwischen Rad und Schiene. In *Tagungsband 39. Tagung Moderne Schienenfahrzeuge*, volume ZEVrail - Tagungsband, pages 127–135. Georg Siemens Verlag, 2010.

[96] C. Tomberger, M. Rosenberger, K. Six, and P. Dietmaier. Der Rad-Schiene Kontakt: Multi-physikalische Effekte und deren Modellbildung. In *Proceedings of 11. Internationale Schienenfahrzeugtagung*, page 2, Dresden, Deutschland, 2001.

[97] C. Tomberger and G. Müller. Rad/Schiene Kontakt Verschleiß. Kplus - Abschlussbericht VIF-AB-029/2008, Kompetenzzentrum Das Virtuelle Fahrzeug, 2009.

[98] H. Krause and G. Poll. Wear of wheel-rail surfaces. *Wear*, 113:103–122, 1986.

[99] C. Marte, G Trummer, P. Dietmaier, E. Fischmeister, A. Oberhauser, K. Six, and R. Stock. Messung und Simulation von Verschleiß und Rollkontaktermüdung im U-Bahnbetrieb. In *Proceedings 11. Internationale Schienenfahrzeugtagung*, page 2, Dresden, 2011.

[100] R. Lunden. Charmec triennial report 1. july 2003 - 30. june 2006. Technical report, Chalmers Railway Mechanics - a NUTEK/VINNOVA Competence Center, Chalmers University of Technology, Gothenburg, Sweden, 2006.

[101] R. Lunden. Charmec trennial report 1. july 2006 - 30. june 2009. Technical report, Chalmers Railway Mechanics - a NUTEK/VINNOVA Competence Center, Chalmers University of Technology, Gothenburg, Sweden, 2009.

[102] R. Lunden. Semi-annual reports 31 december 2010 of current charmec projects. Technical report, Chalmers University of Technology, Gothenburg, Sweden, January 2011.

[103] J. Brouzoulis, M. Ekh, F. Larsson, A. Ekberg, and K. Runesson. Wear impact on rolling contact fatigue of rails - workshop presentation. Internal presentation at voestalpine, Charmec Meeting in Leoben, available on sumary CD at voestalpine, January 2011.

[104] A. Bergkvist. *On the crack driving force in elastic-plastic fracture mechanics with application to rolling contact fatigue in rails.* Thesis for the degree of licentiate of engineering, Chalmers University of Technology, Gothenburg, Sweden, 2005.

[105] J. Tillberg, F. Larsson, and K. Runesson. A study of multiple crack interaction at rolling contact fatigue loading of rails. *Proceedings of the Institution of Mechanical Engineers, Part F: Journal of Rail and Rapid Transit*, 233:319–330, 2009.

[106] J. Tillberg. *Elastic-Plastic Fracture Mechanics - Application to Rolling Contact Fatigue in Rails.* Thesis for the degree of doctor of philisophy in solid mechanics, Chalmers University of Technology, 2010.

[107] N. Larijani, M. Ekh, G. Johansson, and E. Lindfeldt. On the modeling of deformation induced anisotropy of pearlitic steel. In *Proceedings 23rd Nordic Seminar on Computational Mechanics (NSCM-23)*, pages 153–156, Stockholm, Sweden, 2010.

[108] J. Brouzoulis and J. Tillberg. Propagation of a single head check crack under rcf conditions. In *Proceedings of 16th Nordic Seminar on Railway Technology*, page 17, Nynäshamn, Sweden, 2010.

[109] J. Brouzoulis. On crack propagation in rails under rcf loading conditions. In *Proceedings 23rd Nordic Seminar on Computational Mechanics (NSCM-23)*, pages 42–44, Stockholm, Sweden, 2010.

[110] J. Brouzoulis, P. Torstensson, R. Stock, and M. Eck. Prediction of wear and plastic flow in rails-test rig results, model calibration and numerical prediction. *Wear*, 271(Special Issue):92–99, 2011.

[111] A. Eckberg and B. Paulsson (Editors). *INNOTRACK - Concluding technical report.* International Union of Railways (UIC), 2010.

[112] M. Schlike. Rail materials for switches and crossings. In *Proceedings of 16th Nordic Seminar on Railway Technology*, page 1, Nynäshamn, Sweden, September 2010.

[113] M. Schilke. High strength materials for rails MU24. Project presentation at voestalpine, January 2010.

[114] F. Wetscher. *Effect of Large Shear Deformation on Rail Steels and Pure Metals*. Phd thesis, Montanunversitaet Leoben, March 2006.

[115] F. Wetscher, B. Tian, R. Stock, and R. Pippan. High pressure torsion of rail steels. *Materials Science Forum*, 503-504:455–460, 2006.

[116] F. Wetscher, A. Vorhauer, R. Stock, and R. Pippan. Structural refinement of low alloyed steels during severe plastic deformation. *Materials Science and Engineering A*, 387-389:809–816, 2004.

[117] F. Wetscher. Abschlußpräsentation CD-Labor Lokale Analyse von Verformung und Bruch - Modul 1. Internal presentation at voestalpine, 2007.

[118] A. Hohenwarter. *Fracture of ultrafine-grained metals produced by severe plastic deformation*. Phd thesis, Montanuniversitaet Leoben, 2010.

[119] A. Hohenwarter, R. Stock, and R. Pippan. Changes in the fracture toughness of a rail steel subjected to high pressure torsion. In *Proceedings of the 12th International Conference on Fracture*, page n/a., Ottawa, Canada, 2009.

[120] A. Hohenwarter, R. Stock, and R. Pippan. Severe plastic deformation of a bainitic rail steel. *Materials Science Forum*, 584-86:655–660, 2008.

[121] A. Hohenwarter and R. Pippan. Abschlusspräsentation - Modul 1: "Effect of shear deformations in rail steels". Internal presentation at voestalpine, 2010.

[122] T.J. Ludlow. The journey to 40 tal - the fmg experience. In *Proceedings of the 2011 International Heavy Haul Association Conference (IHHA 2011)*, page 8, Calgary, Canada, 2011.

[123] A. Hohenwarter, A. Taylor, R. Stock, and R. Pippan. Effect of large shear deformations on the fracture behavior of a fully pearlitic steel. *Metallurgical and Materials Transactions A*, 42:1609–1618, 2001.

[124] P. Pointner. Ein Modell für die Head Check Musterbildung. Internes voestalpine Dokument - Version 07, August 2010.

[125] A. Matsumoto, Y. Sato, H. Ono, Y. Wang, Y. Yamamoto, M. Tanimoto, and Y. Oka. Creep force characteristics between rail and wheel on scaled model. *Wear*, 253:199–203, 2002.

[126] J.W. Ringsberg, M. Loo-Morrey, B.L. Josefson, A. Kapoor, and J.H. Beynon. Prediction of fatigue crack initiation for rolling contact fatigue. *International Journal of Fatigue*, 22:205–215, 2000.

[127] J.W. Ringsberg, H. Bjarnehed, A. Johansson, and B.L. Josefson. Rolling contact fatigue of rails - finite element modelling of residual stresses, strains and crack initiation. *Proceedings of the Institution of Mechanical Engineers, Part F: Journal of Rail and Rapid Transit*, 214:7–19, 2000.

[128] J.W. Ringsberg. Cyclic ratchetting and failure of a pearlitic rail steel. *Fatigue & Fracture of Engineering Materials & Structures*, 23:747–758, 2000.

[129] J.W. Ringsberg and B.L. Josefson. Finite element analyses of rolling contact fatigue crack initiation in railheads. *Proceedings of the Institution of Mechanical Engineers, Part F: Journal of Rail and Rapid Transit*, 215:243–259, 2001.

[130] J.W. Ringsberg. Life prediction of rolling contact fatigue crack initiation. *International Journal of Fatigue*, 23:575–586, 2001.

[131] Y. Jiang and H.A. Sehitoglu. A model for rolling contact fatigue. *Wear*, 224:38–49, 1999.

[132] F.J. Franklin, J.E. Garnham, C.L. Davis, D.I. Fletscher, and A. Kapoor. *Wheel-rail interface handbook*, chapter The evolution and failure of pearlitic microstructure in rail steel - observations and modelling, pages 311–348. Woodhead Publishing, 2009.

[133] J.E. Garnham and C.L. Davis. Very early stage rolling contact fatigue crack growth in pearlitic rail steels. In *Proceedings of the 8th International Conference on Contact Mechanics and Wear of Rail/Wheel Systems (CM2009)*, pages 61–71, Florence, Italy, 2009.

[134] F.J. Franklin, A. Gahlot an D.I. Fletscher, J.E. Garnham, and C. Davis. Three-dimensional modelling of rail steel microstructure and crack growth. In *Proceedings of the 8th International Conference on Contact Mechanics and Wear of Rail/Wheel Systems (CM2009)*, pages 53–59, Florence, Itlay, 2009.

[135] E. Fischmeister, H.P. Rossmanith, F. Loibnegger, H.N. Linsbauer, P. Mittermayr, and A. Oberhauser. From surface cracks to rail breaks - recent investigations and results of research at the Wiener Linien metro system. In *Proceedings of the 8th International Conference on Contact Mechanics and Wear of Rail/Wheel Systems (CM2009)*, pages 333–339, Florence, Italy, 2009.

[136] A. Mazzu, G. Donzella, M. Faccoli, C. Petrogalli, and R. Roberti. Progressive damage assesment in the near-surface layer of railway wheel-rail couple under cyclic contact. In *Proceedings of the 8th International Conference on Contact Mechanics and Wear of Rail/Wheel Systems (CM2009)*, pages 99–204, Florence, Italy, 2009.

[137] R. Stock. Summary CD of Charmec Meeting in June 2008 in Leoben. Internal summary CD of all presentations during that meeting. Available at voestalpine Schienen GmbH, June 2008.

[138] R. Stock, S. Scheriau, and J. Stephanides. Internal voestalpine meeting reports of several RSS project meetings. 2010/2011.